GLOBAL HEAT BALANCE WITHOUT AND WITH SOLAR RADIATION MANAGEMENT

BY

CHENGHAO DING

THESIS

Submitted in partial fulfillment of the requirements
for the degree of Master of Science in Nuclear, Plasma, and Radiological Engineering
in the Graduate College of the
University of Illinois at Urbana-Champaign, 2018

Urbana, Illinois

Master's Committee:

Professor Emeritus Clifford Singer, Advisor
Associate Professor Yang Zhang

ABSTRACT

A linearized global heat balance model which is driven by five classes of influence on long wavelength radiation and four classes of influence on short wavelength radiation is calibrated against historical estimates of global average temperature. Additional influences are variability of solar irradiance and the initial global average temperature at the end of pre-industrial period. Industrial activities perturbs the concentration of CO_2, CH_4, N_2O, tropospheric ozone, other greenhouse gases, and contrails in the atmosphere. Also, anthropogenic influences on short wavelength radiation including effects of land use changes on albedo, anthropogenic tropospheric aerosols and stratospheric ozone and black carbon on snow, effects of volcanoes, and variable solar irradiance are considered. The "climate sensitivity" of global average temperature response to these influences accounts for the "ice albedo" effect of global average temperature changes on absorption of short wavelength radiation and the influence of temperature changes on atmospheric water. Using the data-calibrated model, global average temperature is extrapolated to the year 2220.

To my parents, for their love and support.

ACKNOWLEDGMENTS

I would like to express my special thanks to my advisor Professor Clifford Singer. He greatly motivated my interests in climate change research, and I appreciate him sharing his ideas and advice, particularly Chapter 9 of this thesis.

I would like to thank the NPRE department head, Professor Rizwan Uddin. With his caring and help, I quickly enjoyed my life at the University of Illinois at Urbana-Champaign.

I would like to thank Professor Yang Zhang for reading the thesis and giving valuable advice on the work.

I would like to thank Illinois International Programs (IIP) to provide funding for my research.

I would like to thank Program in Arms Control & Domestic and International Security (ACDIS) for providing me a very comfortable study room and study resources for my research.

I would like to thank the NPRE department office, including Becky Meline, Margaret Krause, and Barbara Russell. Special thanks are due to Becky Meline for encouraging me to enjoy both my research and life in the United States. Special thanks are due to Margaret Krause for making appointments for Oral English Assessment (EPI) and my qualifying exam. I wish her a wonderful life after her retirement. Special thanks are due to Barbara Russell for helping me open the door of the computer room in Talbot when I was locked out on weekends.

I would like to thank all my colleagues Susan Forsyth, Bei Yang, Nuole Chen and Christopher Szul. Special thanks are due to Susan Forsyth for helping me print materials and make appointments. Special thanks are due to Yang Bei for discussing this project and providing me with insights into the economic impact of climate change, and Nuole Chen also discussing this project with me. Special thanks are due to Christopher Szul for helping me fix infor-

mation technology problems and setting up a github account for posting the codes and for advice on coding style.

Most importantly, I am deeply grateful to my family, especially my beloved parents. They are being so supporting to my career dream. Their support and love are the source of my passion of daily life and my dream. I cannot overstate my appreciation for their caring and love.

TABLE OF CONTENTS

LIST OF TABLES

LIST OF FIGURES

CHAPTER 1

INTRODUCTION

For research and educational purposes, it is sometimes convenient to have a computationally efficient model of the evolution of global average temperature. The present work describes a global heat balance model with parameters calibrated against historical time series data on global average temperature based on thermometer measurements. Included are models of ten contributions to radiative forcing that are calibrated against historical time series estimates and formulated to make conceptually consistent extrapolations beyond the historical data base. Where direct historical information is insufficient to calibrate models of radiative forcing suitable for long term extrapolation, data and extrapolations of global population and deforestation are used as proxies to estimate some of the parameters in the radiative forcing models. A particular motivation for this work is to support an interactive simulation of international negotiations on human effects on climate change, including the possibility of deliberate creation of a stratospheric haze to reduce radiative forcing [1].

The latest report from the Intergovernmental Panel on Climate Change (IPCC) states that warming of the climate is unequivocal and that many changes observed since the 1950s are unprecedented in recent times, some even over millennia. That report adds that emissions have been accelerating and that we will pass through a global CO_2 safety limit by 2030 [2]. Studies have shown that: (1) Humanity's influence on a warming climate is obvious. (2) Greenhouse gas emissions rates have accelerated since 1970, with the steepest increase coming in the past decade. (3) Global warming is already harming agriculture, the environment, and human health.

Therefore, globally, economic and population growth continue to be the most important drivers of increases in carbon dioxide emissions from fossil fuel combustion. The IPCC defines climate forcing as "An externally imposed perturbation in the radiative energy budget of

the Earth climate system, e.g. through changes in solar radiation, changes in the Earth albedo, or changes in atmospheric gases and aerosol particles." Thus, climate forcing is a "change" in the status quo, a direct measure of the amount that the Earth's energy budget is out of balance. Most researchers choose a "baseline" year before the beginning of world industrialization—usually either 1750 or 1850—as the zero point, and compute radiative forcing in relation to that base. The IPCC uses 1750 as its base year and it is the changes in the various radiative forcing agents since then that are counted. The perturbation to direct climate forcing (also termed "radiative forcing") that has the largest magnitude and the least scientific uncertainty is the forcing related to changes in long-lived, well mixed greenhouse gases, in particular carbon dioxide (CO_2), methane (CH_4), nitrous oxide (N_2O), and halogenated compounds such as chlorofluorocarbons(CFCs).

The present report uses more complete time-series calibrated models of contributions to radiative forcing than previously used for the Climate Action Gaming Experiment (CAGE) [1]. It also systematically uses time series estimates of global average temperature to estimate adjustable parameters. One of these three parameters adjusts shielding from tropospheric aerosols for use in a global heat balance rather than in more complete global circulation models (GCMs). Another of the calibrated parameters affects how the climate sensitivity ($^\circ$K of global warming per W/m^2 of radiative forcing) in a long-term equilibrium limit. The third parameter is proportional to the thermal inertia of a surface ocean mixed layer.

The discussion here starts in chapter 2 with comments on relationships between demographics, deforestation, and climate change. Moving on to long wavelength radiative forcing, chapter 3 describes emissions of CO_2, CH_4, and N_2O. Chapter 4 goes on to provide analytically extrapolatable formulas for the radiative forcing from these and other greenhouse gases, and from contrails. Chapter 5 summarizes and discusses the results of long wavelength radiative forcing. Chapter 6 describes similarly integrable fits primarily for short wavelength effects. Chapter 7 gives formulas for impacts on the evolution of global average temperature and compares results from variation of adjustable parameters to global average temperature estimates for an industrial era that starts with Julian year $t_0 = 1750$. Chapter 7 describes how evolution of global average temperature estimates for a preindustrial era are used to specify an initial condition for the industrial era. Chapter 8 couples numerically

integrable models of the evolution of global average temperature and atmospheric CO_2 concentration. Also, chapter 8 discusses extrapolations of future global average temperature based on extrapolations of radiative forcing. Chapter 8 provides examples of the effects using stratospheric sulfur injection to stabilize global average temperature. Chapter 8 also includes comments on how the results can be used in combination with global circulation models to support Climate Action Gaming Experiments (CAGE) [1]. The earlier chapters contain mostly verbal descriptions of methods used, to be following later with graphs of results and the associated equations. The parameters used to produce those graphs are mostly collected in a set of appendices. This approach makes it easier to find the constants used in the calculations for reference and minimizes the chance for inconsistencies between parameter values spread throughout the text and collected in summary tables, but it may require the reader interested in the parameter values to keep a separate copy of the appendices in view when reading the main text. In many cases, however, the approximate values of constant parameters can be inferred from visual inspection of figures containing graphs. The idea to make the overall methodology clear first, but also then become specific about the mathematical formulas used. Appendices B–O contain not only parameter values, but also instructions on how to access codes used to produce the parameter values. This information is included because those codes are expected to be comparatively stable, needing only updated input files when new supporting data becomes available. For the overall model calibration and extrapolations describedin chapters 7 and 8, the coding is expected to evolve as methodology is improved in the future. Those interested in accessing and using updated versions of those codes should contact the author at `cd7@illinois.edu` or through `acdis@illinois.edu`. Where formulas and numbers are given, the numbers are generally given with six digits. That is not to indicate the accuracy with which the numbers are estimated, but rather to allow for independent reproduction of the results without significant rounding error.

CHAPTER 2

DEMOGRAPHICS AND DEFORESTATION

The global population has doubled since the 1960s and continues to grow by about 80 million people every year. Even if most of this growth is in low consumption regions, all of these extra people need food, water, energy and shelter. Together, population growth and rising consumption are likely to increase demand for food by 70 percent by 2050 [3]. Increase in global human population has been correlated with various impacts on greenhouse gas emissions and thus on global average temperature. Also, decrease in the area of land covered by forest is related to both the average albedo of the earth and is an indicator depletion of an energy source, the depletion of which helped simulate the use of fossil fuels. This chapter describes calibration of models of the evolution of global population and deforestation.

2.1 Demographics

Historical population data from work by Angus Maddison for population from 1820–2008 and data and projections from the United Nations (UN) from 2008 to 2100 are used here [4]. The source data is shown in Appendix Table B.1 in detail. Global population growth was previously exponential over a early industrial base level, but cannot continue exponentially or even linearly forever. This observation suggests a logistic function model plus a constant, which turns out to produce a useful fit to historical data and UN extrapolations. A non-linear least square method is applied to fit the population estimates. A logistic function of the form $u = b_1/(1 + e^{-(t-b_2)/b_3})$ is used extensively in this thesis. For the population fit, the parameters b_1, b_2, and b_3 are listed in table B.2. A plot of the population fit is given in figure 5.1, and the constant added to the logistic function is given in the legend to figure 5.1.

2.2 Deforestation

Forests have played a significant role in human life. However, due to the development of human society and a growing population, reduction of forest cover has taken place around the globe for than thousands of years. Due to logging, agricultural production and other economic activities, changes in land use have increased atmospheric CO_2 emissions. In particular, unsustainable logging practices produce CO_2 emissions when trees are felled and release the carbon they are storing into the atmosphere, where it mingles with greenhouse gases from other sources and contributes to global warming. Before the advent of the industrial revolution, most people resided in small, rural communities where their daily existences revolved around farming. But industrialization, starting slowly about 1750 and accelerating in the nineteenth century, marked a shift to powered, special-purpose machinery, factories and mass production. The steam engine played central roles in the industrial revolution, and spurred the rapid growth of all varieties of industry. Wood was initially used as the primary fuel for steam engines. Therefore, woods were cut down and deforestation became intertwined with human influences on the global climate. For the deforestation fit, the fitting parameters are listed in table C.3, and the plot is shown in figure 5.2.

In the present work, historical data for the area covered by forest in the globe from 1800 to 2015 have been used. The source data are shown in Appendix C in Table C.1. The deforestation estimates from 1800–2010 used here are from a 2012 State of the World's Forest report [5], which estimates an initial total global forest cover of six billion hectares (6 Gha) before significant anthropogenic deforestation. To these deforestation estimates are added the 2010 value from that report and the additional deforestation by 2015 estimated by Keenan et al. [6]. Under the assumption that deforestation can be modeled with a logistic function, a non-linear least square method was used to fit with those data.

CHAPTER 3

CO_2, CH_4 AND N_2O EMISSIONS

The greenhouse effect is a natural process that warms the Earth's surface. When the Sun's energy reaches the Earth's atmosphere, some of it is reflected back to space, and the rest is absorbed and re-radiated by greenhouse gases. The absorbed energy warms the atmosphere and the surface of the Earth. However, human activities—particularly burning fossil fuels (coal, oil and natural gas), agriculture and land clearing—are increasing the concentrations of greenhouse gases. This is the enhanced greenhouse effect, which is contributing to warming of the Earth. Greenhouse gases include water vapour, carbon dioxide, methane, nitrous oxide, ozone and some halogen compounds including chlorofluorocarbons (CFCs). This chapter will discuss the CO_2, CH_4 and N_2O emissions.

3.1 CO_2 emissions

Carbon dioxide is an important greenhouse gas, which traps escaping heat energy, causing some of heat energy to pass back to the surface and thus keep our planet warm. The continual increase in the carbon dioxide concentration in the atmosphere is considered to be the main contributor to the global temperature increase known as global warming.

Humans burn fossil fuels, primarily coal, oil, and natural gas. The energy released is used to power cars and other machines, to generate electricity, and to keep buildings warm. The burning fuel releases waste gases, including carbon dioxide. As the human population increases, more fuel is used, and more carbon dioxide is released. There is an additional but comparatively small industrial carbon dioxide release from use of cement.

In this section, the effect of carbon dioxide is discussed. This section is divided into two different processes: carbon dioxide emitted from land use changes and from industry. The

fraction of emitted CO_2 that is retained in the atmosphere decreases with increasing temperature and increasing surface ocean mixed layer acidity. For simplicity for the historical period calibration, this evolution is modeled by using a different constant proportion of the emitted CO_2 from each of the two sources is retained in the atmosphere. This approach is sufficient for the present purposes because it provides a good fit to the historical evolution of atmospheric CO_2 concentrations. For the extrapolation described in a later chapter, however, numerical integration of a model containing the dominant effect of changes in atmospheric CO_2 concentration on retention in the atmosphere of emitted CO_2.

3.1.1 Industrial CO_2 emissions

A logistic plus to carbon emissions from fossil fuel use and cement production from year 1751 to 2017 has been use here. Boden et al. [7] give the total amount of carbon dioxide emitted due to fossil fuel use and cement production from year 1751 to 2014. For data in year 2015 to 2017, Jackson's data are used [8]. The fitting parameters are listed in table D.1, and the fit is plotted in figure 5.3.

3.1.2 CO_2 emissions from land use changes

By using annual net flux of carbon to the atmosphere resulting from land use change from year 1850 to 2005, the carbon contents are fitted with a constant times the time derivative of the logistic fit to cumulative deforestation, plus four Gaussians. It is assumed that the land use changing rate is proportional to rate of cumulative global deforestation. In order to get the estimated carbon dioxide concentration before the industry revolution, data are used from Law Dome Ice Cores from year 200 to 2004 [9, 10, 11, 12, 13] and data provided by National Oceanic and Atmospheric Administration (NOAA) from year 1979 to 2016 are used [14]. The concentration value for 2017 is estimated by multiplying the year 2016 data of NOAA by a factor of the quotient of year 2017 data of NOAA and the year 2016's. Also, the data from year 1 to 1978 of Law Dome Ice Cores are rescaled by a factor equal to quotient of year 1978 data of NOAA and the year 1978 of Law Dome. Then, the rescaled historical

data from year 200 to 1749 are fitted with a constant 281.795 parts per million (ppm) by volume plus a logistic function.

The Gaussian functions used in this thesis have the form $b_1 e^{-((t-b_2)/b_3)^2/2}/\sqrt{2\pi}$. The fitting paramters for the fits to carbon emissions from land use changes are listed in tables E.1–E.4, and a plot of the fit is given in figure 5.4.

3.2 CH_4 emissions

Methane in the earth's atmosphere is a strong greenhouse gas. However, methane has a large effect but for a relatively brief period, having an estimated lifetime of 8.9±0.6 years in the atmosphere [15], whereas carbon dioxide has a small effect for a long period, having an estimated lifetime of over 100 years.

Anthropogenic methane emissions occur during the industrial production or processing of natural gas [16]. Agriculture is another significant anthropogenic methane source [2].

Estimates of annual methane emissions for 1970–2012 are available from the European Joint Research Centre (EC-JRC) [17]. Estimates of atmospheric methane concentrations are available from years 1–2004 from Law Dome ice cores [9, 10, 11, 12, 13], from 1979– 2016 from Butler et al. [18], and from the NOAA from 1984–2017 [16]. To obtain estimates of methane emissions for years other than 1970–2012, an estimate of the atmospheric lifetime for methane was first made a least squares fit to equation 3.1 solved for t_{mlife} using the EC-JRC data for S_{CH_4} and the atmospheric concentrations for years 1970–2012.

The methane concentration governing equation is as follows:

$$\frac{\mathrm{d}<\mathrm{CH_4}>}{\mathrm{dt}} = \mathrm{S_{CH_4}} - \frac{<\mathrm{CH_4}> - <\mathrm{CH_4}>_0}{t_{\mathrm{mlife}}} \tag{3.1}$$

where left hand side of equation 3.1 represents the rate of change of atmospheric methane concentration, and S_{CH_4} is the source term of methane, which is the annual methane emission. $<CH_4>_0$ is estimated by fitting to a constant plus a logistic function for the atmospheric methane concentration data from years 200 to 1749. Here, the estimates of initial concentra-

tion of methane at the end of 1749 is 732.138 parts per billion (ppb) by volume, consistent with the graph shown in figure 5.5.

For other years, S_{CH_4} was estimated from the atmospheric concentrations using equation 3.1. For these purposes, $d<CH_4>/dt$ was estimated using the difference from before and after the year of the emission rate estimate divided by 2.

From a least squares fit, the atmospheric lifetime $t_{\text{mlife}} = 9.50694$ years was computed. The upper limit of the range referenced above and derived from a different database was 9.5 years. Though, the atmospheric lifetime of methane depends on the method used to estimate it, it is short compared to the time scale for global warming. Here, S_{CH_4} is from the historical data provided by EC-JRC from year 1970 to 2012, which represents the estimated annual anthropogenic emission. Then the average value of estimated annual methane anthropogenic emission from year 1750 to 2016 was computed, and the mean of fitted estimated emission from year 1750 to 2016 was evaluated as well. The ratio of these two average values 1.00918 was used to rescale the methane annual emission data from 1750 to 2016. Later, these rescaled data are fitted with a logistic function to get the post-1749 anthropogenic increase in methane emissions.

3.3 N_2O emissions

Nitrous oxide is emitted during agricultural and industrial activities, as well as during combustion of fossil fuels and solid waste. Although relatively small amounts are released compared with carbon dioxide, it has a high "global warming potential" (310 times that of carbon dioxide) [19]. A similar approach to that used for CH_4 emissions is used to fit N_2O emissions.

Estimates of annual nitrous oxide emissions for 1970–2012 are available from the European Joint Research Centre (EC-JRC) [17]. Estimates of atmospheric nitrous oxide concentrations are available from years 200–2004 from Law Dome ice cores [9, 10, 11, 12, 13], from 1979–2016 from Butler et al. [18]. To obtain estimates of methane emissions for years other than 1970–2012, an estimate of the atmospheric lifetime for nitrous oxide was first made a least squares

fit to equation 3.2 solved for t_{nlife} using the EC-JRC data for S_{N_2O} and the atmospheric concentrations for years 1970–2012.

$$\frac{d<N_2O>}{dt} = S_{N_2O} - \frac{<N_2O> - <N_2O>_0}{t_{nlife}} \tag{3.2}$$

where left hand side of equation 3.2 represents for the rate of change of atmospheric concentration of nitrous oxide. $<N_2O>$ is the atmospheric concentration of nitrous oxide. S_{N_2O} is the source term which amounts to annual emission in units of ppb/yr. $<N_2O>_0$ is estimated by fitting to a constant 262.150 plus a logistic function for the atmospheric nitrous oxide concentration data from years 200 to 1749. Here, the estimates of initial concentration of nitrous oxide at the end of 1749 is 267.2913 ppb, consistent with the graph shown in figure 5.7.

For other years, S_{N_2O} was estimated from the atmospheric concentrations using equation 3.2. For these purposes, $d<N_2O>/dt$ was estimated using the difference from before and after the year of the emission rate estimate divided by 2.

By a least square fit, the atmospheric lifetime $t_{nlife} = 128.012$ years was computed. The Law Dome data from year 1 to 1978 were rescaled by a factor of 0.996028, which is the ratio of year 1979 nitrous oxide concentration data of NOAA with year 1979 nitrous oxide concentration data of law dome. Then, from years 200 to 1749, the data is fitted with a constant 262.150 ppb by volume plus a logistic function. After that, the data from year 1750 to 2016 was rescaled by a factor of 1.00396, which is the ratio of the means of the EC-JRC and emissions inferred from the $<N_2O>$ data and the atmospheric lifetime, with both averages taken over the 1970–2012 years for which the EC-JRC give emissions estimates. Then, the nitrous oxide concentrations are approximated as the year 2016's data plus the difference between year 2016 and 2015's to estimate the $<N_2O>$ in year 2017. Later, these rescaled data are fitted with a logistic function to get the post-1749 anthropogenic increase in nitrous oxide emissions.

CHAPTER 4

LONG WAVELENGTH RADIATIVE FORCING

Radiative forcing, measured in watts per square meter of surface, is a direct measure of the impact of recent human activities—including not just greenhouse gases added to the air, but also the impact of deforestation, which changes the reflectivity of the surface—are having on changing the planet's climate. However, radiative forcing also includes any natural effects that may also have changed during that time, such as changes in the sun's output (which has produced a slight warming effect) and particles spewed into the atmosphere from volcanoes (which generally produce a very short-lived cooling effect, or negative forcing).

Radiative forcing of greenhouse gases, the "greenhouse effect" is the most important cause of the current global warming trend. To understand the energy budget of global systems, it is necessary to estimate the radiative forcing for greenhouse gases, including carbon dioxide, methane, and nitrous oxide.

4.1 Carbon dioxide atmospheric concentration fit

The oceans play an important role in regulating the amount of CO_2 in the atmosphere because CO_2 can move quickly into and out of a surface ocean mixed layer. Once in the oceans, the CO_2 no longer traps heat. CO_2 also moves quickly between the atmosphere and the land biosphere.

As noted above, CO_2 concentrations in the atmosphere are increasing as a direct result of human activities such as deforestation and the burning of fossil fuels (e.g., coal, oil, and natural gas). Over the past 150 years, CO_2 concentrations in the atmosphere have increased by as much as 30 percent (from 280 to 400 ppm). The oceans' depths are able to hold much more carbon than the atmosphere because most of the CO_2 that diffuses into the

oceans reacts with the water to form carbonic acid, bicarbonate, and carbonate. However, mixing into the benthic ocean is such a slow process, so only a surface ocean mixing layer is accounted for herein.

In this section, the concentration of carbon dioxide in the atmosphere is integrated from year 1750 to 2017. A simple model was used to model the atmospheric concentration of carbon dioxide from 1750 through 2017 is as follows:

$$<\mathrm{CO_2}> = <\mathrm{CO_2}>_0 + \mathrm{a} \times \int_{\mathrm{t_0}}^{\mathrm{t}} (r_{\mathrm{land}} + \mathrm{b} \times r_{\mathrm{industry}})\mathrm{dt} \tag{4.1}$$

where r_{industry} represents for the fit of estimated annual industrial carbon emissions in units of ppm, and r_{land} is the fit of estimated annual carbon emissions resulting from land use changes in units of ppm. The fraction of carbon emission due to two different process, that is land use changes and industry, are fitted by a least square scheme. Values of the fitting parameters a and b in equation 4.1 are given in equation 5.1, and plots of r_{land} and $r_{industry}$ are shown in figures 5.3 and 5.4 respectively.

4.2 Methane atomospheric concentration fit

The methane concentration governing equation is:

$$\frac{\mathrm{d}<\mathrm{CH_4}>}{\mathrm{dt}} = f(t) - \frac{<\mathrm{CH_4}>}{t_{\mathrm{mlife}}} \tag{4.2}$$

where

$$f(t) = \frac{b_1}{1 + e^{\frac{-(t-b_2)}{b_3}}}$$

Here, $\mathrm{b_1}$ is the constant in the anthropogenic methane emission rate equation plotted below in figure 5.6, $\mathrm{b_2}$ is the inflection year point for the logistic fit to post-1749 anthropogenic increase in methane emissions, and $\mathrm{b_3}$ is the early emission growth time which is the inverse of the early emission growth rate.

As noted above, the lifetime of methane in atmosphere is about 9.5 years. The early emission growth time of methane is about 41.4 years. The ratio of methane's lifetime to its

early emissions growth time is small, so it is convenient to use an expansion in powers of $\epsilon = t_{\text{mlife}}/b_3$ to solve the $<CH_4>$ balance equation. Keeping terms through second order in ϵ, and letting

$$y = \frac{<CH_4> - <CH_4>_0}{t_{\text{mlife}} * b_1} \tag{4.3}$$

evolve from y=0, t=t_0=1750, and approximate y as

$$y = u + \epsilon y_1 + \epsilon^2 y_2 \tag{4.4}$$

where u is the unit logistic function $1/(1 + e^{-x})$ gives

$$\epsilon \frac{dy}{dx} = u - y \tag{4.5}$$

where

$$x = \frac{t - b_2}{b_3}$$

Then, plug in y, and solve for the coefficients y_1 and y_2. Then, $y_1 = -u(1-u)$ and $y_2 = u(1-u)(1-2u)$. Thus,

$$y = u - u(1-u)\epsilon + \epsilon^2 u(1-u)(1-2u) \tag{4.6}$$

Therefore,

$$<CH_4> - <CH_4>_0 = t_{\text{mlife}} b_1 y \tag{4.7}$$

4.3 Nitrous oxide atmospheric concentration fit

In the case of nitrous oxide, it is the ratio of the initial emissions growth time b_3 of about 52 years to the atmospheric lifetime of t_{nlife} of 128 years that is instead small. Thus, it is convenient to use an expansion in powers of $\delta = b_3/t_{\text{nlife}}$ to solve the $<N_2O>$ balance equation. The equation can be rewritten as:

$$\frac{\mathrm{d}<\mathrm{N_2O}>}{\mathrm{dt}} = b_1 u - \frac{<\mathrm{N_2O}>}{t_{\mathrm{nlife}}} \tag{4.8}$$

where b_1 is the anthropogenic nitrous oxide emission rate plotted below in figure 5.8, and u is again $1/(1+e^{-x})$. Keep terms through first order in δ, and let

$$y = \ln(1+e^x) + \delta Li_2[-e^x] - \delta^2 Li_3[-e^x] \tag{4.9}$$

Here, Li_2 and Li_3 are polylogarithm functions of order 2 and 3 respectively. Then,

$$<\mathrm{N_2O}> - <\mathrm{N_2O}>_0 = t_{\mathrm{nlife}} b_1 y \tag{4.10}$$

In order to make a better fit for the nitrous oxide concentration, a logistic function correction is also included.

4.4 Non-linear radiative forcing formulas

To determine the total radiative forcing of the greenhouse gases, the non-linear formulas from IPCC [20] are used. These empirical expressions are derived from atmospheric radiative transfer models and generally have an uncertainty of about 10%. The uncertainties in the global average abundances of the long-lived greenhouse gases are much smaller (<1%). For the historical data period, linear approximations the non-linear formulas suffice. Use of the linear formulas permits use of analytic expressions for impacts on global average temperature. For numerically integrated extrapolations, however, the more accurate non-linear formulas need to be used, as described in a subsequent chapter.

Table 4.1. Non-Linear radiative formulas of greenhouse gases

Gases	Simplified Expression Radiative Forcing, $\Delta F(\mathrm{W/m^{-2}})$	Constant
CO_2	$\Delta F = \alpha \ln(C/C_0)$	$\alpha = 5.35$
CH_4	$\Delta F = \beta(M^{0.5} - M_0^{0.5}) - [f(M, N_0) - f(M_0, N_0)]$	$\beta = 0.036$
N_2O	$\Delta F = \epsilon(N^{0.5} - N_0^{0.5}) - [f(M_0, N) - f(M_0, N_0)]$	$\epsilon = 0.12$

The subscript "0" denotes the concentration of that species at year 1750. Also,

$$f(M,N) = 0.47 \ln\left[1 + 2.01 \times 10^{-5} \times (MN)^{0.75} + 5.31 \times 10^{-15} M(MN)^{1.52}\right] \tag{4.11}$$

Here C is <CO_2> in ppm, M is <CH_4> in ppb, N is <N_2O> in ppb.
For this case, C_0 = 278 ppm, M_0= 722 ppb, and N_0 = 270 ppb. A least square method is applied to fit with the two parameters in the proposed linear model. Then, the radiative forcing from the anthropogenic change in each species is estimated using the fitted linear approximation formulas.

4.5 Linear fitting of radiative forcing of CO_2, CH_4 and N_2O

To begin with, linear approximations to radiative forcings with respective to greenhouse gases concentrations are fit. In general, the linear forcing approximations follows the form of $f(X) = a(X - X_0)$, where the values of X_0 are the long-term limits of a logistic fits to the concentration of molecule X from a constant plus logistic fit for years 200 to 1749.
The procedure used is to plug in the previous long-term limits from that pre-industrial fit to the non-linear formulas as the initial fitted concentration of molecule X. Then, find the year 2017 concentration data of molecule X from NOAA globally averaged marine surface annual mean database as the maximum concentrations, divide the range between the maximum and minimum into 100 data points, and plug those data points into that non-linear equation. Then the linear equation used to fit the non-linear formula by using a least squares method. The linear equations with the two fitted parameters are plotted out and compared with the non-linear formulas shown in Table 4.1.

4.6 Radiative forcing estimates of "other" well mixed greenhouse gases and contrails

Generally, long wave radiation in the Earth's atmosphere is defined as the radiation at wavelengths longer than 4 µm (infrared) [21]. Like carbon dioxide, many non-CO_2 atmospheric

gases absorb in the infrared and contribute to climate forcing. Such gases include hydrofluorocarbons (HFCs), sulfur hexafluoride (SF_6), and perfluorocarbons (PFCs, which includes CF_4 and C_2F_6). Other classes of greenhouse gases are included in the Montreal Protocol for Substances that Deplete the Ozone Layer and its subsequent amendments and include chlorofluorocarbons (CFCs), halon, and chlorine- and bromine- containing (halogenated) solvents (like methyl chloroform (CH_3CCl_3), carbon tetrachloride (CCl_4), and bromochloromethane (CH_2BrCl)). Water vapor is a major greenhouse gas, but it is considered as a feedback in the climate system related to the human activities on other greenhouse gases and by changes in land use activity, rather than having its concentration in atmosphere modeled directly.

A significant fraction of the longwave radiation emitted by the surface is absorbed by trace gases in the air. Therefore, those well mixed greenhouse gases also play an important part in global warming effect. Contrails are thin cirrus clouds, which reflect solar radiation and trap outgoing heat. Therefore, it is significant to study the radiative forcing from well mixed greenhouse gases other than N_2O, CH_4, and CO_2, and from contrails as well.

In our case, by taking reference at the fig 8.6a in IPCC (2013) [2], the radiative forcing for "other" well mixed greenhouse gases are shown below: First of all, data from the "others"

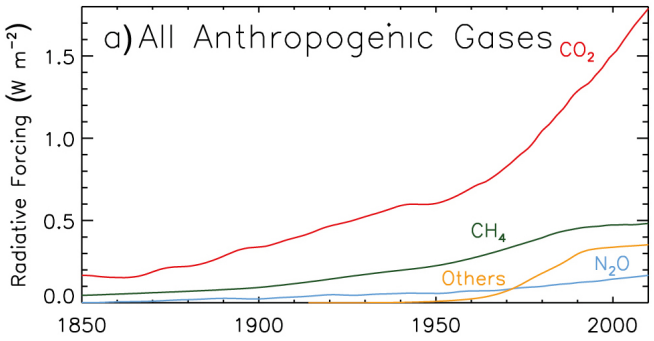

Figure 4.1. All Anthropogenic Gases [2]

plot which is shown above are extracted. The data points starting from year 1935 until 2010 are selected. Then, those data are fitted with logistic function.

In the ANNEX II Table AII.1.2 of IPCC (2013) [2], historical effective radiative forcings including land use change are shown. The contrail annual historical data from year 1750 to 2011 are selected and fit with a logistic function by a least square method.

CHAPTER 5

GREENHOUSE EFFECT RESULTS AND DISCUSSION

In this chapter, greenhouse effect results are shown and discussed.

5.1 Demographics

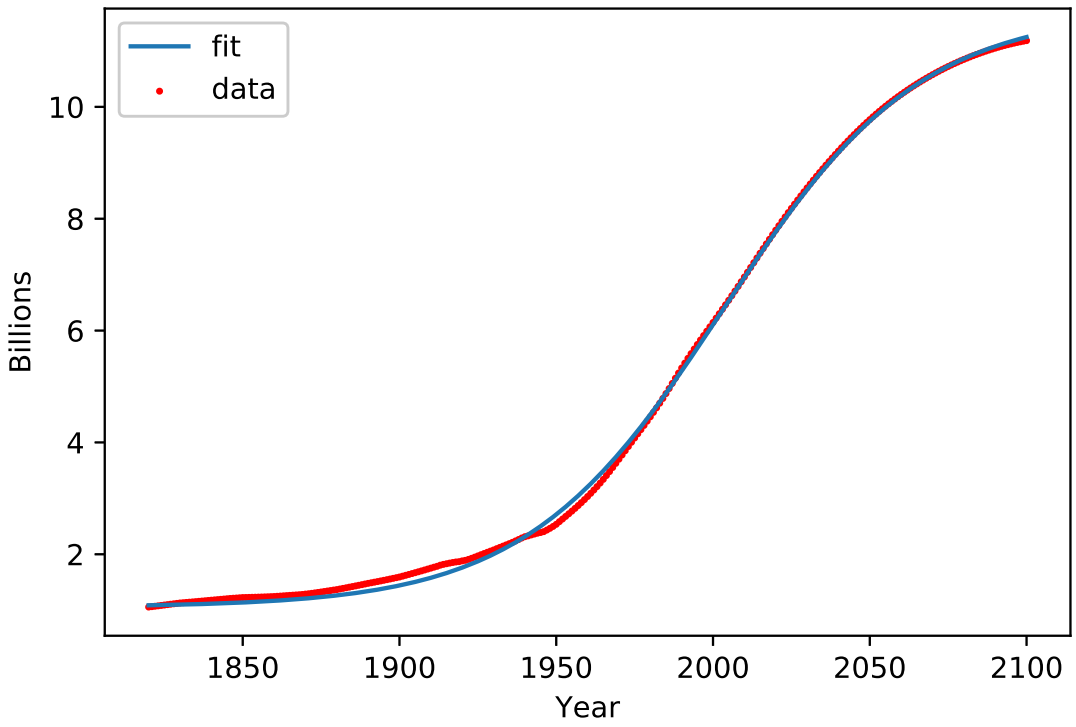

Figure 5.1. Logistic function plus a 1820 value of 1.05650 billion (curve), fit to estimates (dots) and extrapolations of global population.

Figure 5.1 shows that the population estimates used are fit well with a constant plus a logistic function. Around the year 2003, there is an inflection point. Before year 2003, the

population growth rate keeps increasing, but after that, growth rate of global population starts to decrease. Finally, the total population approaches a saturation state after the year 2100. The fitted parameters of global population are summarized in Table B.2 in Appendix B.

5.2 Deforestation

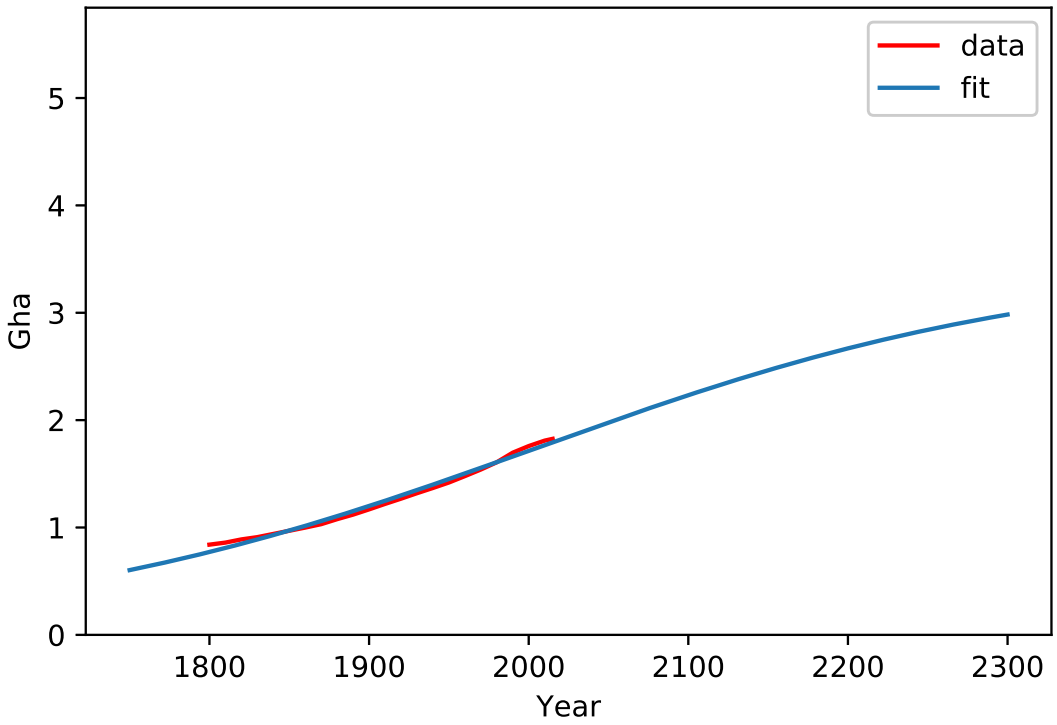

Figure 5.2. Logistic function fit to cumulative global deforestation estimation, with extrapolation back to 1750 and forward to 2200.

Figure 5.2 shows that, from the year 1800 to 2015, the global forested area kept decreasing. The historical data are fit well with logistic model, which extrapolates to a total deforestation of about three billion hectares (Gha), and by the year 2300 that limit will nearly have been reached. The deforested area from 1800 to 2015 are saved in Table C.2 in Appendix. The fitted parameters of deforestation are summarized in Table C.3 in Appendix C.

5.3 CO_2, CH_4, and N_2O emissions

This section discusses the anthropogenic-induced emissions of CO_2, CH_4, and N_2O, which are the main three greenhouse gases (GHGs) that contribute to global warming. The fitting parameters of CO_2, CH_4, and N_2O emissions are summarized in Table P.1 in Appendix P.

5.3.1 CO_2 emissions

Separate functional fits are made to estimates of industrial CO_2 emissions and of emissions of CO_2 from land use changes. Using the above-mentioned approximation that a different constant fraction of the emitted of CO_2 from each of these two sources was retained in the atmosphere allows for an overall increase in that fraction with time and provides a fit to the evolution of the atmospheric concentration. The fraction for land use is 0.271308 and for industry is 0.41108 respectively. In practice, the retention fraction for any given year does not depend appreciably on the type of source. But the approach used here allows for a gradual increase in the retention fraction of the total source.

Industrial CO_2 emissions: Figure 5.3 compares estimates of annual industrial carbon content of CO_2 emissions to a logistic fit. That figure shows that industrial emissions were very small before 1850, but that the carbon emission rate increased at a constant rate of 0.4%/yr, due to economic and population growth and technology changes with which anthropogenic carbon emissions are associated. The fitted parameters of industrial CO_2 emissions are summarized in Table D.1 in Appendix D.

CO_2 emissions from land use changes: Comparing the logistic function part of a fit to estimates of atmospheric carbon emissions from land use changes in figure 5.4, there are two big peaks after year 1950. After World War II, the carbon emissions from land use changes intensified in conjunction with post-war economic recovery. The first larger Gaussian function was added to compensate this effect. Similarly, the peak of second larger Gaussian function was added to represent the economic boost of developing countries, such as China and India.

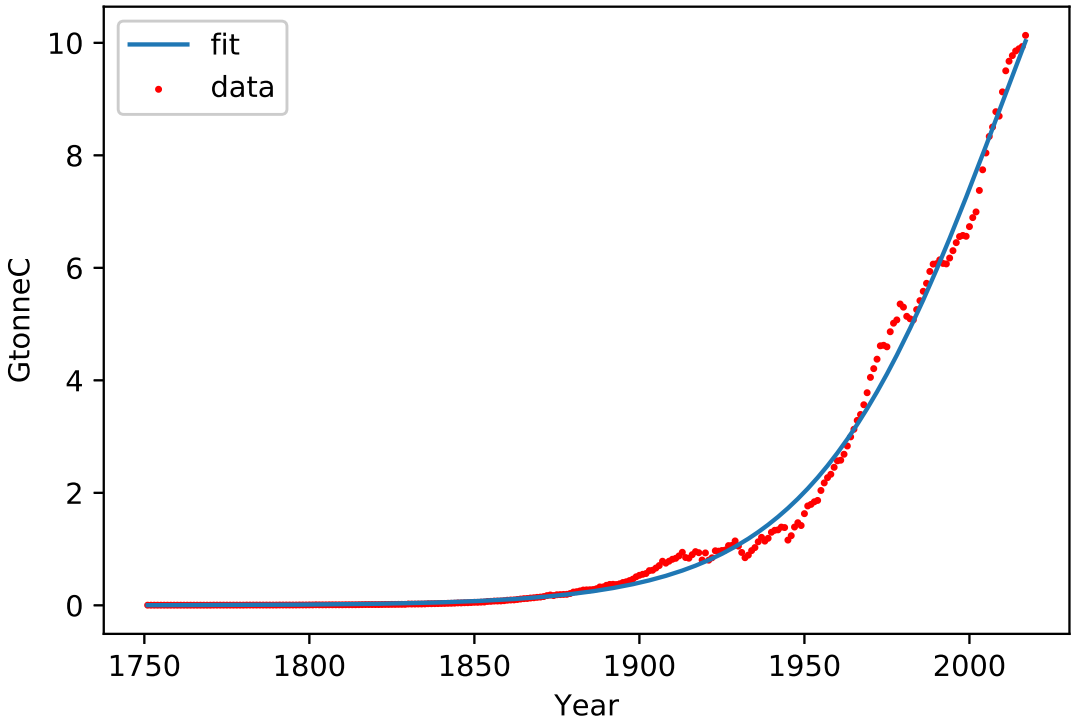

Figure 5.3. Logistic function fit to annual industrial carbon emissions.

5.3.2 CH_4 emissions

From the constant logistic function fit used to produce figure 5.5, the long-term limit of the logistic function part of the constant plus logistic fit to methane concentration from years 200 to 1749 was computed as 732.139 ppb.

However, from the points figure 5.6 derived as described in chapter 4, the annual methane emissions initially grew with a rate of 2.42%/yr after year 1750. It appears that human activities have disturbed the previously more nearly balanced methane cycle.

5.3.3 N_2O emissions

From the points in figure 5.8 alone, derived as described in chapter 4, it is difficult to judge the long-term tendency of nitrous oxide concentration in atmosphere. This is because the

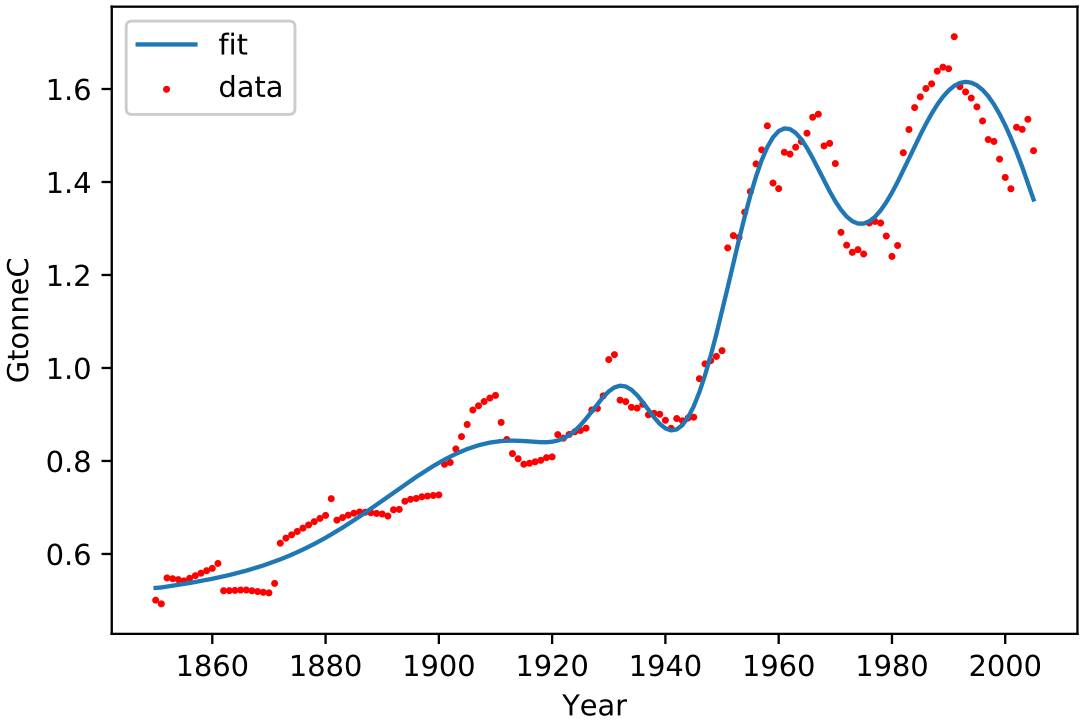

Figure 5.4. Fit (curve) of the time derivative of a logistic function plus four Gaussians, compared to estimates of annual atmospheric carbon emissions from land use changes.

atmospheric lifetime of N_2O is about 128 years, making it the historical concentrations far from steady state. Therefore, the same inflection time for the increment in global population over its year 1820 value used when fitting it with a two parameters' logistic function. The pre-industrial limit of the constant of 287.2913 ppb used in equation 4.1 was computed from a logistic function fit to methane concentrations from years 200 to 1749 as shown in figure 5.7. A logistic fit to the resulting annual emissions estimate is shown in figure 5.8.

5.4 <CO_2>, <CH_4> and <N_2O> fit

5.4.1 <CO_2> fit

Figure 5.9 shows that the concentration of CO_2 was almost kept constant at 280 ppm by volume for about 1000 years prior to the industrial era. Because the carbon being removed

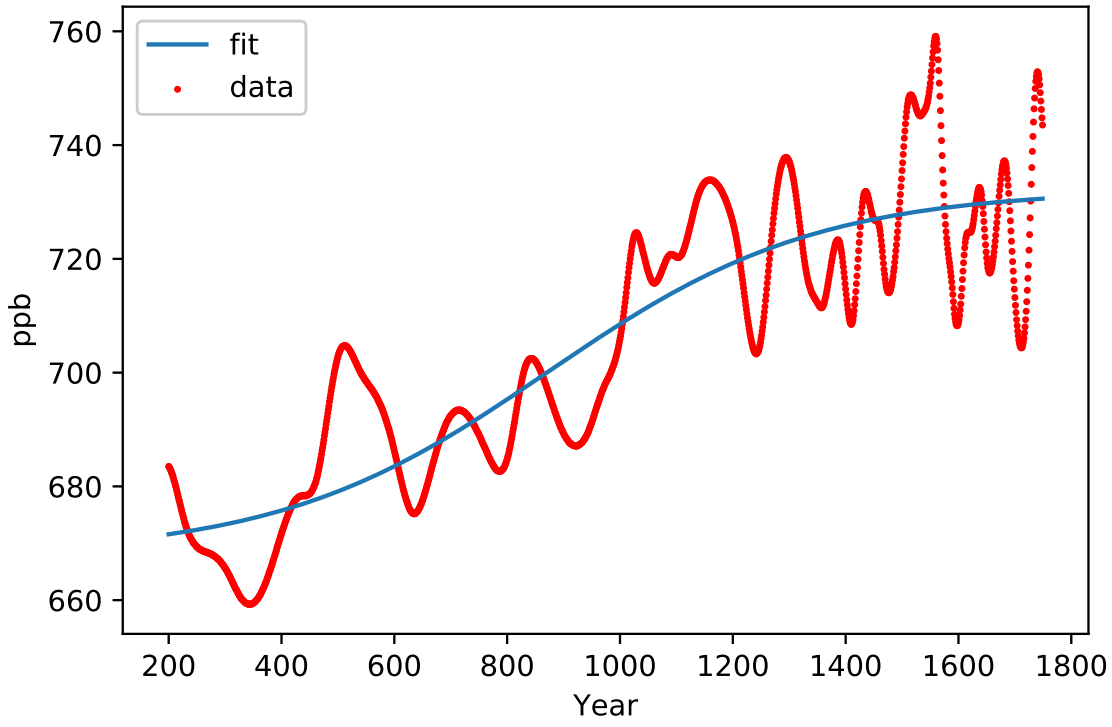

Figure 5.5. A constant 667.982 ppb plus a logistic function fit to estimates of the atmospheric methane concentration from years 200–1749.

from the atmosphere in some places nearly exactly matched the CO_2 being added to the atmosphere in other places, a nearly steady state atmospheric concentration had been reached over a century before year 1750. The long-term limit of a constant plus logistic fit to carbon dioxide concentration from years 200 to 1749 shown in figure 5.7 was computed as 277.8529 ppb. However, since year 1750, the carbon dioxide kept growing, with an average annual rate of 2.11 ppm per year over years 2005 to 2015.

The fitted carbon dioxide concentration formula is as follows:

$$<CO_2> = <CO_2>_0 + 0.271308 \times \int_{t_0}^{t} (r_{\text{land}} + 1.51518 r_{\text{industry}}) \text{dt} \tag{5.1}$$

where r_{industry} represents 1/2.13 times the fit to GtonneC/yr industrial carbon emissions shown in figure 5.3, and r_{land} denotes 1/2.13 times the fit to GtonneC/yr from land use changes shown in figure 5.4. By comparing figures 5.3 and 5.4, the increase in industrial

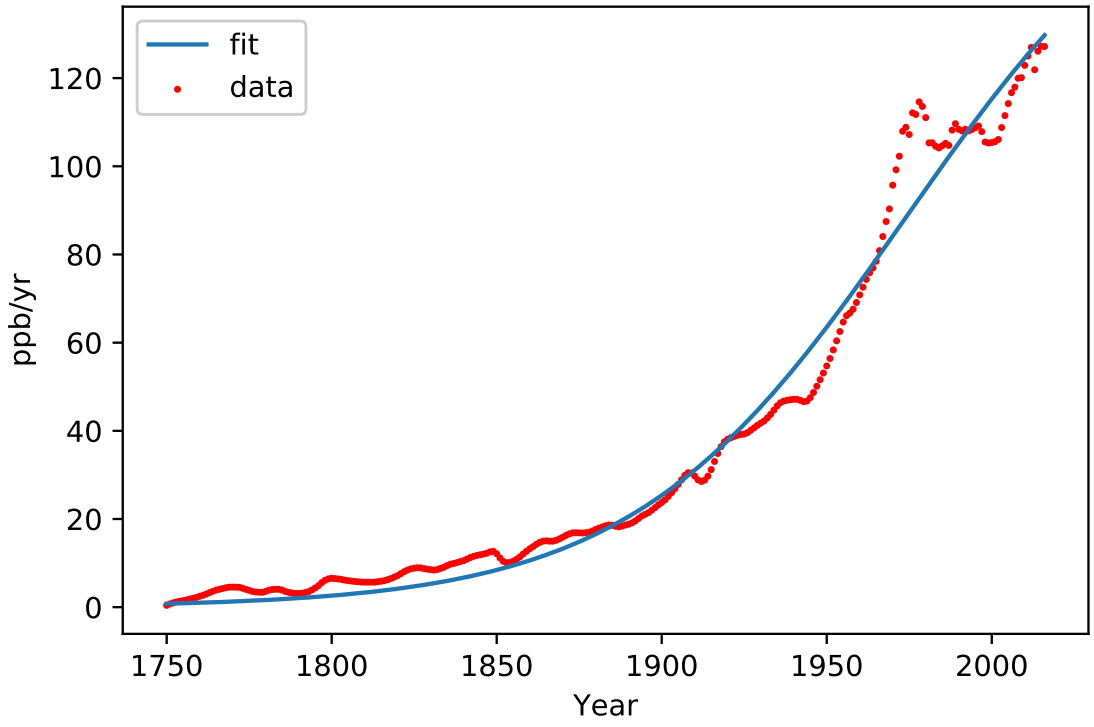

Figure 5.6. Logistic fit to post-1749 anthropogenic increase in methane emissions, expressed in terms of the rate of increase of atmospheric methane concentration that would result if all of such emissions were retained in the atmosphere.

carbon emissions comes later than the increase in carbon emissions from land use changes. Thus, the factor 1.51518 represents the increment as a result of emitting carbon retained in the atmosphere with rising global average temperature and $<CO_2>$. The results are shown in figure 5.10.

5.4.2 $<CH_4>$ fit

For the fit shown in figure 5.11, the integrated atmospheric methane concentration equation is estimated by using equation 4.7.

The initial $<CH_4>_0$ is 722.065 ppb at year 1750. It is clear that methane concentration has kept growing since 1750, and it is sufficient to use the approximate analytic integration formula in equation 4.5 to fit with the estimates of methane concentration.

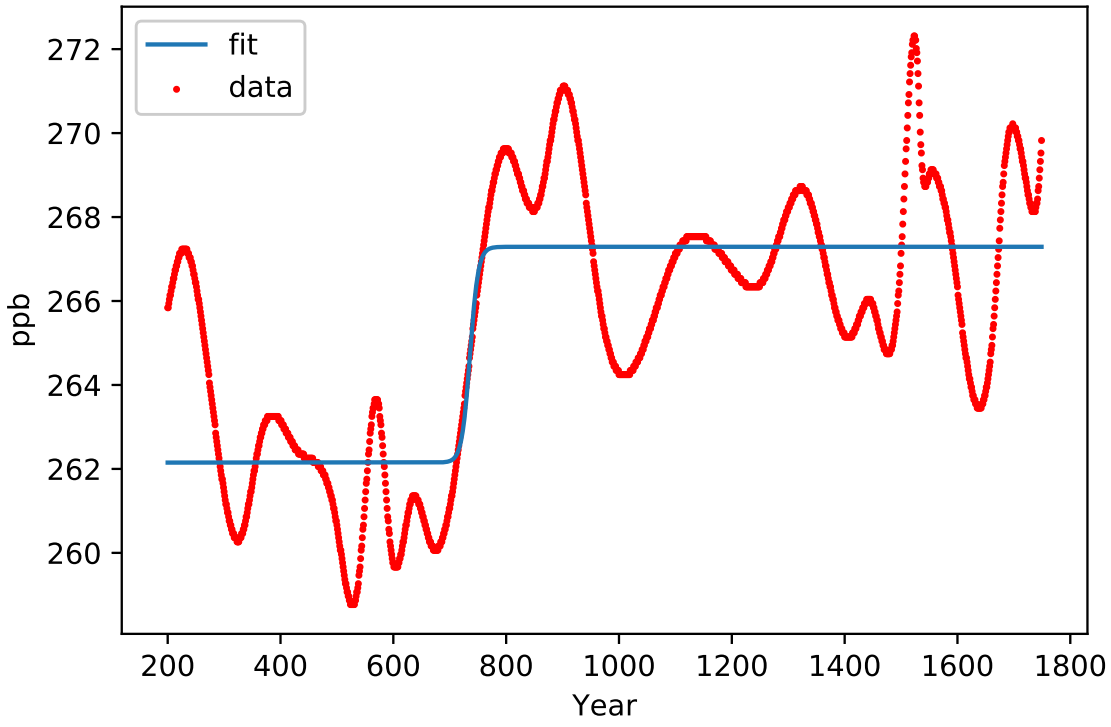

Figure 5.7. A constant 262.150 ppb plus a logistic function fit to estimates of the atmospheric nitrous oxide concentration from years 200–1749.

5.4.3 $<N_2O>$ fit

For the fit shown in figure 5.12, the integrated atmospheric nitrous oxide concentration equation is estimated by using equation 4.10.

The initial $<N_2O>_0$ is 267.2913 ppb. However, compared with methane integration, a logistic correction is used to get a better fit to early industrial era values of $<N_2O>$, up to about 1955. The formula for that correction is $b_1(1 - 1/(1 + e^{-(t-b_2)/b_3}))$, where the values of parameters b_1, b_2, and b_3 are shown in table I.1.

5.5 Total long wavelength radiative forcing

After the formulas for concentration of the three main greenhouse gases are derived, it is necessary to relate the concentration of each species to their corresponding radiative forcings.

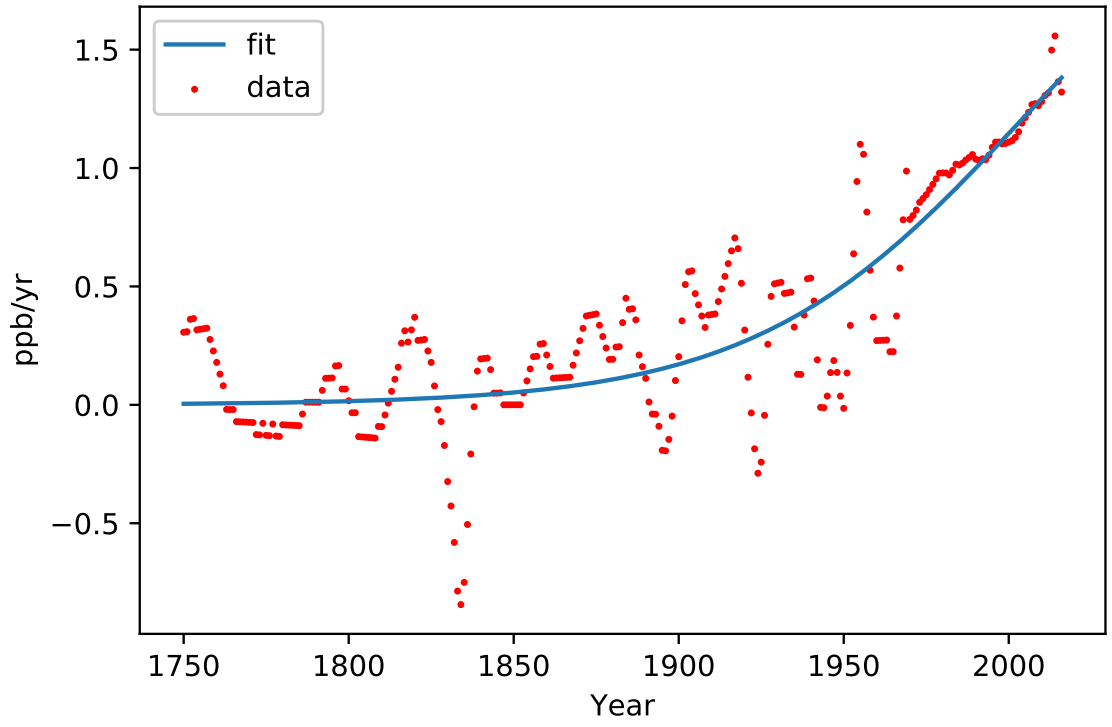

Figure 5.8. Logistic fit to post-1749 anthropogenic increase in nitrous oxide emissions, expressed in terms of the rate of increase of atmospheric nitrous oxide concentration that would result if all of such emissions were retained in the atmosphere.

Figure 5.13 shows the radiative forcing of $<CO_2>$ as a function of its atmospheric concentration. The fitted linear equation is:

$$y = 0.01653708 \times (x - 277.8529) \tag{5.2}$$

For methane case shown in figure 5.14, the fitted linear equation is:

$$y = 0.00048336 \times (x - 732.1388) \tag{5.3}$$

For nitrous oxide case shown in figure 5.15, the fitted linear equation is:

$$y = 0.00309776 \times (x - 267.2913) \tag{5.4}$$

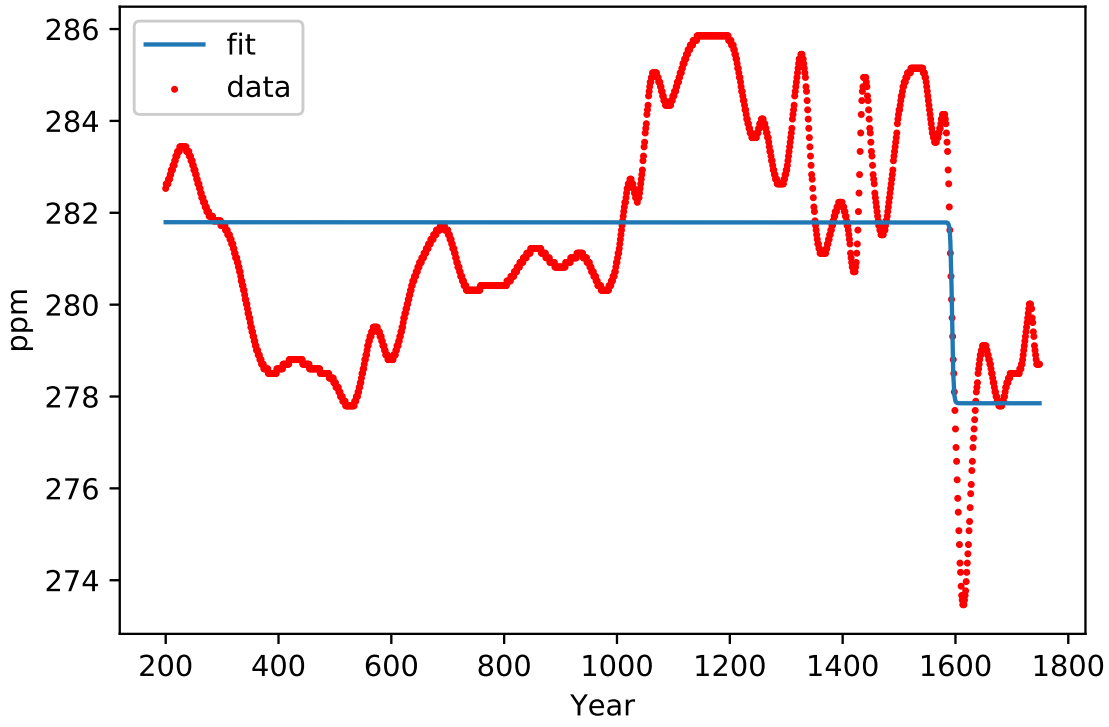

Figure 5.9. A constant 281.795 ppm plus a logistic function fit to estimates of the atmospheric carbon dioxide concentration from years 200–1749.

where y is the radiative forcing in units of W/m^2, and x is the concentration of species X. For carbon dioxide, concentration x is in units of ppm, while for methane and nitrous oxide, concentration x is in units of ppb. The linear fitting formulas for these three GHGs are summarized in Table M.1.

In figure 5.16, the above-mentioned "other greenhouse gas radiative forcing" is plotted along with a logistic function fit. The fitting parameters are listed in table J.2. Since year 1960, the total radiative forcing resulting from these other greenhouse gases has increased with an initial annual growth rate of 13.63% per year. After that, the radiative forcing fit approaches a plateau. However, compared with carbon dioxide, the forcing remains small.

For the fit shown in figure 5.17, the radiative forcing of contrails grows with an initial annual rate of 5.6142% per year. The fitting parameters are listed in table J.3. However,

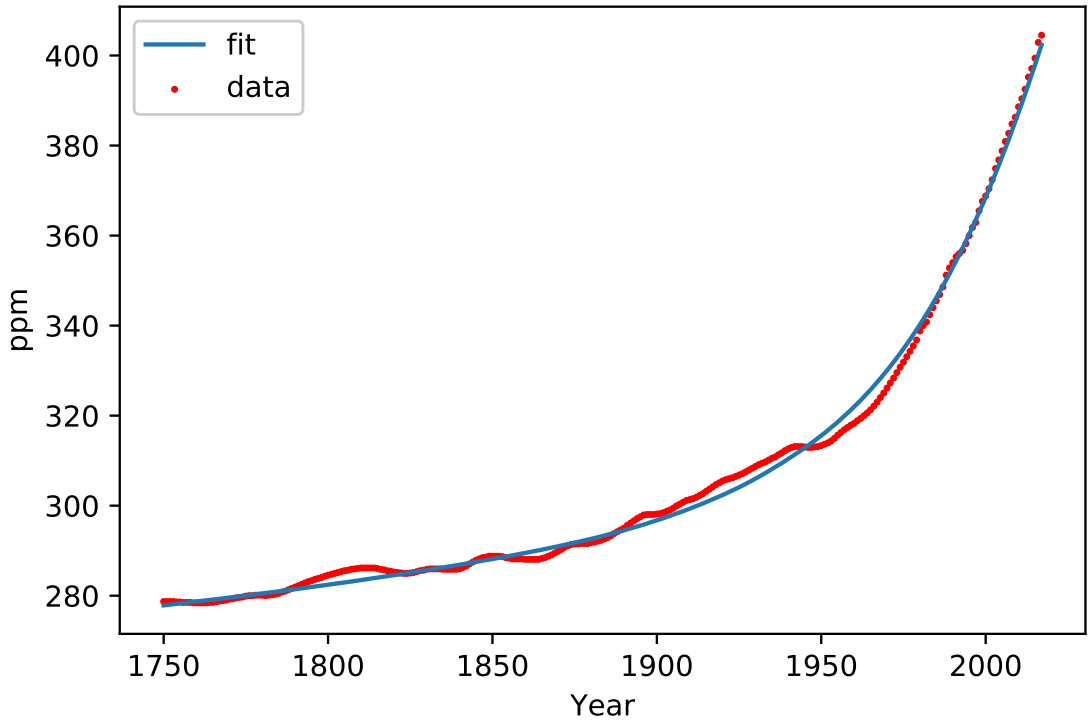

Figure 5.10. Data (dots) and fit (curve) to <CO_2>.

even the extrapolated long term limit of radiative forcing from contrails is small compared with greenhouse gases.

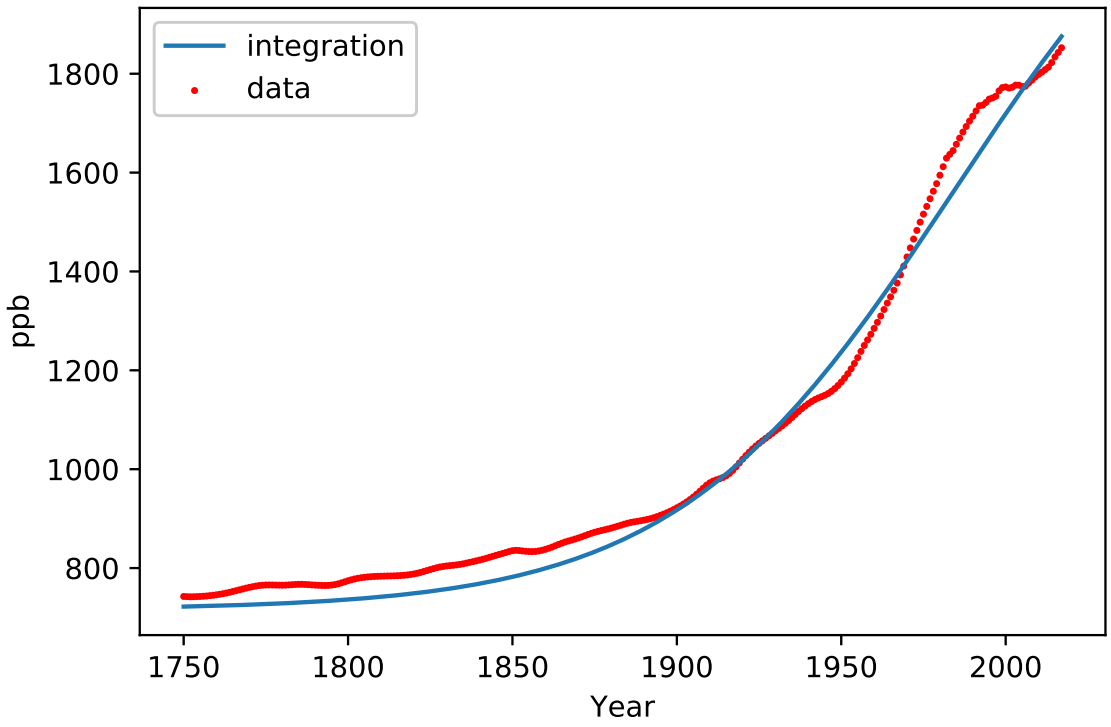

Figure 5.11. Integration of CH_4 emissions expanded through second order in the ratio of the atmospheric lifetime to the early growth time (curve) and estimates of $<CH_4>$ (dots).

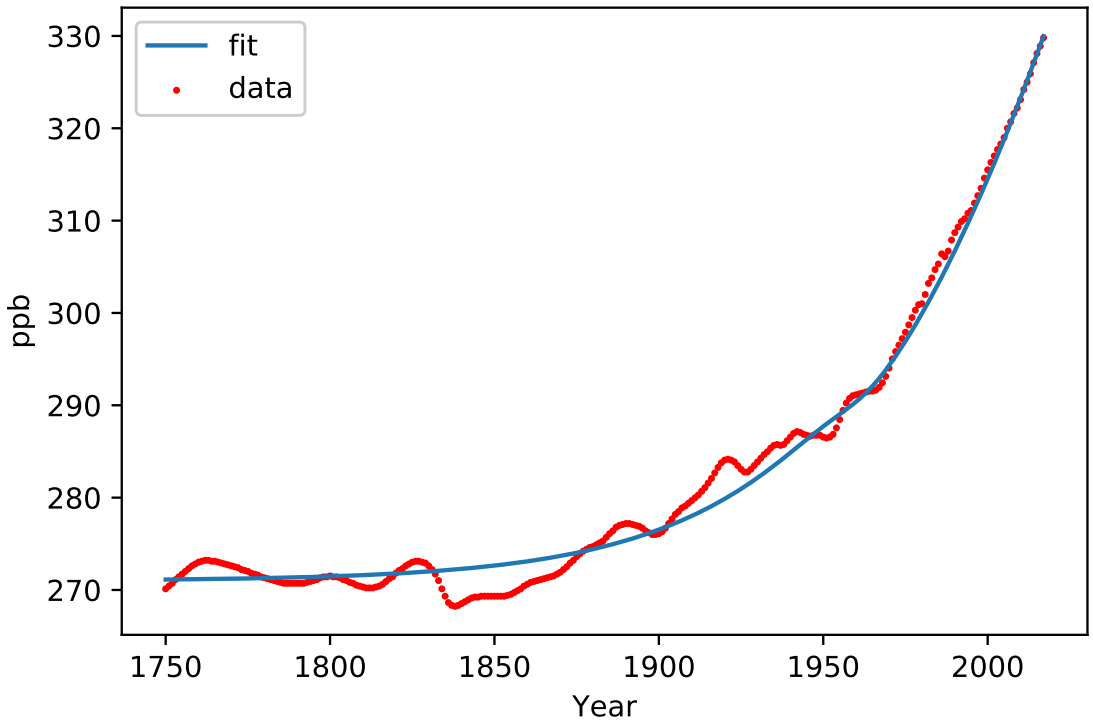

Figure 5.12. Integration of N_2O emissions expanded through second order in ratio of the atmospheric lifetime to the early growth time to atmospheric lifetime plus a logistic function (curve), and estimates of $<N_2O>$ (dots).

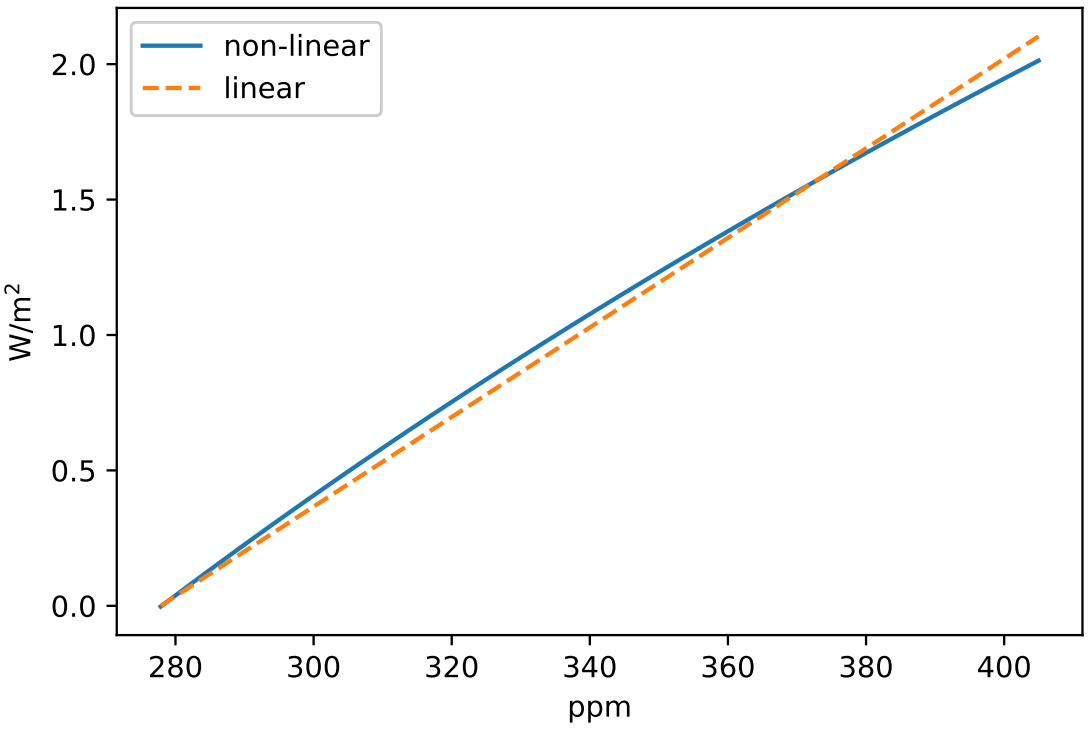

Figure 5.13. Linear (dashed line) approximation to the non-linear <CO_2> radiative forcing formula.

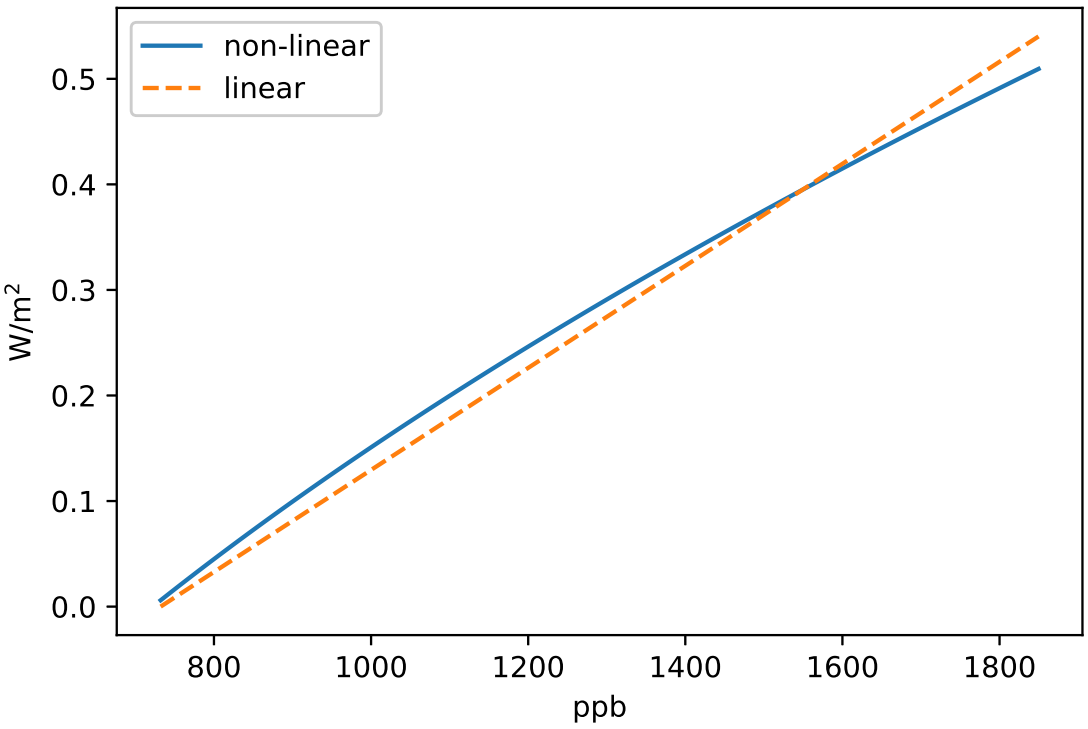

Figure 5.14. Linear (dashed line) approximation to the non-linear <CH_4> radiative forcing formula.

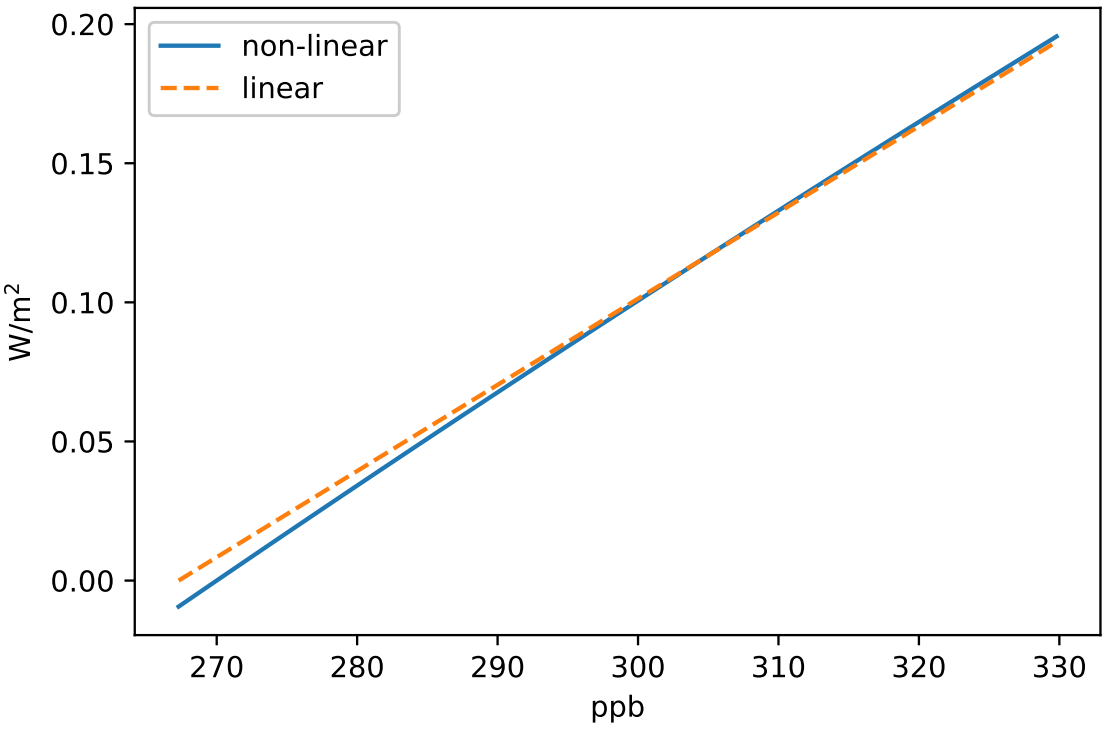

Figure 5.15. Linear (dashed line) approximation to the non-linear <N_2O> radiative forcing formula.

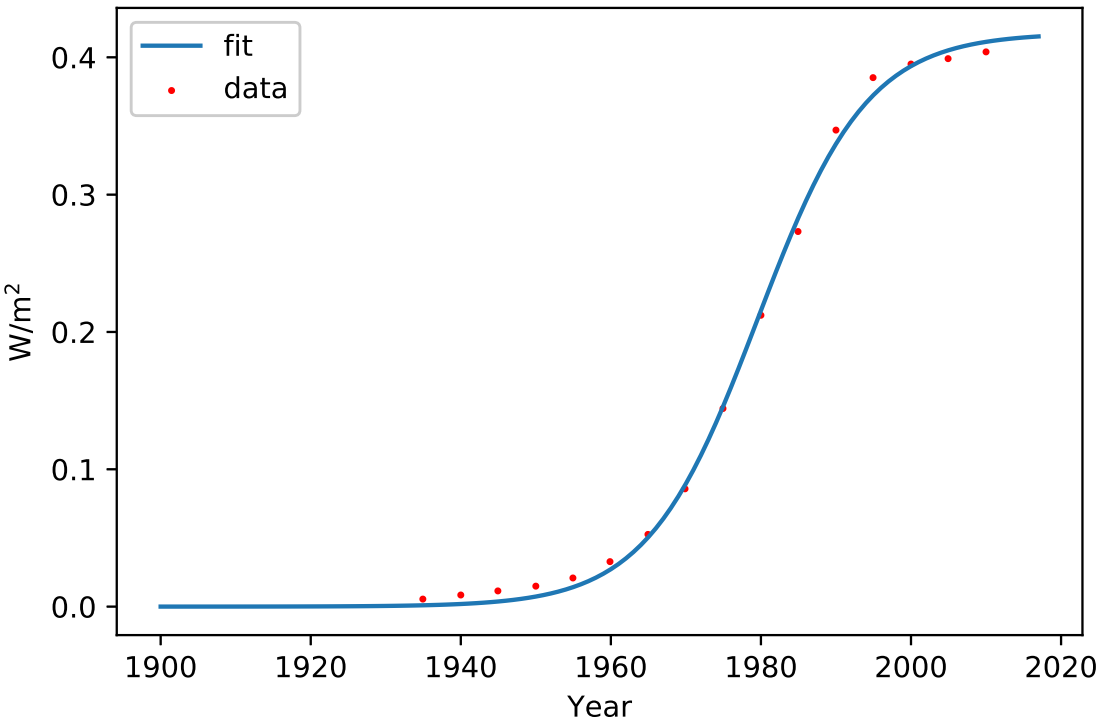

Figure 5.16. Logistic fit to radiative forcing estimates from 1935–2010 from well mixed greenhouse gases other than N_2O, CH_4, and CO_2.

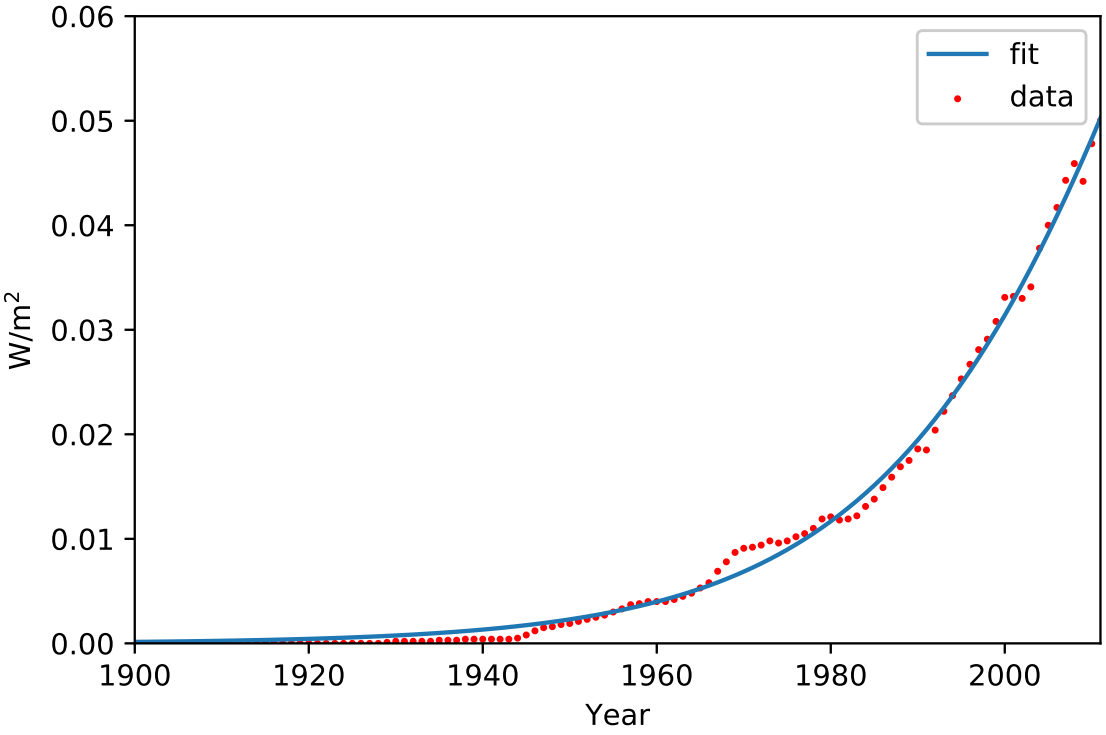

Figure 5.17. Logistic fit to estimates of radiative shielding by contrails.

CHAPTER 6

SHORT WAVELENGTH IRRADIANCE VARIATION, SHIELDING AND TROPOSPHERIC OZONE

Part of the solar energy that comes to Earth is reflected back out to space in some of the same, short wavelengths in which it came to Earth. The fraction of solar energy that is reflected back to space is called the albedo. Different parts of the Earth have different albedos. Over the whole surface of the Earth, about 30 percent of incoming solar energy is reflected back to space [22]. This chapter provides formulas for shielding of short wavelength radiation. These include influences on albedo from land-use changes, anthropogenic tropospheric aerosols, less the effect of black carbon on snow, stratospheric ozone and volcanic shielding. The formulas are for the absolute value of the radiative forcing, so those formulas must be substracted from long wavelength forcing to get net effective radiative forcing. Also, formulas for cosinusoidal variations solar irradiance per square meter of the earth's surface are provided, which will be added to long wavelength net radiative forcing to get overall radiative forcing. Although it affects long wavelength radiation, forcing from tropospheric ozone is included in this section because the fitting procedure for it is similar to the used for shielding dominated by tropospheric aerosols.

6.1 Influence on albedo from land use changes

Changes in land surface albedo can result from land-use changes and thus be tied to an anthropogenic cause. The largest effect is estimated to be at high latitudes where snow-covered forests that have a lower albedo have been replaced by snow-covered deforested areas [23]. Bright surfaces reflect radiation and cool the climate, whereas darker surfaces absorb radiation and produce a warming effect. Figure 6.1 shows a fit to estimates of radiative shielding via changes in albedo due to land use changes [2]. The fit uses a logistic

function plus the time derivative of a logistic function. The approximate linear portion of the curve in figure 6.1 is due to contribution of linear radiative forcing of atmospheric carbon dioxide from land use changes. However, the radiative shield effect of albedo changes due to land use changes is not completely proportional to radiative forcing from the contribution of $<CO_2>$ from land use changes. Therefore, the derivative of a logistic function in figure 6.1 is used instead of the sum of four Gaussian functions in the case of radiative forcing from the contribution to $<CO_2>$ from land use.

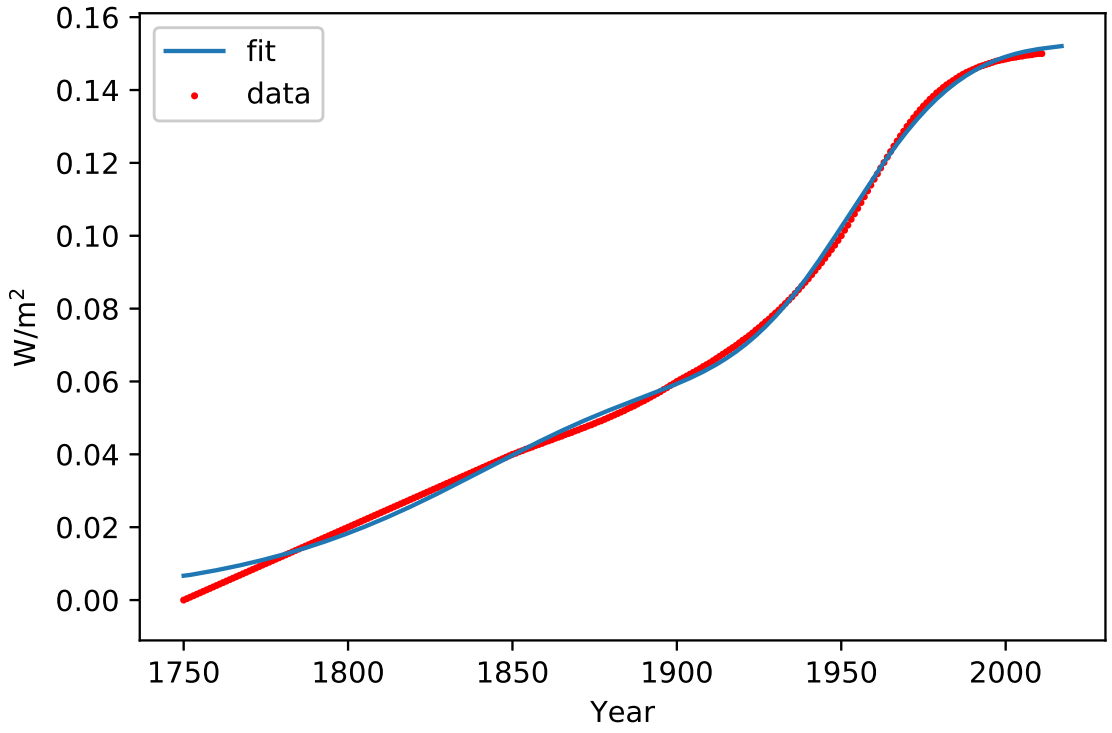

Figure 6.1. Radiative shielding estimates for albedo changes, fit with a logistic function plus a constant times the time derivative of the unit logistic function u.

6.2 Anthropogenic aerosols and black carbon on snow

The Sun provides the energy that drives the earth's climate, but not all of the energy that reaches the top of the atmosphere finds its way to the surface. Due to in part to aerosols—

and clouds seeded by them—about a quarter of the sun's energy is reflected back to space. Aerosols can have a significant impact on climate when they scatter light. Figure 6.2 shows a fit to the net radiative shielding from anthropogenic aerosols and radiative forcing from black carbon on snow. These are combined because they both have significant contributions from industrial activities. The fitting function is a constant times the deforestation rate, plus a Gaussian function. The deforestation rate is taken to a measure of early industrial activities, assuming that deforestation encouraged the burning of coal. The Gaussian function accounts for an increase in tropospheric ozone during a post World War II increase before imposition of effective pollution controls. The fitting parameters for the gaussian function are listed in table K.1.

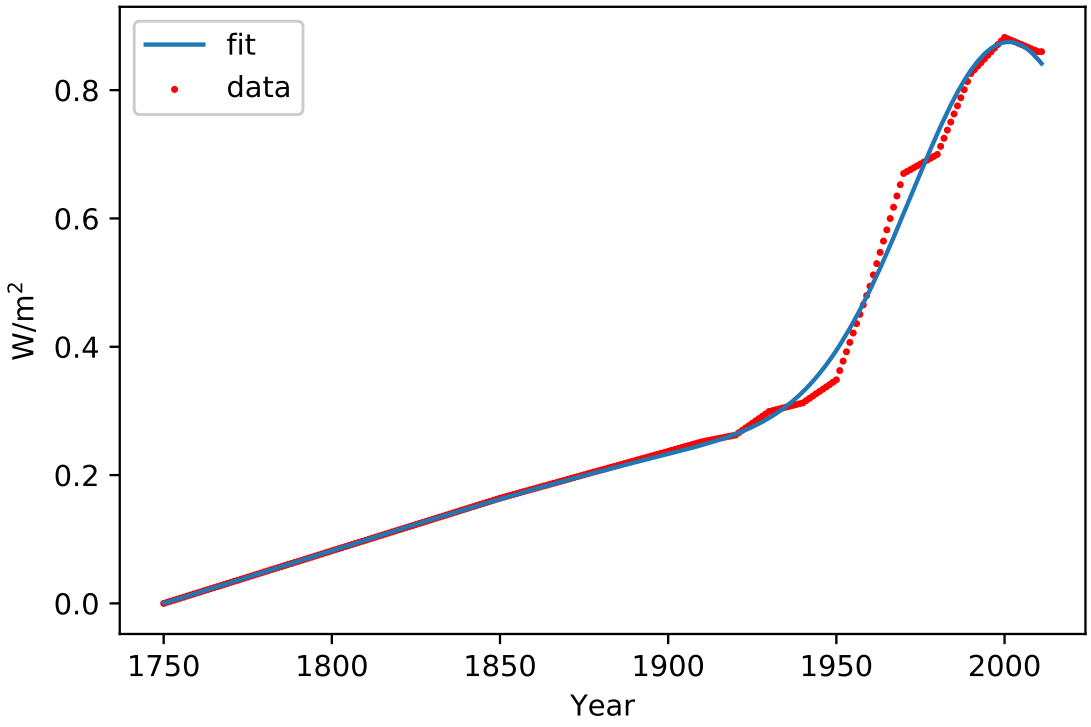

Figure 6.2. Net radiative shielding estimates for anthropogenic aerosols and black carbon on snow, fit with a constant times the deforestation rate plus a Gaussian function.

6.3 Tropospheric ozone forcing

Tropospheric ozone is a short-lived trace gas that is partly emitted into the troposphere and partly produced in situ by precursor gases and sunlight [24]. Ozone is an important contributor to the earth's radiative balance, which is both a major absorber of incoming ultraviolet (UV) in the stratosphere and a significant absorber of earth's emitted infrared radiation. Figure 6.3 shows a fit to the net radiative forcing from tropospheric ozone to estimates from IPCC fifth assessment report [2] . The fitting procedure is the same as for shielding from anthropogenic aerosols and black carbon on snow. The fitting parameters for the gaussian function are listed in table K.2.

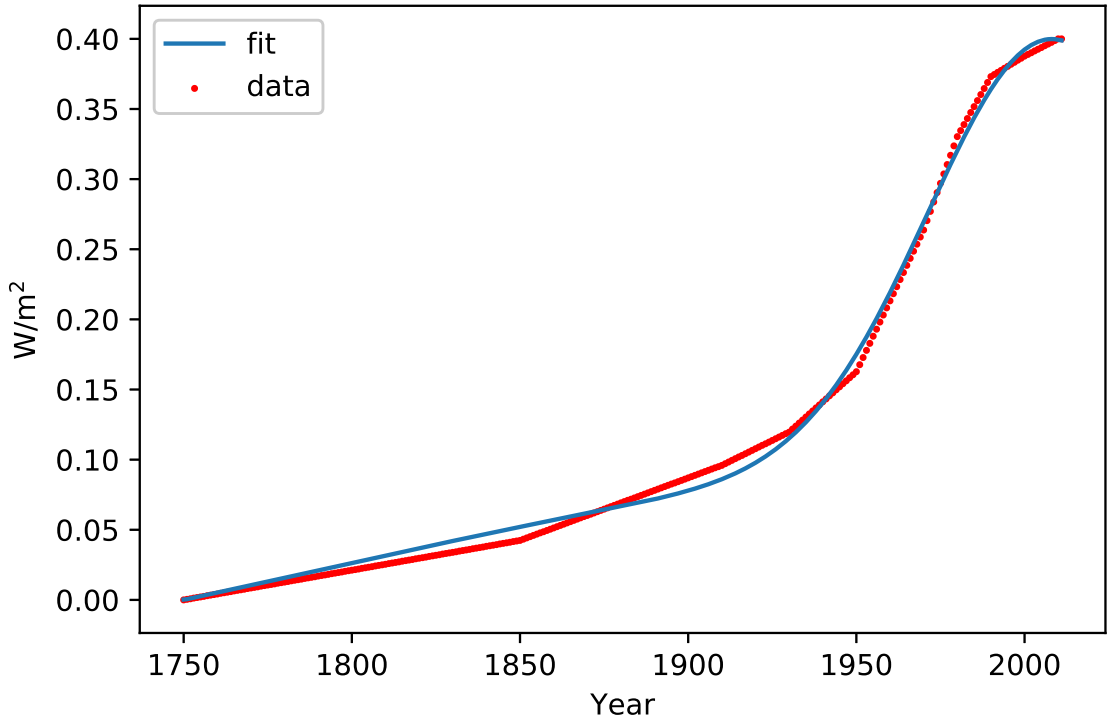

Figure 6.3. Radiative forcing estimates for anthropogenic tropospheric ozone, fit with a constant times the deforestation rate plus a Gaussian function.

6.4 Volcanic shielding

In 1991, the eruption of Mount Pinatubo in the Philippines ejected more than 20 million tons of sulfur dioxide—a gas that interacts with other substances to produce sulfate aerosol—as high as 60 kilometers (37 miles) above the surface, creating particles in the stratosphere. Dispersal around the world caused global temperatures to drop temporarily (1991 through 1993) by a maximum of about 0.5°C [25]. The radiative, chemical, dynamical and climatic consequences accompanying the transient duration of sulphuric acid aerosols in the stratosphere have been discussed in previous IPCC assessments. Peak volcanic radiative shielding in W/m^2 from years -491 to 1992 [26] and from 2008 and 2011.5 [27] were multiplied by the ratio of the integrated (W/m^2)yr from the 1992 Pinatubo eruption to obtain estimates of the (W/m^2)yr [28] for all of the volcanoes. For the recent volcanoes, the Okmak and Kasatochi eruptions combined and assigned to time 2008.6 in Julian years. One eruption in 2009 was assigned to time 2009.4. Four eruptions from Nov 2010 through May 2011 were combined in proportion to estimated sulfur emissions ratios to the Pinatubo eruption.

Figure 6.4 shows the time derivative of the fit to cumulative volcanic radiative shielding shown in figure 6.5, less the time derivative of the slope of cumulative radiative shielding versus time from volcanoes after 1654 and through 1756. The fitting parameters for constant and three logistic functions used to produce figure 6.4 are listed in tables N.1-N.3.

Douglass and Knox proposed that the cooling effect of volcanoes is mostly limited to the time when their aerosols are still in substantive amounts in the atmosphere [28]. Therefore, climate sensitivity λ as 0.85 °K/(W/m^2) estimate may be slightly low due to an assumption that volcanoes have more lasting effects.

6.5 Solar irradiance

The rate at which energy from the sun reaches the top of the earth's atmosphere is called "total solar irradiance". Total solar irradiance (TSI) fluctuates slightly from day to day and week to week. In addition to these rapid, short-term fluctuations, there is an 11-year cycle in TSI measurements related to "sunspots" (parts of the sun's surface that is temporarily cooler

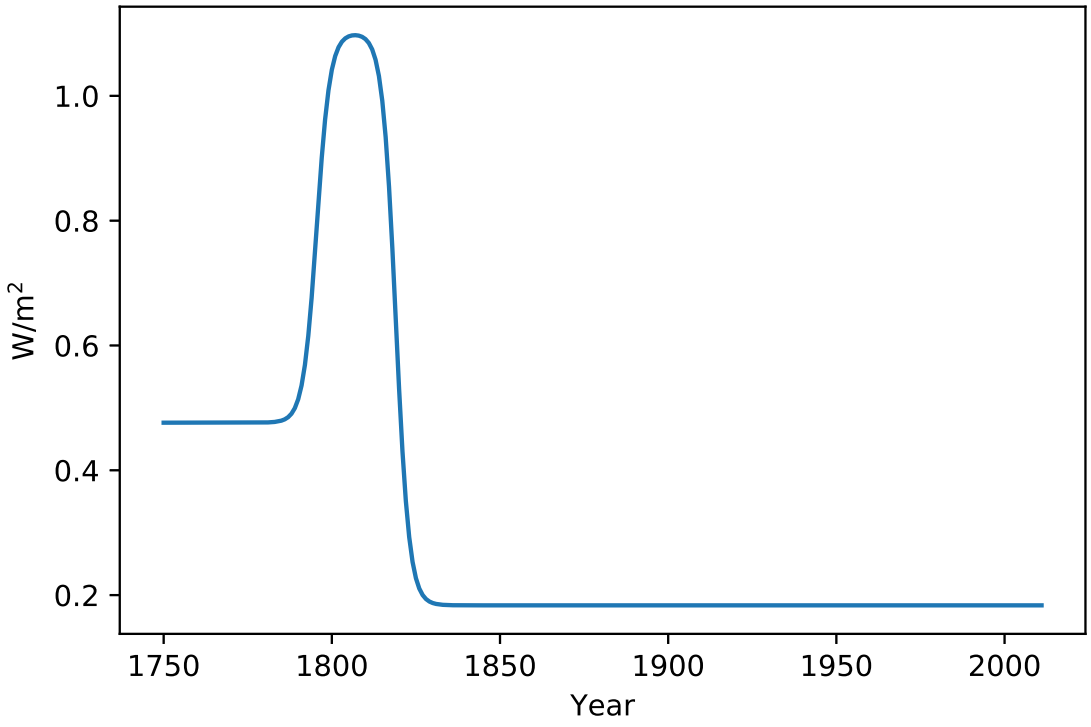

Figure 6.4. Average annual volcanic radiative shielding change from 1654–1756.(The timing of volcanic eruptions after 1756 suggested using 1654–1756 rather than 1650–1749 as a baseline.)

and darker than its neighboring regions, with some of magnetic energy that helps contain the plasma in the darker regions deposited in the solar corona). Estimates of annually averaged solar irradiance are based on direct satellite measurements, solar magnetic activity, and ice core radioisotopes. Kopp, Heuerman, and Lawrence [29] provide daily estimates from direct satellite measurements in W/m^2 converted to normal incidence at one astronomical unit from the sun from March 7, 2003, to about one week before the latest access date. The Spectral and Total Solar Irradiance Reconstruction project has used direct and indirect estimates of solar magnetic activity to extrapolate satellite irradiance measurements annually averaged from 2014 back to 1700 [30, 31, 32] and daily from 2005 back to 1610 [33]. The solar magnetic activity estimates were multiplied here by 0.996128, to be consistent with the average satellite measurements for the data overlaps years of 2004 and 2005.

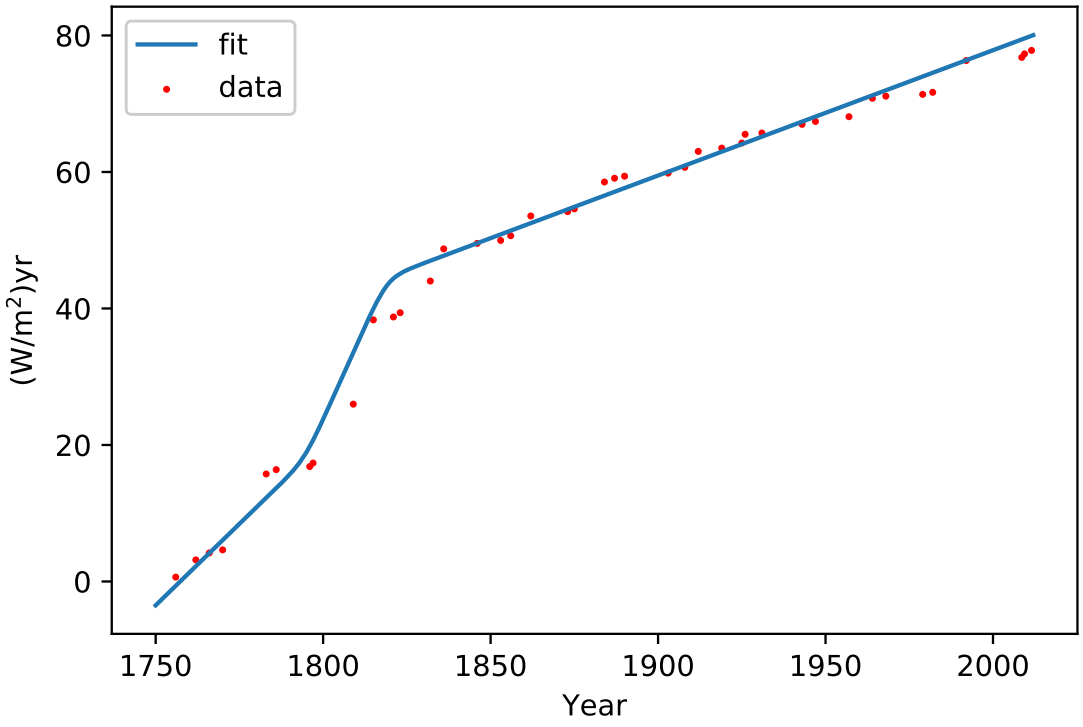

Figure 6.5. Cumulative volcanic forcing (dots) compared to the time integral of the volcanic shielding rate in figure 6.4.

Steinhilber, Beer and Frölich [34] used ice core radioisotope measurements to estimate solar irradiance from 9321.5 years before 1950 through year 2007.5. McCracken et al. [35] identified periodicities in this long time series with periods of 976 and 708 years. Starting from either of these, a year 202.5 to 2007.5 quinquennial data set gave a period of 841.916 years, and a cosine maximum at year 255.824. The cosine fitting formulas have the form of $b_1 cos(2\pi(t-b_2)/b_3)$. Values of the fitting parameters for the cosine terms are listed in tables O.1 and O.2. Values of the fitting parameters for the gaussian functions are listed in tables O.3 and O.4.

Figure 6.6 shows a fit to annual estimates from direct satellite measurements and sunspot data from 1650–2017 with those cosine parameters and a variable amplitude, plus another cosine function with period 257.658 years, from a search starting with the 208 year periodicity also noted by McCracken et al. Figure 6.6 shows the resulting fit to the difference between the 1650–1749 global surface average of $1359.49/4 = 339.873$ W/m^2, along with two Gaussian

corrections. Surface ocean mixed layer thermal inertia damps short period oscillations in the global heat balance model described below, so an approximately 11 year periodicity in solar irradiance is not included here. To indicate how well the fit used corresponds to an 11 year average of the data, that average is also included in figure 6.6, as a jagged line, for 11 year periods from 1650 through 2012.

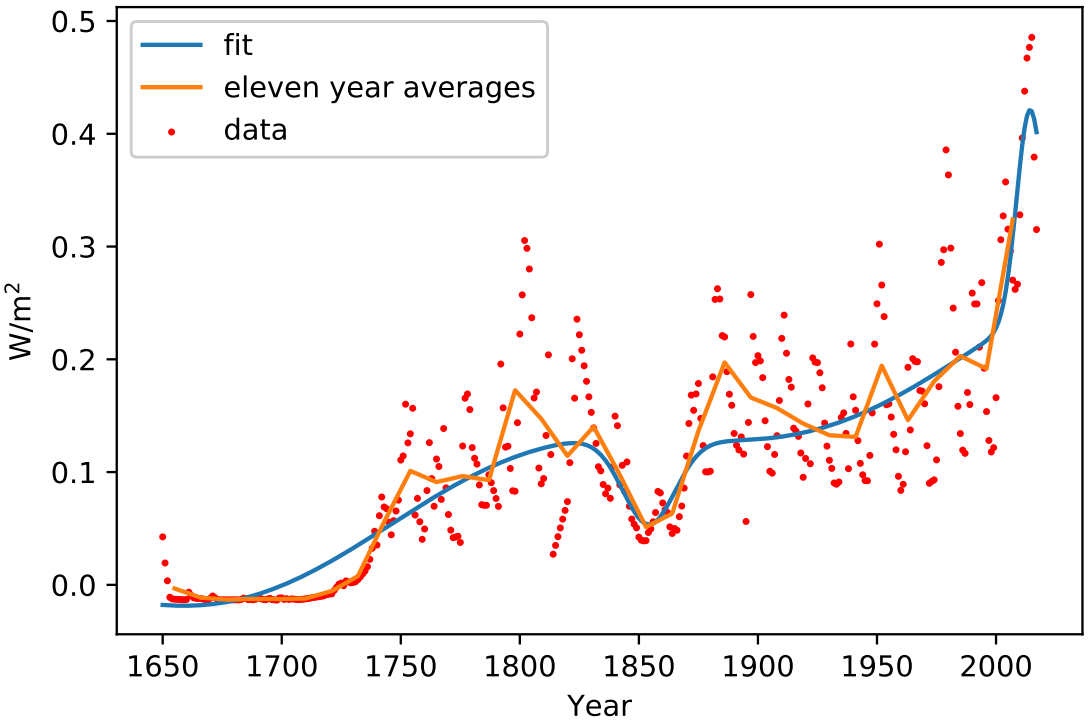

Figure 6.6. One quarter of the normal solar irradiance (dots) less the 1650–1749 average of 1359.49/4=339.873 W/m^2, eleven year averages from 1650–2012 (connected by dashed line segments), and a fit to the dots with the sum of two cosine and two Gaussian functions.

6.6 Total long wavelength radiative forcing

The Earth's climate system constantly adjusts in a way that tends toward maintaining a balance between the energy that reaches the Earth from the sun and the energy that goes from Earth back out to space. That balance is the so-called "radiation budget." The budget

equation is:

$$\frac{\partial E}{\partial t} = R_{in} - R_{out} \tag{6.1}$$

Here R_{in} is the input, and R_{out} is the output. The left-hand-side of this equation is the rate-of-change of global total energy. In this case, the input is net short wavelength solar power, and output is long wavelength emission. On the one hand, deserts, ice, and clouds have high albedos, and a large portion of the sun's energy is reflected back out to space from earth surface. On the other hand, the Earth's surface is heated up by absorbing energy, and at the same time, it emits long-wave radiation back out to space to keep approximately in balance.

Cumulative radiative forcing of carbon dioxide from industry and land use changes are plotted respectively in figure 6.7, in which cumulative radiative forcing of methane and nitrous oxide are plotted as well. It is evident that the fraction of radiative forcing as a result of industrial emitted carbon dioxide has become highest of those plotted. The summation of radiative forcings of other well mixed greenhouse gases except CO_2, CH_4, N_2O and tropospheric ozone and contrails are shown in figure 6.8 as well.

For the case of CO_2, CH_4, N_2O, the linear models which are fitted previously are used to evaluate the radiative forcing. For tropospheric ozone, the historical data from ANNEX II Table AII 1.2 of IPCC fifth Assessment [2] are fitted analytically.

From figure 6.8, the effect of tropospheric ozone and other well mixed greenhouse gases are comparable. However, the contrail effect is small compared with the other forcings. The radiative forcing caused by the "other greenhouse gases" group have the largest initial growth rate of those plotted in figure 6.8.

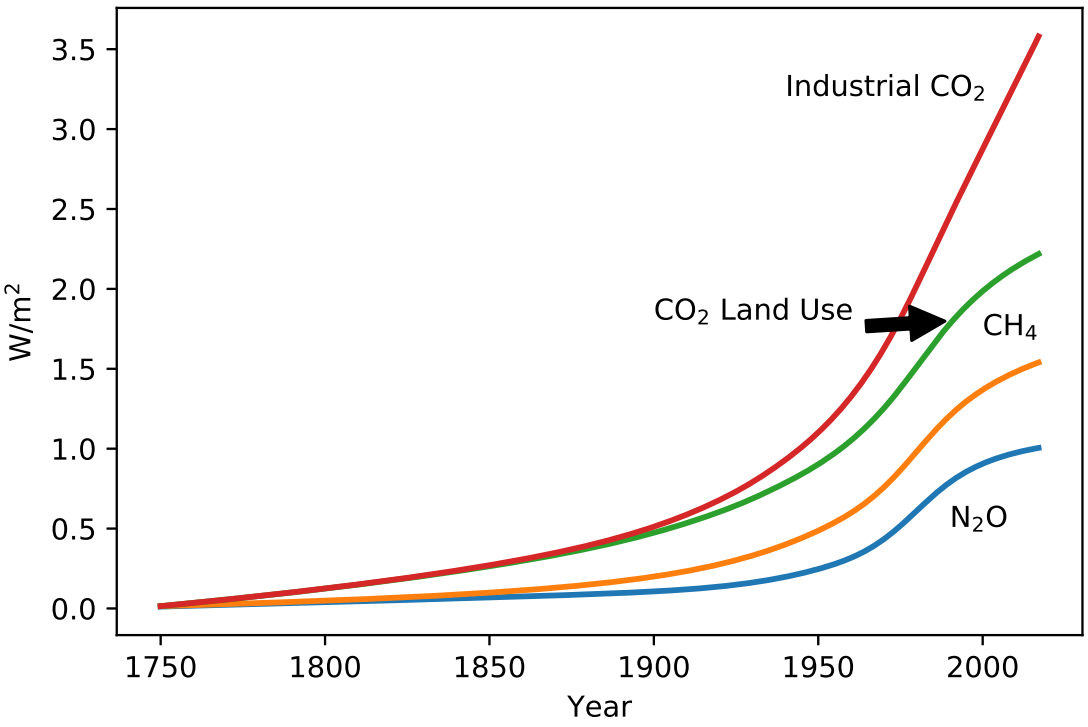

Figure 6.7. Sums of radiative forcing including, from bottom to top, from <N_2O>, <CH_4>, <CO_2> from land use changes, and industrial <CO_2>.

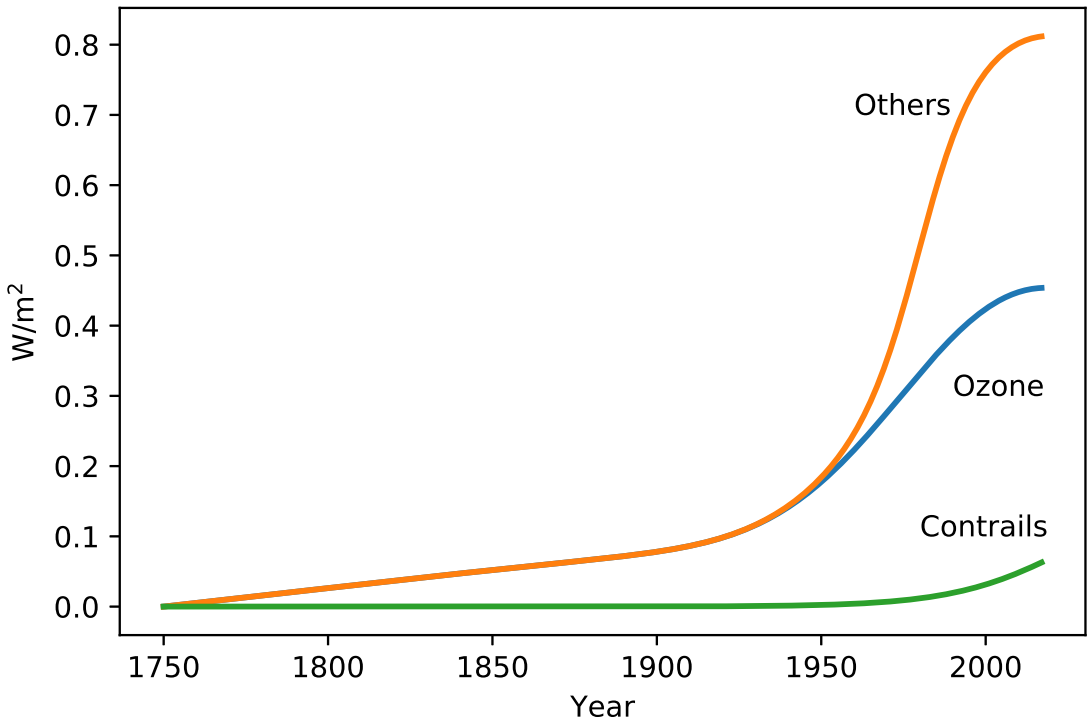

Figure 6.8. Sums of radiative forcing including, from bottom to top, from contrails, tropospheric ozone, "other greenhouse gases".

CHAPTER 7

GLOBAL HEAT BALANCE

In this chapter, the governing equation for the global heat balance is given, along with the solution of the governing equation. Then, a least square fit to temperature starting from 1892 to 2017 is made, and residuals between the data-calibrated reference model and historical temperature data are plotted.

Approximating the heat capacity of the heat absorbing materials as constant in time, climate system of geometrical dimension zero given in equation 6.1 can be described by the energy conservation law after integrating over the total mass (per unit area) of the system

$$c\frac{dT}{dt} = R_{in} - R_{out}$$

The storage term (left) results from the imbalance between net incoming solar radiation, R_{in}, and outgoing emission, R_{out} [36].

7.1 Equation derivation

The starting point for derivation of the global heat balance equation used for the present analysis is a nonlinear equation for evolution of the global average temperature T in degrees Kelvin [1].

$$c_3\frac{d\tau}{dt} = c_{18}\left[1 - c_{20} + c_{22}(\frac{T}{T_0})^2\right] - c_{24}\left(\frac{T}{T_0}\right)^4\left[c_{21} - c_{23}\left(\frac{T}{T_0}\right)^2\right] + F \tag{7.1}$$

where

$$\tau = T - T_0 \tag{7.2}$$

and

$$F = g_0 + g_1 + g_2 + g_3 + g_4 + g_5 + g_6 + c_0 g_7 + g_8 + g_9 \tag{7.3}$$

is the sum respectively of the radiative forcing described above from tropospheric ozone, <CO_2>, <CH_4>, <N_2O>, "other well mixed greenhouse gases", contrails, and incoming solar irradiance, on radiative shielding from land use albedo changes, anthropogenic aerosols and stratospheric ozone less radiative forcing from black carbon on snow, volcanoes. F is defined in AR5, as in previous IPCC assessments, as the change in net downward flux (shortwave & longwave) at the tropopause after allowing for stratospheric temperatures to readjust to radiative equilibrium, while holding other state variables such as tropospheric temperatures, water vapour and cloud cover fixed at the unperturbed values [2]. F is expressed in watts per square meter (Wm^{-2}). An adjustable parameter c_0 is included to multiply the anthropogenic aerosol dominated shielding to account for possible differences concerning this effect between the present global heat balance model and global circulation models for which the radiative forcing estimates described above were designed.

Here $c_{24} = \sigma T_0^4 = 383.647$ W/m^2, with σ the Stefan-Boltzman constant, is the black body radiative loss rate in W/m^2 at the 1650–1749 average $T_0 = 286.681$ of the global average temperature based on figure 9.8 on page 768 of the 2013 IPCC working group I report [37]. The time averaged total solar irradiance averaged over the surface area of the earth during the same time period is $c_{18} = 1359.49/4 = 339.873$ in W/m^2 based on the data described in section 6.5 of this thesis. F is the sum of the positive long wavelength radiative forcing and negative short wavelength radiative forcing describe above. This equation is identical to that used by Singer and Matchett [1], except for use of the notation c_3 for the constant that multiplies dT/dt and is proportional to the thermal inertia of a model surface ocean mixed layer.

Global average temperatures from thermometer measurements as used here are expressed as differences from a 1650–1749 average based "multiproxy" estimates [38]. The thermometer measurement average estimates were reported as differences from a 1951–1980 average [39, 40] , while the"multiproxy" estimates where reported as differences from a 1961–1990 average [38]. A correction of 0.101333°K was subtracted from the reported thermometer av-

erage data to account for the increase thermometer average from the 1951–1980 to 1961–1990 avreages.

The steady state version of the above heat balance equation is cubic in $(T/T_0)^2$, because it is based on an equation originally developed for comparison of planetary atmospheres with and without enough radiative forcing to allow for a low and high temperature solution to the cubic equation [36]. For the present purposes, it suffices to use an approximation that is linear in τ/T_0, assuming $\tau/T_0 \ll 1$. This is adequate for calibration of the global heat balance against historical data and for extrapolations that account for human responses to climate change that keep global average temperature away from the drastic increases that would require including terms of order $(\tau/T_0)^2$ in the analysis. Then, the equilibrium state solution can be derived by letting T=T_0, and $F = 0$ in equation 8.1,

$$0 = c_{18}(1 - c_{20} + c_{22}) - c_{24}\epsilon_0 \tag{7.4}$$

with emissivity in the absence of industrial era anthropogenic radiative forcing of

$$\epsilon_0 = c_{21} - c_{23} \tag{7.5}$$

Dropping products of the small terms such as $\mathrm{O}\big((\frac{\tau}{T_0})^2\big)$, and $\frac{\tau}{T_0}F$, and using equation 7.5, the linearized equation is:

$$c_3\frac{d\tau}{dt} = 2c_{18}c_{22}\frac{\tau}{T_0} - 4c_{24}\frac{\tau}{T_0}(c_{21} - c_{23}) + 2c_{23}c_{24}\frac{\tau}{T_0} + F \tag{7.6}$$

Equation 7.6 is same as the linearised one-box model given by Rypdal [41]. The 1650–1749 reference period albedo $c_{20} - c_{22} = 0.299557$ is estimated subtracting 0.150602/(1359.49/4) from the value of 0.3 measured as about constant from 2000 through 2012 [42]. Here 0.150602 W/m^2 is the increase in albedo due to land use changes from 1750 to 2016 as described above, and (1359.49/4) W/m^2 is the global surface average reference solar irradiance. While this correction is presumably smaller than the albedo measurement uncertainty, it is included to make the albedo used in the calculation the same as the reported measured value. The 1650–1749 reference period emissivity is then estimated as $\epsilon_0 = c_{18}(1 - c_{20} + c_{22})/c_{24} = 0.620523$.

Dropping the above-mentioned cancelling lowest order terms in an expansion in τ/T_0 and keeping only the next order terms in that expansion gives

$$c_3 d\tau/dt = F - c_2\tau/T_0 \tag{7.7}$$

Here

$$c_2 = 4\epsilon_0 c_{24} - 2c_{23}c_{24} - 2c_{18}c_{22} \tag{7.8}$$

Here g_6, g_7, and g_8 are equal to -1 times the shielding functions plotted above in figures 6.1, 6.2, and 6.4. By calibration of the adjustable parameters in the present global heat balance model against the evolution of global average temperature alone, it is only possible even in principle to make an estimates of c_0, c_2 and c_3, but not separately of the ice albedo effect constant c_{22} and the temperature effect on atmospheric water c_{23} in the equation for c_2. However, Mauritsen et al. [43] have used a global circulation model to estimate the relative importance of these two effects. For a doubling of the $<CO_2>$ radiative forcing, they found that the ice albedo effect accounted for only 0.17 °C global average temperature increase out of a total of 1.763 °C for the temperature effect on atmospheric water.

7.2 Heat balance solution formulas

The solution to equation 7.7 can be written as

$$\tau = \sum_{n=0}^{10} \tau_n \tag{7.9}$$

Here τ_{10} solves $c_3 d\tau/dt = -c_2\tau/T_0$ with an initial condition for τ when $t = t_0$. $\tau_{10} = \tau_{t_0} e^{-(t-t_0)/t_{inertia}}$. Here, t is set to start from year 1892 to year 2017 and t_0 is the baseline year at 1750. Generally, $t_{inertia}$ is of order of several decades. Therefore, the effect of initial condition on τ is negligible when $t - t_0$ is very large compared to $t_{inertia}$. Here, it is more convenient to let the initial condition for τ be 0, which is equivalent to setting $\tau_{10} = 0$.

The other τ_n solve, with $\tau_n = 0$ when $t = t_0$, solve

$$c_3 d\tau/dt = -c_2\tau/T_0 + g_n \tag{7.10}$$

for $n = 0 \ldots 5{,}9$ and

$$c_3 d\tau/dt = -c_2\tau/T_0 - g_n \tag{7.11}$$

for $n = 6, 7, 8$. Here a given g_n is the sum of one or more terms, shown as:

$$g_n = \sum_{m=1}^{m=M_n} g_{nm} \tag{7.12}$$

where M_n is different for each n. Therefore, the solution for each n can be written as the sum of solutions to $c_3 d\tau/dt = -c_2\tau/T_0 + g_{nm}$ for $n = 0, \ldots 5{,}9$ or of $c_3 d\tau/dt = -c_2\tau/T_0 - g_{nm}$ for $n = 6, 7, 8$.

It is convenient for each such case to define a new independent variable

$$x_{nm} = (t - t_{nm})/w_{nm} \tag{7.13}$$

with t_{nm} being "pivot times" for the contributions to driving terms and w_{nm} being characteristics timescales for variation of those terms. Then, letting

$$s_{nm} = (c_2/T_0) w_{nm}/c_3 \tag{7.14}$$

the solutions are, for $n < 10$,

$$I_n = e^{-s_{nm}x} \int_{x_{nm0}}^{x} e^{s_{nm}x} f_{nm} dx \tag{7.15}$$

where

$$f_{nm} = g_{nm} w_{nm}/c_3 \tag{7.16}$$

for $n = 0 \ldots 9$. The thirty functions f_{mn} are listed in Table P.4 with x in each function definition taking on the value x_{nm} defined by the constants t_{nm} and w_{nm} in that table.

Here x_{nm0} is the value of x_{nm} when $t = t_0 = 1750$. There are ten different types of function forms f_{nm}. For convenience, the analytical form of the ten kinds of solutions I_{nm} are provided in appendix P.

7.3 Least squares fits to temperatures from 1892-2017

The solid curve in figure 7.1 is a least squares fit to global average temperatures from 1892–2017. Starting the data for the least squares fitting procedure to obtain the curve in figure 7.1 was done with year 1892 because the integration from 1750 to 1892 gives a temperature increment then over the 1650–1749 average that is very close to an 11 year average centered at 1891. The temperature data start from a negative number is due to the negative volcanic forcing at early nineteenth century. What is primarily of interest here is extrapolation beyond the historical data times, and omitting the sparser earlier individual temperature measurements concentrates the historical data fit on times closer the time where extrapolations will start. The dashed curve includes the dominant amplitude in a discrete Fourier cosine transform of the differences between the data and the fit. The dashed curve in figure 7.1 is meant to capture the dominant intrinsic variation. That there are significant such intrinsic variations not reflecting changes in radiative forcing has been suggested to correlate with North Atlantic and Tropical Pacific Ocean temperature oscillations [44]. The parameters adjusted to get the solid curve in figure 7.1 are the climate sensitivity λ, the surface mixed ocean layer thermal inertia c_3, and the multiplier c_0 of the aerosol-dominated radiative shielding.

If a new equilibrium value of τ is attained with the forcing F, we have

$$\lambda = \frac{\tau}{F}$$

which makes it natural to identify λ as the climate sensitivity in equilibrium [41]. Climate sensitivity is sometimes defined as how much the average global surface temperature will increase if there is a doubling of greenhouse gases (expressed as carbon dioxide equivalents) in the air, once the planet has had a chance to settle into a new equilibrium after the increase

occurs [2]. In IPCC report, the radiative forcing are scaled by doubling CO_2 concentration which is 3.7 Wm^{-2} [45] combined with an equilibrium climate sensitivity of 3.0°C, midway between an estimated range of 1.5 °C to 4.5 °C. That corresponds to a value of λ of 0.81 °K/(W/m^2), midway between 0.41 and 1.22 °K/(W/m^2).

The parameters in the present work correspond to an climate sensitivity λ of 0.84998 °K/(W/m^2), a mixed ocean layer volume equal to the ocean surface area times 761.519 meters, and multiplying the early aerosol dominated direct radiative shielding estimate by a factor of 1.5899 to account for overall aerosol-radiation interaction and other differences between a full radiative transport calculation and the present model. These and other relevant parameters are summarized in Table P.2. Here, it is assumed that the oceans only cover a fraction 0.70 of the earth's surface [46].

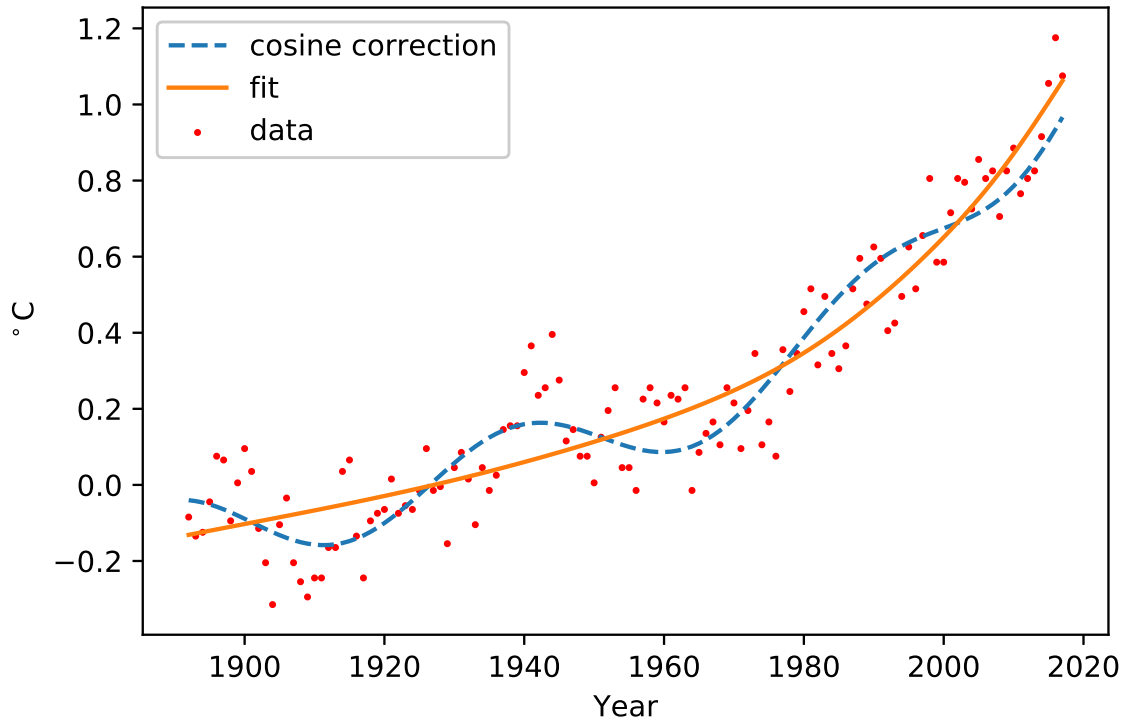

Figure 7.1. Data and reference model solution for evolution of global average temperature without (solid) and with corrections for intrinsic variations with one (dashed curve) cosine correction effects.

L.Resplandy et al. propose that the ocean gained $1.33 \pm 0.20 * 10^{22}$ joules of heat per year between 1991 and 2016, equivalent to a planetary energy imbalance of 0.83 ± 0.11 W/m^2 of Earth's surface [47]. They suggest that ocean warming is at high end of previous estimates from IPCC report. An upward revision of the ocean heat gain would push up the lower bound of the equilibrium climate sensitivity from 1.5°K back to 2.0°K (stronger warming expected for given emissions). Thus, they estimate the new lower bound of equilibrium climate sensitivity λ is 0.5398°K/(W/m^2). Therefore, our estimates of λ fall within the range of their estimates, which also implies that ocean absorbs more energy than previous findings.

There are three primary feedback effects—clouds, sea ice and water vapor. These, combined with other feedback effects, produce the greatest uncertainties in predicting the planet's future climate. Clouds can have either a positive or negative feedback effect, depending on their altitude and the size of their components. Therefore, there is still much uncertainty in what the climate sensitivity is.

Figure 7.2 shows the evolution of radiative forcing used to calculate the result shown in figure 7.1. Starting the data for the least squares fitting procedure to obtain the curve in figure 7.1 was done with year 1892 because the integration from 1750 to 1892 gives a temperature increment then over the 1650–1749 average that is very close to an 11 year average centered at 1891. The figure shows that from 1750–1850, there is a region of negative radiative forcing with particular strong average volcanic shielding in for about two decades near the beginning at the nineteenth century. Then after 1850, the radiative forcing increased. As noted above, the procedure used here produces a large negative volcanic forcing in the early nineteenth century and likely also over estimates the persis of this effect. Starting the model calibration in 1892 showed largely avoid distortions due to the procedure used here for estimating volcanic radiative shielding.

Figure 7.3 shows approximations to the residuals between the data and solid curve shown in figure 7.1, using one cosine function for the dashed curve and five cosine functions for the dotted curve. For the purpose of a reference case model, including the one cosine function is sufficient to identify a presumed oscillation. The parameters of this one cosine function are listed in table P.3. The level of extrapolation of such oscillations without a clearer

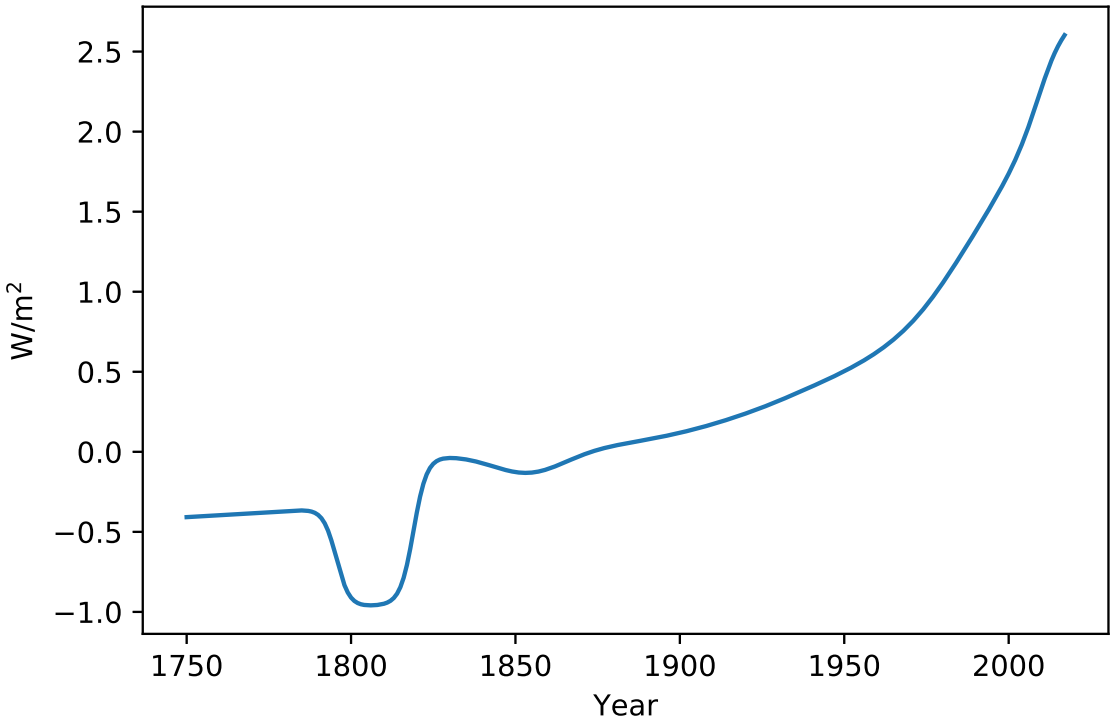

Figure 7.2. Total radiative forcing for the reference model.

understanding of the extent to which their periods and phases are likely to be stable suggests not including more cosine corrections in a reference model. The one cosine correction that is included is meant just to be a reminder of how small the internal variations have been in the past compared to the results from extrapolating radiative forcings into the future as described below. The additional cosine corrections are included in the dotted curve in figure 7.3 as a starting point for possible tests for randomness in the remaining residuals in a quest for a probability distribution for the model parameters.

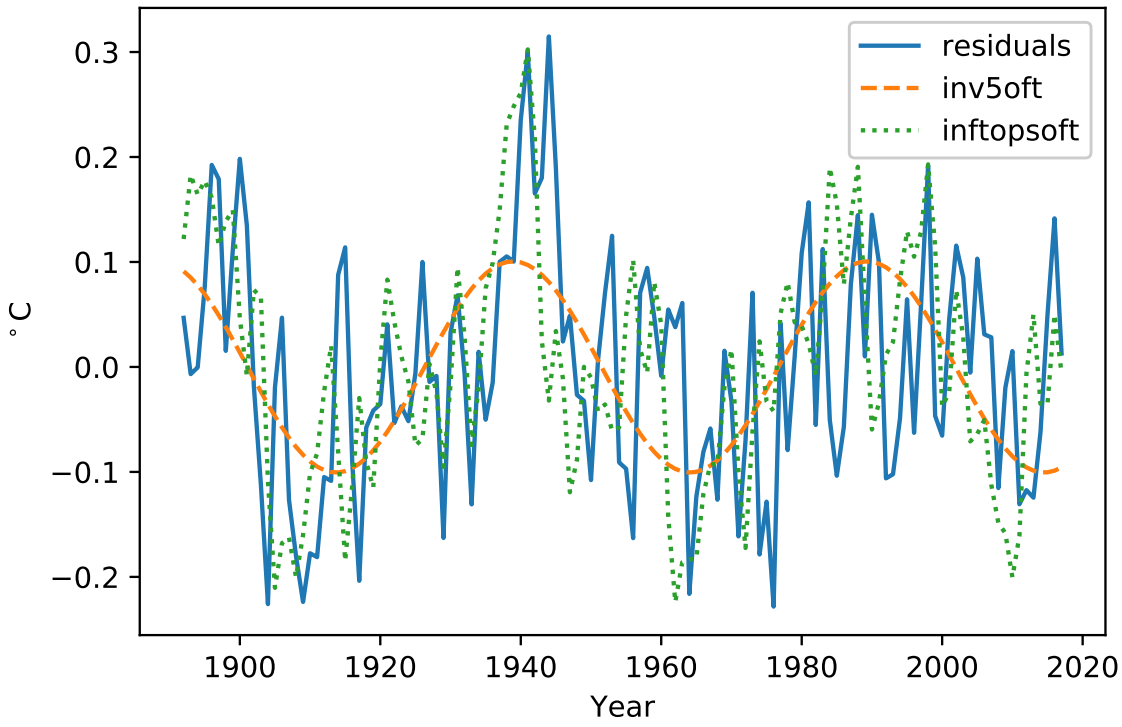

Figure 7.3. Residuals between the data and solid curve in figure 7.1 (jagged curve) and one (dashed curve) and five (dotted curve) summed cosine functions.

CHAPTER 8

EXTRAPOLATIONS

While the analysis described above is suitable for calibrating a priori uncertain parameters in the heat balance equation against time series data, it is not adequate for long-term extrapolation of the radiative forcing from $<CO_2>$, $<CH_4>$, and $<N_2O>$. For each of these, nonlinear dependences of radiative forcing on atmospheric concentration are used in the temporal extrapolations described here. Also, for $<CO_2>$ and $<N_2O>$, the analytic formulas described above for atmospheric concentration as a function of the history of anthropogenic emissions are inadequate for extrapolations involving very substantial increases in atmospheric concentration, so numerical integration of atmospheric balance equations is used below instead. Since numerical integration is used for extrapolating $<N_2O>$, it is also convenient to use accurate numerical extrapolation for $<CH_4>$ instead of an analytic approximation.

8.1 CO_2 extrapolation

As noted above, the fraction of emitted CO_2 that is rapidly removed from the atmosphere is expected to decrease as the CO_2 concentration in the surface ocean mixed layer increases. The extrapolations here rely on simpler version [1] of global atmospheric carbon balance model described by Singer, Milligan, and Rethinaraj [48]. That simpler model approximated the results of a four chamber global analysis by including nonlinear terms to account for how surface ocean CO_2 concentration and temperature affect the global carbon balance. In that analysis, the temperature effect was substantially smaller than the CO_2 saturation effect. That observation is consistent with present analysis being able only to estimate the parameter controlling the CO_2 saturation effect in the following equation, which leaves out

the small temperature effect from the Singer, Milligan, and Rethinaraj model [48].

$$\frac{dc_a}{dt} = \left(c_8 + (1 - c_8) \frac{c_a - c_5}{c_a + c_6 c_5} \right) E_c - \frac{c_a - c_5}{c_7} \tag{8.1}$$

Here c_a is the atmospheric carbon content in Ttonne and E_c is the rate of anthropogenic carbon emissions in Ttonne/yr. As in Singer and Matchett [1], $c_5 = 0.5964$ TtonneC, $c_6 = 0.5$, and $c_7 = 1350$ yr. The value $c_8 = 0.372409$ results from a least squares fit to atmospheric CO_2 concentrations from 1950–2017, with the result shown in figure 8.1.

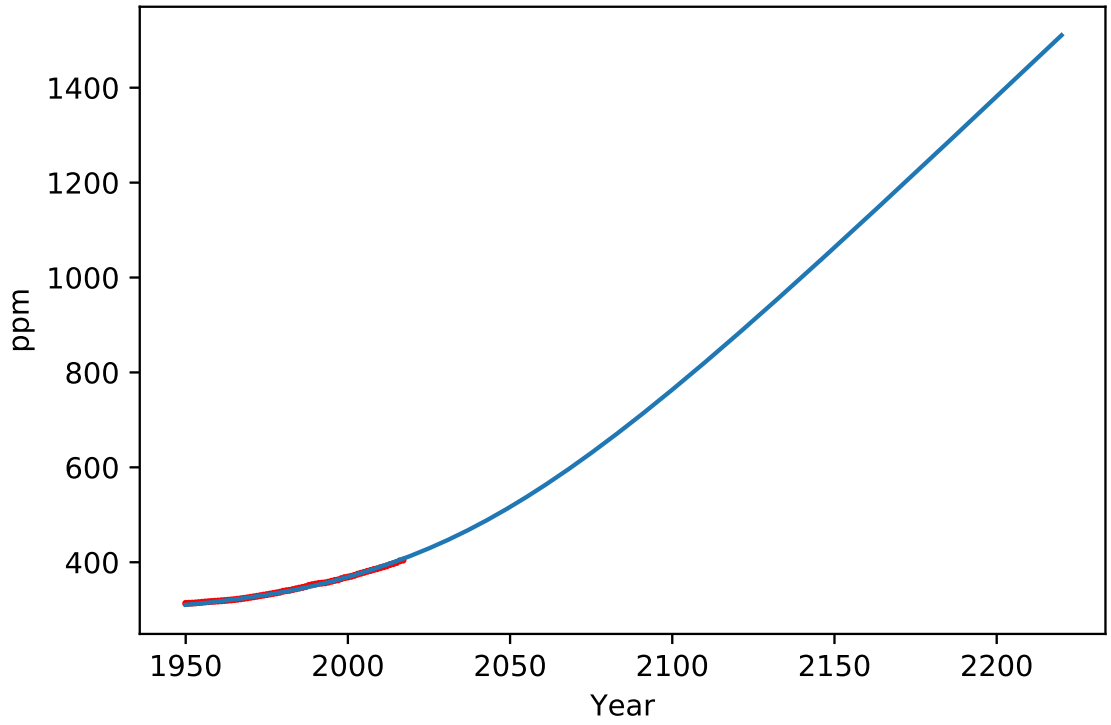

Figure 8.1. <CO_2> data fit and extrapolation with surface ocean mixed layer saturation effect.

8.2 Extrapolated radiative forcing

To estimate the radiative forcing for extrapolated values of <CO_2>, it is important to use the nonlinear relation between forcing and CO_2 plotted above in figure 5.13. Results for

linear and nonlinear formula are shown in as the dotted and solid curve in figure 8.2. As illustrated in that figure, the linear approximation suffices for years through 2017, but not when <CO_2> substantially exceeds 400 ppm. Thus, it is more accurate to use non-linear equation from Table 4.1 to calculate the radiative forcing of CO_2.

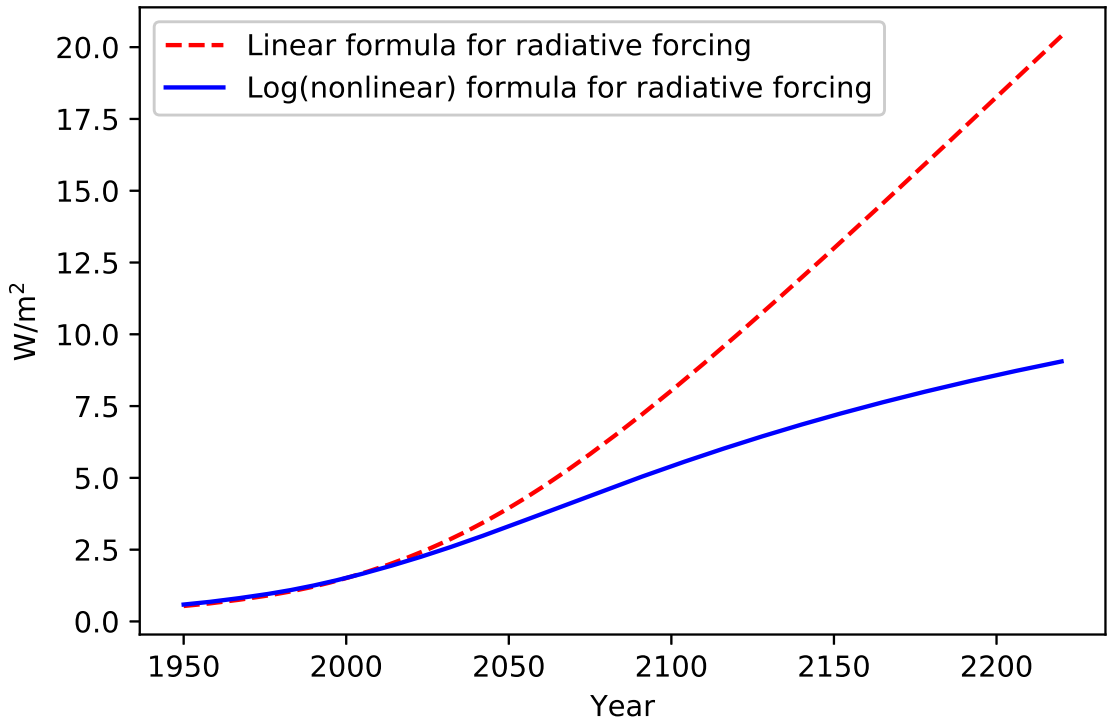

Figure 8.2. Extrapolated radiative forcing from <CO_2> with the formula 5.35ln(<CO_2>/278) (solid curve) and a linear formula for the dependence of radiative forcing on atmospheric carbon dioxide concentration (dashed curve).

The numerically integrated contribution of radiative forcing to global warming from the extrapolated <CO_2> shown above is plotted in figure 8.3. While the increase in <CO_2> becomes approximately linear with time in the second half of the twenty-second century, the nonlinear dependence of radiative forcing from <CO_2> makes the contribution of <CO_2> to global warming eventually increase less than linearly with time. It is the industrial contribution to CO_2 emissions that primarily produce the sizeable temperature increase in the twenty-second century shown below in figure 8.7. It should be kept in mind that this is merely an extrapolation of historical trends, not a prediction. While global coal resources

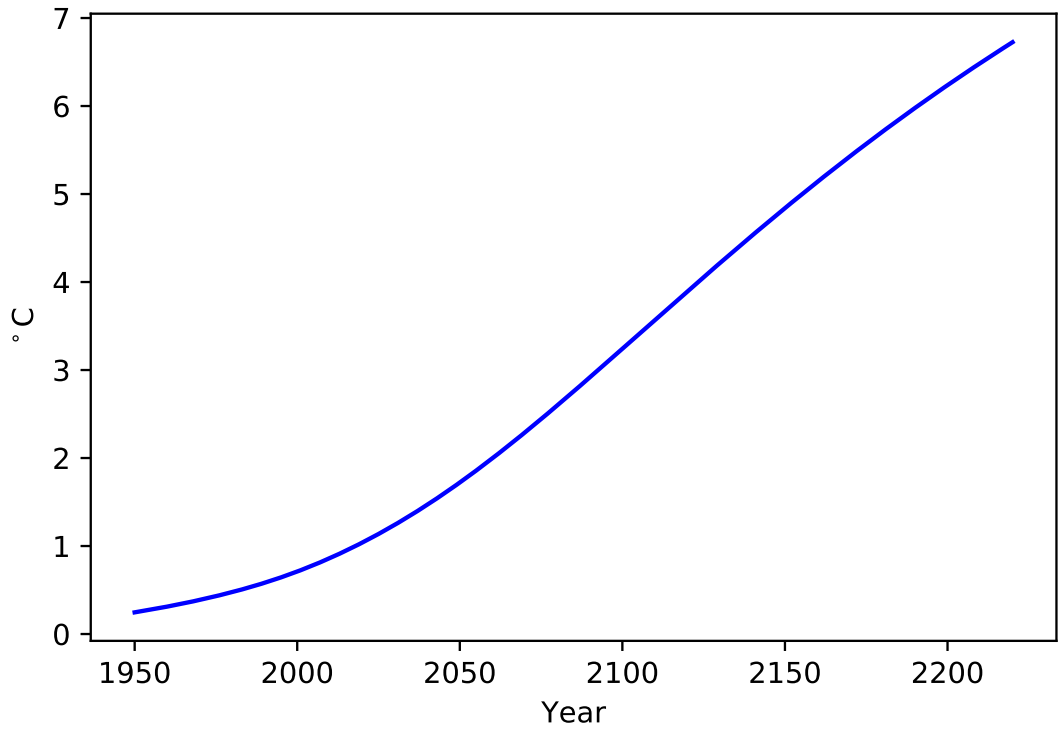

Figure 8.3. Historical (from 1950) and extrapolated contribution from anthropogenic increases in $<CO_2>$ to the industrial era increase of global average temperature.

are sufficient to allow emissions of over 18 GtonneC/yr to continue into the twenty-third century, depletion of fluid fossil fuel resources and evolution of non-fossil energy supply technology might well lead to an eventual reduction in anthropogenic emissions of CO_2 into the atmosphere even without additional negative feedback on anthropogenic emissions due to effects of higher $<CO_2>$ values.

Figure 8.5 compares extrapolated radiative forcing from $<CH_4>$ to that from $<N_2O>$ (dashed curve) for the concentration evolutions shown in figure 8.4. To produce the results in figure 8.5, the above atmospheric balance equations were integrated numerically, and the above nonlinear functions for radiative forcing as a function of atmospheric concentrations were used.

Because nitrous oxide has more radiative forcing per ppb than methane, its longer atmospheric lifetime eventually leads to a larger radiative forcing, as shown in figure 8.5.

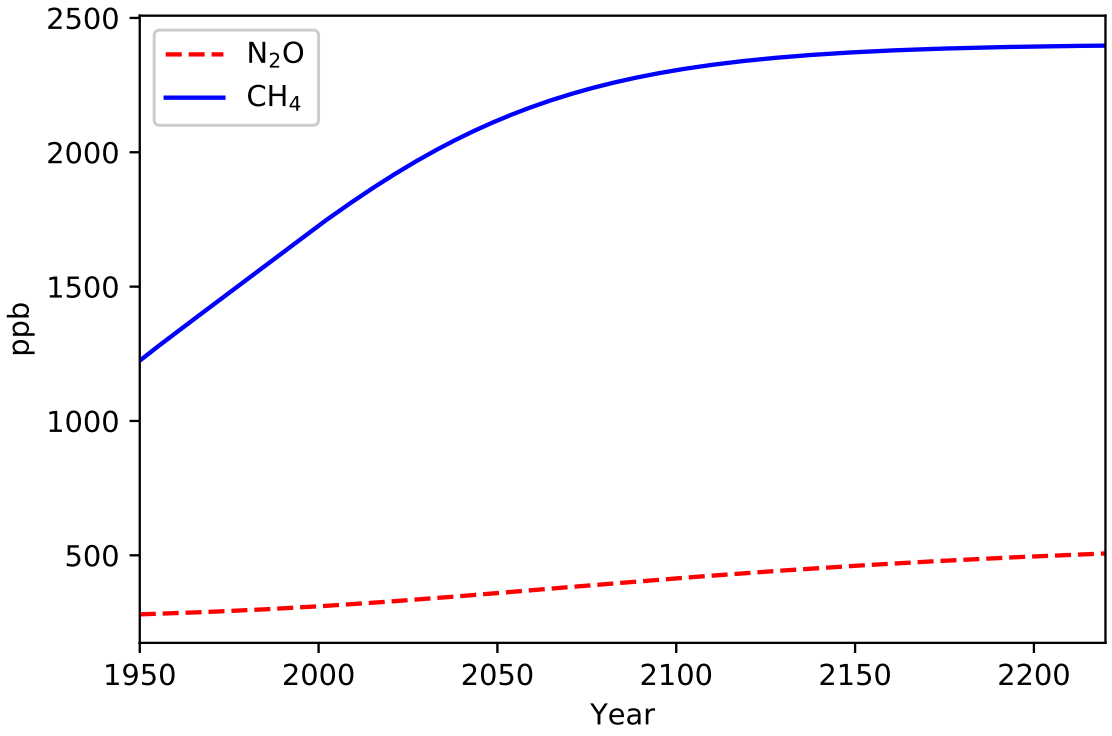

Figure 8.4. Historical (from 1950) and extrapolated <CH_4> and <N_2O> values.

The combined numerically integrated extrapolated effect of <CH_4> and <N_2O> on global average temperature increase is shown in figure 8.6.

8.3 Extrapolated temperature without anthropogenic stratospheric aerosols

Since the global heat balance is linear in the dependent variable τ, the numerically integrated contributions from <CO_2> , <CH_4> , and <N_2O> can be added to results from analytically integrated formulas for other radiative forcing and shielding effects. Figure 8.7 compares the result to historical data from 1950 and extrapolates through 2220. The single sinusoidal intrinsic variation is included to illustrate that such variations are historically small compared to the effect of extrapolated anthropogenic changes in radiative forcing. Figure 8.8 shows that the total radiative forcing for the reference model is over 10 W/m^2 at the end of 2220.

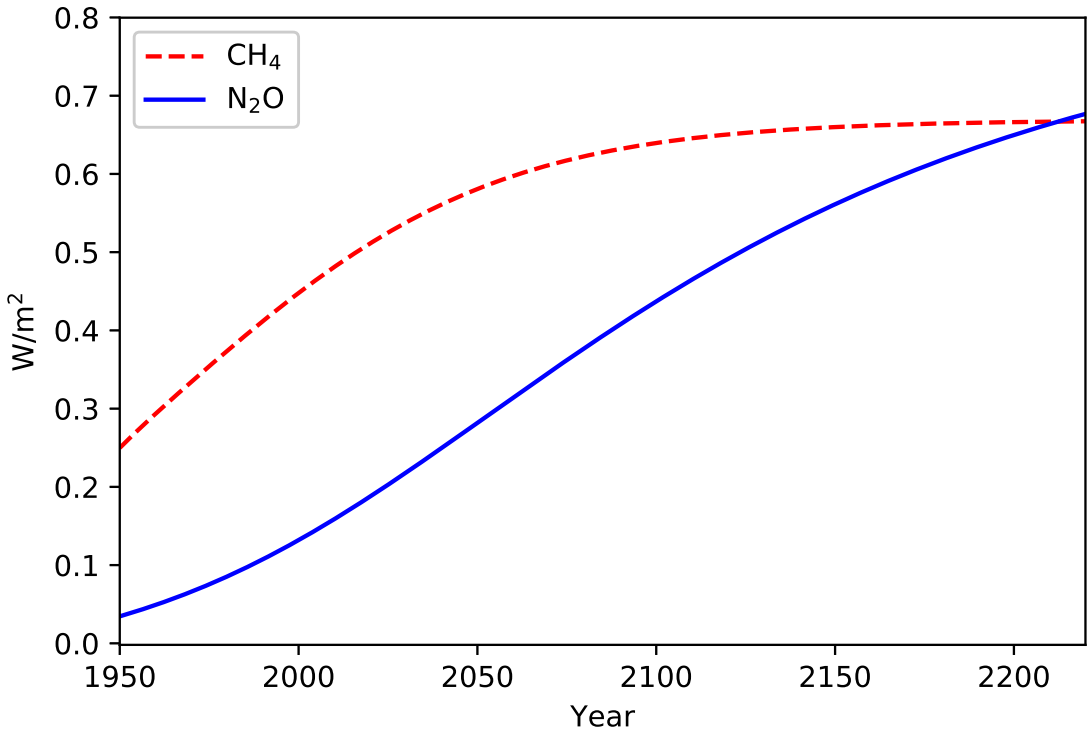

Figure 8.5. Historical (from 1950) and extrapolated extrapolated contribution from anthropogenic increases in <CH_4> and <N_2O> to radiative forcing.

Comparing figure 8.8 to figure 8.2, overall radiative forcing increases are dominated by CO_2, but the net effect of other radiative forcings also becomes substantial. It is evident that CO_2 contributes most to the increment of the total radiative forcing.

8.4 Solar radiation management

The solid curve in figure 8.9 shows the evolution of τ if in year $t_1 = 2020$ enough sulfur is deliberately injected into the stratosphere to reduce the equilibrium temperature to be equal to its 1650–1749 average. This equilibrium temperature would be the optimum countries that lie wholly between forty degrees north and south latitude if their economically optimum temperature were the same in that pre-industrial era when they had predominantly agrarian

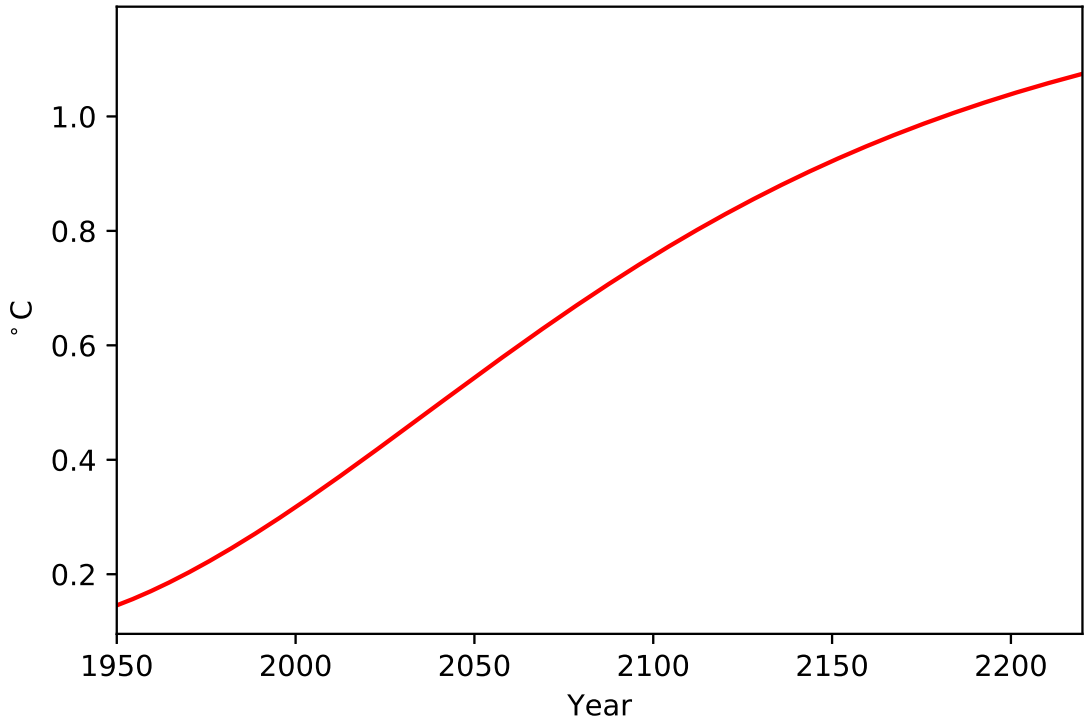

Figure 8.6. Historical (from 1950) and extrapolated combined contribution from anthropogenic increases in $<CH_4>$ and $<N_2O>$ to the industrial era increase of global average temperature.

economies. Under this assumption, the equation for τ starting in 2020 is simply

$$\tau = \tau_1 e^{-(t-t_1)/t_{\text{inertial}}} \tag{8.2}$$

where $t_{\text{inertial}} = \lambda c_3$ is the surface ocean mixed layer thermal inertia timescale of about 41.4776 years and τ_1 the value of τ at $t_1 = 2020$.

The dashed curve in figure 8.9 shows the evolution of τ with $t_1 = 2020$ and $\tau = (\tau_1/2) + (\tau_1/2)e^{-(t-t_1)/t_{inertial}}$. This result represents a hypothetical compromise between countries with an lower economically optimum τ and more temperate region countries with a higher economically optimum τ. In exchange, the more temperate region countries might help pay for limiting the global increase in anthropogenic carbon emissions. An example might keep atmospheric carbon emissions frozen at their 2020 level. The approach would keep $<CO_2>$

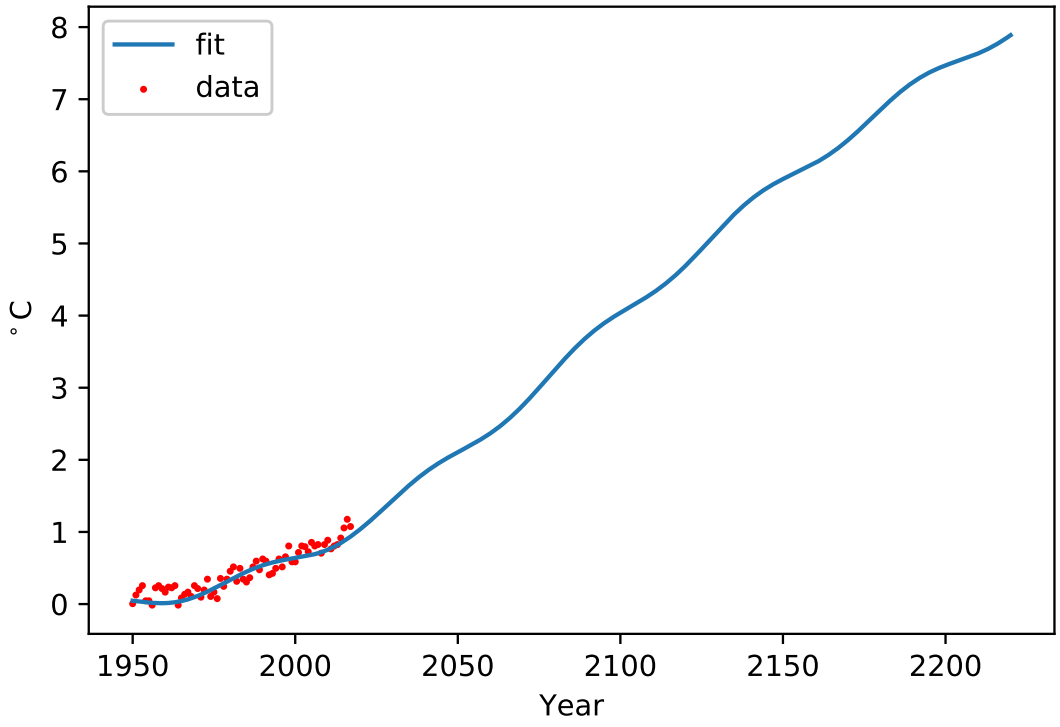

Figure 8.7. Historical (from 1950) and extrapolated change in industrial era global average, compared to historical data from 1950–2017.

from reaching 1500 ppm by 2020, a level which a double blind experiment has shown to have statistically significant effect on a particular test of performance on a cognitive test [49]. That approach would also produce less increase in surface mixed ocean layer acidity, which can be quantified using a model that Singer, Rethinaraj, and Milligan [48] adapted from Eliseev and Mokhov [50]. While such options are not analyzed here, the model described here is well suited to this type of study.

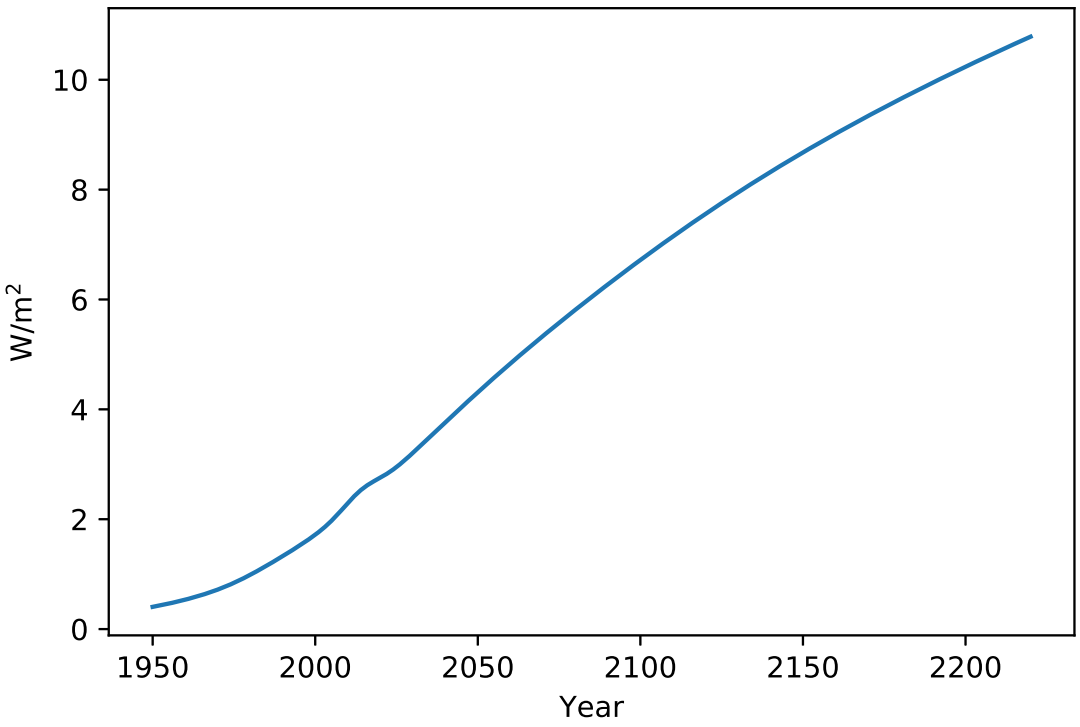

Figure 8.8. Extrapolation of total radiative forcing for the reference model from 1950–2220

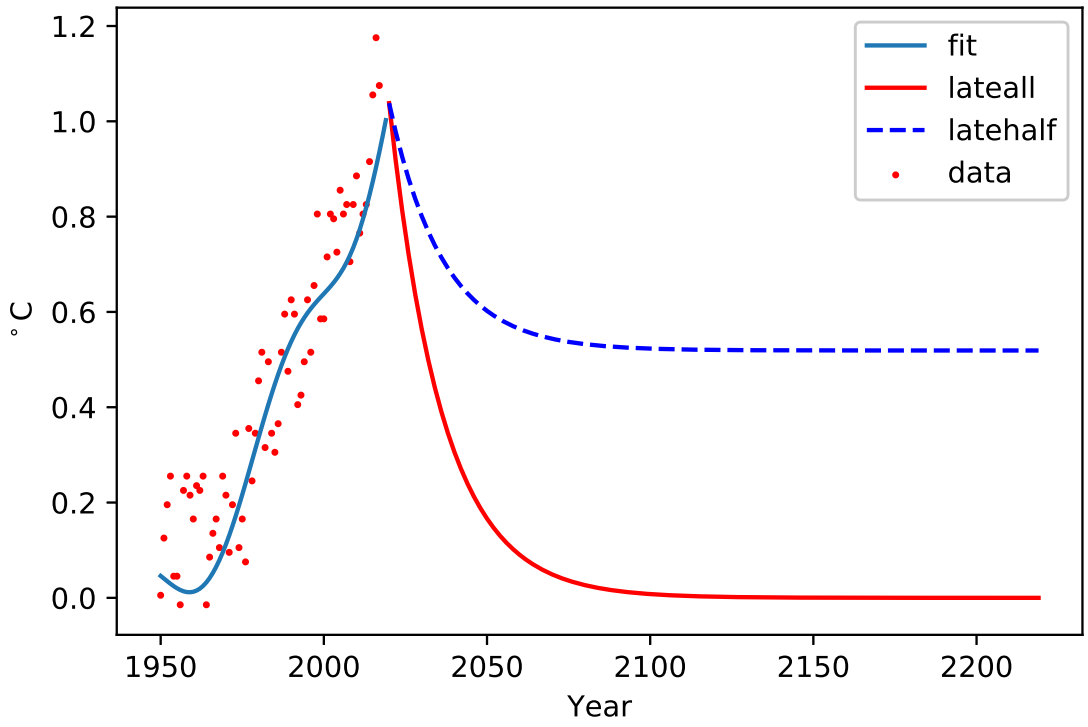

Figure 8.9. Historical (from 1950) and extrapolated change in industrial era global average with approach to equilibrium τ at 0 (solid curve) and 0.5 (dashed curve) times the value estimated for year 2020, compared to historical data from 1950–2017.

CHAPTER 9

CONCLUSIONS AND FUTURE WORK

9.1 Conclusions

The ten components of net radiative forcing in this analysis in this thesis are each formulated in a way that (a) allows for analytic integration of its impact on the linearized global heat balance over the historical data period, (b) is thus readily allows for systematic least squares calibration of the three adjustable heat balance model parameters against historical data through Julian year 2017, and is based on a hypothesis that allows for extrapolation indefinitely far into the future by numerical integration of the data-calibrated model. The calibrated heat balance described in this thesis can fit well with historical globally averaged thermometer data summarized by the IPCC. Its climate sensitivity in equilibrium is near the middle of the range estimated in the 2013 IPCC Working Group I report. The inferred surface ocean mixed layer depth of about 762 meters is qualitatively compatible with a typical thickness of an oceanic thermocline (variable temperature) layer [51]. The correction factor for adjusting global average radiative shielding from latitude and longitude dependent tropospheric aerosols from the average value used in GCMs of a factor of 1.59 is not surprising, given the difference in how this effect is treated here and in GCMs.

The the ten contributions to net radiative forcing used in this thesis are treated more comprehensively and systematically than in some other recent global heat balance models. The global heat balance parameters are also calibrated against extensive and more recent global average temperature measurements. The coding is written in an opens source platform, the code is available upon request from the author, and instructions for updating the data used as inputs to the global heat balance code are included in this thesis. Extrapolations based on user-specified modifications of any of the formulas in the model can be done

in a few seconds on a laptop computer. Examples using assumptions about solar radiation management changes in net radiative forcing are shown above in chapter 8.

The work described in this thesis is meant to provide potential users with a well documented, convenient, and flexible tool for analyzing and extrapolating estimates of changes in global average temperature. The next chapter discusses some of the extensions of the analysis that the way in which the analysis described above was formulated could be helpful.

9.2 Future Work

As discussed extensively in IPCC fifth assessment, there are huge uncertainties on the extrapolated response of global average temperature given by GCMs. The most important problem is the huge uncertainty of estimates of climate sensitivity λ. The data calibrated value of about 0.85 °K/(W/m^2) from the present global heat balance model calibration lies close to the middle of the range of uncertainty proposed by 2013 IPCC Working Group I report [37]. Thus, the next step is to calibrate and sample a joint probability distribution for those three fitting parameters described in section 7.3. Singer et al. [52] describe an approach to calibrating and sampling such a joint probability distribution by calibrating earlier historical data and a simpler radiative forcing analysis. That paper assumed that all of the differences between the global average temperature data and the underlying model can be fitted with a combination of sinusoidal functions and temporarily uncorrelated random variations.

The current work is focused on the development of a global heat balance model suitable for analysis of the impact of gradual evolution of changes in net radiative forcing. A number of authors proposed that much of the differences between the results of such a model and the historical data may be due to shorter term response to volcanic forcing, an approximately eleven year cycle in solar irradiance, and the impact of El Niño/Southern Oscillation (ENSO) cycle correlated with alternatively warm and cool surface waters in the eastern part of the Pacific Ocean. Lean [53] found that residuals between an empirical fit to anthropogenic influences on global average temperature anomaly and the historical data from 1980–2009 could be well accounted for by global average temperature fluctuations due to volcanic

aerosols, solar irradiance oscillations, and the ENSO impact. Meehl et al. [54] did a similar longer term analysis on data from 1890–2000. In that work, the authors show an example of how to subtract estimates of ENSO and approximately eleven year solar cycle irradiance oscillation effects from global average temperature data can be used to examine the short-term effects on global average temperature of volcanic eruptions. That approach and the data should allow a long-term extrapolations by calibrating the three parameters described in the current global heat balance model as well as the maximum likelihood estimates and probability distributions of those three parameters. The extrapolations of global average temperature anomaly could then be added with extrapolations of the small approximately periodic effects of ENSO and short-period solar cycle variations and a stochastic model of future volcanic eruptions. While such an approach may not capture all the uncertainty produced by GCMs, it should at least put a lower bound on the uncertainty in response to slower evolution of trends in radiative forcing.

Singer et al. [52] introduce calibration and sampling of an energy econometric model for uncertainties in the future evolution of carbon dioxide emissions from fossil fuel use. Similarly, interactive negotiations on GHGs emissions, sequestration of atmospheric carbon dioxide, and solar radiation management described by Singer and Matchett could also help quantify uncertainties in the human response to climate change. Putting all these together then give the hope of a complete and experimentally informed probability distribution for the actual future evolution of global average temperature. As with the future exercise, the simulation results would be valid in the context of the underlying assumptions in each part of the analysis. Such an exercise could provide useful insights both for the policy making process and for those who need to plan for possible evolution of the future climate, especially for those who have little influence on the global outcome. The work described in this thesis should make a useful contribution to such an exercise.

CHAPTER 10

REFERENCES

[1] C. Singer and L. Matchett, "Climate action gaming experiment: Methods and example results," *Challenges*, vol. 6, no. 2, pp. 202–228, sep 2015.

[2] *Climate Change 2013: The Physical Science Basis*. Cambridge University Pr., 2014. [Online]. Available: https://www.ebook.de/de/product/22180258/climate_change_2013_the_physical_science_basis.html

[3] "World population prospects: The 2017 revision, key findings and advance tables," United Nations, Department of Economic and Social Affairs, Population Division, Tech. Rep., 2017.

[4] A. Maddison, "Historical statistics of the world economy: 1-2008 ad." [Online]. Available: http://www.ggdc.net/maddison/oriindex.htm

[5] *State of the World's Forests 2012*. Food and Agriculture Organization of the United Nations - FAO, 2012. [Online]. Available: https://www.ebook.de/de/product/19935347/state_of_the_world_s_forests_2012.html

[6] R. J. Keenan, G. A. Reams, F. Achard, J. V. de Freitas, A. Grainger, and E. Lindquist, "Dynamics of global forest area: Results from the FAO global forest resources assessment 2015," *Forest Ecology and Management*, vol. 352, pp. 9–20, sep 2015.

[7] T. Boden, R. Andres, and G. Marland, "Global, regional, and national fossil-fuel co2 emissions (1751 - 2011) (v. 2015)," 2015. [Online]. Available: https://cdiac.ess-dive.lbl.gov/trends/emis/overview.html

[8] R. B. Jackson, C. L. Quéré, R. M. Andrew, J. G. Canadell, G. P. Peters, J. Roy, and L. Wu, "Warning signs for stabilizing global CO2 emissions," *Environmental Research Letters*, vol. 12, no. 11, p. 110202, nov 2017.

[9] D. M. Etheridge, L. P. Steele, R. L. Langenfelds, R. J. Francey, J.-M. Barnola, and V. I. Morgan, "Natural and anthropogenic changes in atmospheric CO2 over the last 1000 years from air in antarctic ice and firn," *Journal of Geophysical Research: Atmospheres*, vol. 101, no. D2, pp. 4115–4128, feb 1996.

[10] C. M. Meure, "The natural and anthropogenic variations of carbon dioxide, methane and nitrous oxide during the holocene from ice core analysis," Ph.D. dissertation, University of Melbourne, 2004.

[11] C. M. Meure, D. Etheridge, C. Trudinger, P. Steele, R. Langenfelds, T. van Ommen, A. Smith, and J. Elkins, "Law dome CO2, CH4 and N2O ice core records extended to 2000 years BP," *Geophysical Research Letters*, vol. 33, no. 14, 2006.

[12] D. F. Ferretti, "Unexpected changes to the global methane budget over the past 2000 years," *Science*, vol. 309, no. 5741, pp. 1714–1717, sep 2005.

[13] D. M. Etheridge, L. P. Steele, R. J. Francey, and R. L. Langenfelds, "Atmospheric methane between 1000 a.d. and present: Evidence of anthropogenic emissions and climatic variability," *Journal of Geophysical Research: Atmospheres*, vol. 103, no. D13, pp. 15 979–15 993, jul 1998.

[14] P. T. Ed Dlugokencky, "Globally averaged marine surface annual mean data." [Online]. Available: https://www.esrl.noaa.gov/gmd/ccgg/trends/gl_data.html

[15] D. Wuebbles, "Atmospheric methane and global change," *Earth-Science Reviews*, vol. 57, no. 3-4, pp. 177–210, may 2002.

[16] E. Dlugokencky, "Recent global ch4." [Online]. Available: www.esrl.noaa.gov/gmd/ccgg/trends_ch4/

[17] M. Crippa, D. Guizzardi, M. Muntean, E. Schaaf, F. Dentener, J. A. van Aardenne, S. Monni, U. Doering, J. G. J. Olivier, V. Pagliari, and G. Janssens-Maenhout, "Gridded emissions of air pollutants for the period 1970–2012 within EDGAR v4.3.2," *Earth System Science Data*, vol. 10, no. 4, pp. 1987–2013, oct 2018.

[18] J. H. Butler and S. A. Montzka, "The noaa annual greenhouse gas index (aggi)." [Online]. Available: https://www.esrl.noaa.gov/gmd/aggi/aggi.html

[19] Z. Hu, J. W. Lee, K. Chandran, S. Kim, and S. K. Khanal, "Nitrous oxide (n2o) emission from aquaculture: A review," *Environmental Science & Technology*, vol. 46, no. 12, pp. 6470–6480, may 2012.

[20] *Climate Change 2001: The Scientific Basis: Contribution of Working Group I to the Third Assessment Report of the Intergovernmental Panel on Climate Change*. Cambridge University Press, 2001. [Online]. Available: https://www.amazon.com/Climate-Change-2001-Contribution-Intergovernmental/dp/0521014956?SubscriptionId=AKIAIOBINVZYXZQZ2U3A&tag=chimbori05-20&linkCode=xm2&camp=2025&creative=165953&creativeASIN=0521014956

[21] G. W. Petty, *A First Course in Atmospheric Radiation (2nd Ed.)*. Sundog Publishing, 2006. [Online]. Available: https://www.amazon.com/First-Course-Atmospheric-Radiation-2nd/dp/0972903313?SubscriptionId=AKIAIOBINVZYXZQZ2U3A&tag=chimbori05-20&linkCode=xm2&camp=2025&creative=165953&creativeASIN=0972903313

[22] K. E. Trenberth, J. T. Fasullo, and J. Kiehl, "Earths global energy budget," *Bulletin of the American Meteorological Society*, vol. 90, no. 3, pp. 311–324, mar 2009.

[23] A. Henderson-Sellers, Z.-L. Yang, and R. E. Dickinson, "The project for intercomparison of land-surface parameterization schemes," *Bulletin of the American Meteorological Society*, vol. 74, no. 7, pp. 1335–1349, jul 1993.

[24] P. Monks, C. Granier, S. Fuzzi, A. Stohl, M. Williams, H. Akimoto, M. Amann, A. Baklanov, U. Baltensperger, I. Bey, N. Blake, R. Blake, K. Carslaw, O. Cooper, F. Dentener, D. Fowler, E. Fragkou, G. Frost, S. Generoso, P. Ginoux, V. Grewe, A. Guenther, H. Hansson, S. Henne, J. Hjorth, A. Hofzumahaus, H. Huntrieser, I. Isaksen, M. Jenkin, J. Kaiser, M. Kanakidou, Z. Klimont, M. Kulmala, P. Laj, M. Lawrence, J. Lee, C. Liousse, M. Maione, G. McFiggans, A. Metzger, A. Mieville, N. Moussiopoulos, J. Orlando, C. ODowd, P. Palmer, D. Parrish, A. Petzold, U. Platt, U. Pöschl, A. Prévôt, C. Reeves, S. Reimann, Y. Rudich, K. Sellegri, R. Steinbrecher, D. Simpson, H. ten Brink, J. Theloke, G. van der Werf, R. Vautard, V. Vestreng, C. Vlachokostas, and R. von Glasow, "Atmospheric composition change – global and regional air quality," *Atmospheric Environment*, vol. 43, no. 33, pp. 5268–5350, oct 2009.

[25] M. P. McCormick, L. W. Thomason, and C. R. Trepte, "Atmospheric effects of the mt pinatubo eruption," *Nature*, vol. 373, no. 6513, pp. 399–404, feb 1995.

[26] M. Sigl, M. Winstrup, J. R. McConnell, K. C. Welten, G. Plunkett, F. Ludlow, U. Büntgen, M. Caffee, N. Chellman, D. Dahl-Jensen, H. Fischer, S. Kipfstuhl, C. Kostick, O. J. Maselli, F. Mekhaldi, R. Mulvaney, R. Muscheler, D. R. Pasteris, J. R. Pilcher, M. Salzer, S. Schüpbach, J. P. Steffensen, B. M. Vinther, and T. E. Woodruff, "Timing and climate forcing of volcanic eruptions for the past 2,500 years," *Nature*, vol. 523, no. 7562, pp. 543–549, jul 2015.

[27] S. M. Andersson, B. G. Martinsson, J.-P. Vernier, J. Friberg, C. A. M. Brenninkmeijer, M. Hermann, P. F. J. van Velthoven, and A. Zahn, "Significant radiative impact of volcanic aerosol in the lowermost stratosphere," *Nature Communications*, vol. 6, no. 1, jul 2015.

[28] D. H. Douglass, "Climate forcing by the volcanic eruption of mount pinatubo," *Geophysical Research Letters*, vol. 32, no. 5, 2005.

[29] G. Kopp, K. Heuerman, and G. Lawrence, "The total irradiance monitor (TIM): Instrument calibration," in *The Solar Radiation and Climate Experiment (SORCE)*. Springer New York, pp. 111–127.

[30] N. A. Krivova, L. E. A. Vieira, and S. K. Solanki, "Reconstruction of solar spectral irradiance since the maunder minimum," *Journal of Geophysical Research: Space Physics*, vol. 115, no. A12, pp. n/a–n/a, dec 2010.

[31] W. T. Ball, Y. C. Unruh, N. A. Krivova, S. Solanki, T. Wenzler, D. J. Mortlock, and A. H. Jaffe, "Reconstruction of total solar irradiance 1974–2009," *Astronomy & Astrophysics*, vol. 541, p. A27, apr 2012.

[32] K. L. Yeo, N. A. Krivova, S. K. Solanki, and K. H. Glassmeier, "Reconstruction of total and spectral solar irradiance from 1974 to 2013 based on KPVT, SoHO/MDI, and SDO/HMI observations," *Astronomy & Astrophysics*, vol. 570, p. A85, oct 2014.

[33] K. L. Yeo, N. A. Krivova, and S. K. Solanki, "Solar cycle variation in solar irradiance," *Space Science Reviews*, vol. 186, no. 1-4, pp. 137–167, jul 2014.

[34] F. Steinhilber, J. Beer, and C. Fröhlich, "Total solar irradiance during the holocene," *Geophysical Research Letters*, vol. 36, no. 19, oct 2009.

[35] K. G. McCracken, J. Beer, F. Steinhilber, and J. Abreu, "A phenomenological study of the cosmic ray variations over the past 9400 years, and their implications regarding solar activity and the solar dynamo," *Solar Physics*, vol. 286, no. 2, pp. 609–627, apr 2013.

[36] K. Fraedrich, "Catastrophes and resilience of a zero-dimensional climate system with ice-albedo and greenhouse feedback," *Quarterly Journal of the Royal Meteorological Society*, vol. 105, no. 443, pp. 147–167, jan 1979.

[37] U. Cubasch, D. Wuebbles, D. Chen, M. Facchini, D. Frame, N. Mahowald, and J.-G. Winther, "Introduction. in: Climate change 2013: The physical science basis," Contribution of Working Group I to the Fifth Assessment Report of the Intergovernmental Panel on Climate Change [Stocker, T.F., D. Qin, G.-K. Plattner, M. Tignor, S.K. Allen, J. Boschung, A. Nauels, Y. Xia, V. Bex and P.M. Midgley (eds.)]. Cambridge University Press, Cambridge, United Kingdom and New York, NY, USA., Tech. Rep., 2013.

[38] M. E. Mann and P. D. Jones, "Global surface temperatures over the past two millennia," *Geophysical Research Letters*, vol. 30, no. 15, aug 2003.

[39] J. Hansen, R. Ruedy, M. Sato, and K. Lo, "GLOBAL SURFACE TEMPERATURE CHANGE," *Reviews of Geophysics*, vol. 48, no. 4, dec 2010.

[40] G. Schmidt and B. Schmunk, "Giss surface temperature analysis (gistemp). nasa goddard institute for space studies. dataset accessed 2018-12-07 at data.giss.nasa.gov/gistemp/." 2018.

[41] K. Rypdal, "Global warming projections derived from an observation-based minimal model," *Earth System Dynamics*, vol. 7, no. 1, pp. 51–70, jan 2016.

[42] NASA, "Measuring earth's albedo," 2014. [Online]. Available: https://earthobservatory.nasa.gov/images/84499/measuring-earths-albedo

[43] T. Mauritsen, R. G. Graversen, D. Klocke, P. L. Langen, B. Stevens, and L. Tomassini, "Climate feedback efficiency and synergy," *Climate Dynamics*, vol. 41, no. 9-10, pp. 2539–2554, may 2013.

[44] K. L. Swanson, G. Sugihara, and A. A. Tsonis, "Long-term natural variability and 20th century climate change," *Proceedings of the National Academy of Sciences*, vol. 106, no. 38, pp. 16 120–16 123, sep 2009.

[45] G. Myhre, E. J. Highwood, K. P. Shine, and F. Stordal, "New estimates of radiative forcing due to well mixed greenhouse gases," *Geophysical Research Letters*, vol. 25, no. 14, pp. 2715–2718, jul 1998.

[46] O. Geoffroy, D. Saint-Martin, D. J. L. Olivié, A. Voldoire, G. Bellon, and S. Tytéca, "Transient climate response in a two-layer energy-balance model. part i: Analytical solution and parameter calibration using CMIP5 AOGCM experiments," *Journal of Climate*, vol. 26, no. 6, pp. 1841–1857, mar 2013.

[47] L. Resplandy, R. F. Keeling, Y. Eddebbar, M. K. Brooks, R. Wang, L. Bopp, M. C. Long, J. P. Dunne, W. Koeve, and A. Oschlies, "Quantification of ocean heat uptake from changes in atmospheric O2 and CO2 composition," *Nature*, vol. 563, no. 7729, pp. 105–108, oct 2018.

[48] C. Singer, T. Milligan, and T. Rethinaraj, "How china's options will determine global warming," *Challenges*, vol. 5, no. 1, pp. 1–25, dec 2013.

[49] U. Satish, M. J. Mendell, K. Shekhar, T. Hotchi, D. Sullivan, S. Streufert, and W. J. Fisk, "Is CO 2 an indoor pollutant? direct effects of low-to-moderate CO 2 concentrations on human decision-making performance," *Environmental Health Perspectives*, vol. 120, no. 12, pp. 1671–1677, dec 2012.

[50] A. V. Eliseev and I. I. Mokhov, "Carbon cycle–climate feedback sensitivity to parameter changes of a zero-dimensional terrestrial carbon cycle scheme in a climate model of intermediate complexity," *Theoretical and Applied Climatology*, vol. 89, no. 1-2, pp. 9–24, oct 2006.

[51] NOAA, "What is a thermocline ?" National Oceanic Service website, Tech. Rep., 2018. [Online]. Available: https://oceanservice.noaa.gov/facts/thermocline.hmtl

[52] C. E. Singer, T. S. G. Rethinaraj, S. Addy, D. Durham, M. Isik, M. Khanna, B. Kuehl, J. Luo, W. Quimio, K. Rajendran, D. Ramirez, J. Qiang, J. Scheffran, T. N. Tiouririne, and J. Zhang, "Probability distributions for carbon emissions and atmospheric response," *Climatic Change*, vol. 88, no. 3-4, pp. 309–342, apr 2008.

[53] J. L. Lean, "Cycles and trends in solar irradiance and climate," *Wiley Interdisciplinary Reviews: Climate Change*, vol. 1, no. 1, pp. 111–122, dec 2009.

[54] G. A. Meehl, W. M. Washington, C. M. Ammann, J. M. Arblaster, T. M. L. Wigley, and C. Tebaldi, "Combinations of natural and anthropogenic forcings in twentieth-century climate," *Journal of Climate*, vol. 17, no. 19, pp. 3721–3727, oct 2004.

APPENDIX A

USER MANUAL

This appendix explains how to access the codes used in this thesis if you contact the author at `cd7@illinois.edu` or `acdis@illinois.edu` or for information about where the codes are stored. The author may then provide that information or information on how to access and use a later version of the codes.

A.1 Get started

This section explains how to download Github Desktop and the Jupyter notebook applications and the process of installing them on computers.

A.2 Create a GitHub account

Note that it is only to create a GitHub account necessary if you do not already have one.

Step 1. Visit https://github.com, select the "Sign up" option in the upper right of the screen and fill out the requested personal information.

Step 2. Select the green "Create an account" button at the bottom of the page.

Step 3. Choose the free plan, and do not select any of the checkboxes. Then select the green "Continue" button at the bottom of the page. If a pop-up window appears below the GitHub search bar, select the "Got It."

Step 4. Scroll to the bottom of the page and select to "skip this step."

Step 5. Check the email that was given to GitHub for a verification email. If there is a verification email in the inbox, select the email and click on the link to verify email address.

Step 6. This process of the user manual instructing is now done. Move on to the next part. You can close the web browser or the browser tab if you are working on other things in the browser.

A.3 Install GitHub Desktop

A.3.1 Install on a Windows machine

Step 1. Visit the GitHub Desktop download page at https://desktop.github .com/.

Step 2. Select the "Download for Windows" button in the center of the webpage. If requested to download/save file, select to "Save File"

Step 3. In your computer's destination folder, locate and double-click GitHub Desktop. (The file's name is GitHubDesktopSetup.exe)

Step 4. After GitHub Desktop has been installed, it will be launched automatically. Then on the left side of the new pop-up window, select "Sign into GitHub.com," and then enter the username and password for your GitHub account, and then click blue "Sign in" button.

Step 5. Press the blue "Continue" button on the new window called "Configure Git".

Step 6. Press the blue "Finish" button on the new window called "Make GitHub Desktop better".

A.3.2 Install on a Mac machine

Step 1. Visit the GitHub Desktop download page at https://desktop.github .com/.

Step 2. Select the "Download for macOS" button in the center of the webpage. If requested to download/save file, select to "Save File". Open the zipped document if it is zipped.

Step 3. In your computer's destination folder, locate and double-click GitHub Desktop. (The file's name is GitHub Desktop)

Step 3.1. Open GitHub if prompted by a security check informing that the source was downloaded online.

Step 4. After GitHub Desktop has been installed, the window for GitHub should open it up. If it does not, double-click on GitHub Desktop.

Step 5. On the left side of the new window, select "Sign into GitHub.com," and then enter the username and password for your GitHub account, and then click the blue "Sign in" button.

Step 6. Press the blue "Continue" button on the new window called "Configure Git".

Step 7. Press the blue "Finish" button on the new window called "Make GitHub Desktop better."

A.4 Install Jupyter through Anaconda 5.2

A.4.1 Install on a Windows Machine

Step 1. Visit the Anaconda download page at https://www.anaconda.com /download/.

Step 2. Select the green "Download" button for "Python 3.6 version" near the center of the web page. Close any window that pops up on the browser.

Step 3. Go to the designated download area on computer, double-click the file name "Anaconda3-5.2.0-Windows-x86_64.exe".

Step 4. On the pop-up window for Anaconda3 5.2.0 Setup, select "Next" button in the bottom of the window.

Step 5. Read the "Software License Agreement" and press "I Agree" in the pop-up window.

Step 6. On the new pop-up window of "Select Installation Type", click "Just Me", and then click "Next" button.

Step 7. On the new pop-up window of "Choose Install Location", click "Next" button.

Step 8. On the new pop-up window of "Advanced Installation Options", uncheck the first box and check the second box. Then, click the "Install" button.

Step 9. It will take a few minutes to install. After installation is completed, click "Next" button.

Step 10. In the window that pops up, titled "Microsoft Visual Studio Code Installation", select the "Skip" button in the bottom.

Step 11. In the final window, uncheck both boxes, and click the "Finish" button in the bottom.

A.4.2 Install on a Mac machine

Step 1. Visit the Anaconda download page at https://www.anaconda.com /download/.

Step 2. Select green "Download" button for "Python 3.6 version" near the center of the web page. If a window pops up, select to save the file to the designated download folder. Close any window that pops up on the browser.

Step 3. Go to the designated download folder on the Mac, double-click the file name "Anaconda3-5.2.0-MacOSX-x86_64.pkg".

Step 4. On the pop-up window for installing Anaconda3, select the blue "Continue" button to determine if the software can be installed.

Step 5. Press "Continue" button on "Anaconda3 Installer", read the "Read Me", and press the "Continue" button. Read the "Software License Agreement" and press "Continue" button and "Agree" in the pop-up window.

Step 6. Select the "Install" button in the bottom right of the installation window. It will take awhile to download. If given the option to install for all users or just for you, select "Install for me only" and press the "Continue" button.

Step 7. In the window that pops up, titled "Microsoft Visual Studio Code", select the "Continue" button in the bottom right. In the final window, select the blue "Close" button in the bottom right. If prompted to move the installer to the trash, do so.

A.5 Write Python code and run it on jupyter Notebook

Step 1. Go to your GitHub working folder, click "Documents", and then find the "GitHub" folder.

Step 2. Click "CAGE" if you have created this repository in the previous step. Then, click "Python". You can create a new Python 3 jupyter Notebook by selecting "New" button under this folder. Then, an untitled python 3 notebook will be created. You can select it and rename it, e.g. as "`CAGE_Population`". Then, you can open it and start to write your code. Step 3. When input box is in "code" mode, you can write your code. But when you want to add some comments, then you will need to select "Markdown" from the menu shown on top of your input boxes. Step 4. Run a code cell using Shift-Enter. Also, you can cut or delete a cell by clicking the Edit button. If you want a new cell, press "insert". You can either insert below or above the cell you are working with.

Step 5. After you have finished compiling code, you can click "cell" tab in the main menu, and choose "Run All" to run all the cells.

Step 6. You can save your code by clicking "File", and select "Save and Checkpoint".

Step 7. If there is any error message, you need to go back and fix bugs before running the code.

A.6 Push Python code onto GitHub and Pull code down from GitHub

Step 1. Whenever, you have made changes to your file, you can easily upload it to GitHub, and share with other members.

Step 2. First, open GitHub Desktop, and click "Fetch Origin". The changed files will pop up on the left side. Then, check the file you want to upload and input the required summary describing what changes you have made. Add any description if you want. Then, click commit to master.

Step 3. After that, you will find that the button "Fetch Origin" becomes "Push" button. Press "Push", and your code will be updated on GitHub.

Step 4. You can click "History" to view changes that have been made.

Step 5. When your members have changed any files and updated on Github, you can also click "Pull" button on GitHub Desktop, and then you can get the updated code.

APPENDIX B

POPULATION CODE

B.1 Clone CAGE repository from GitHub

Step 1. In the "File" menu, click the "Clone Repository" button.

Step 2. Click the tab that corresponds to the location of the repository you want to clone. You can also click "URL" button to manually enter the repository location.

Step 3. Choose the repository you want to clone from the list.

Step 4. Click "Choose..." and using Windows Explorer, navigate to a local path where you want to clone the repository. For example, you can choose `C:\Users\Administrator\Documents\GitHub` as the directory.

Step 5. Click "Clone".

B.2 Get ready for sample input files

Download `cage17sep18pop1820-2100un.xlsx` from Compass 2g website. It is shown as Table B.1 below.

B.3 How to run the code

Step 1. Open the Jupyter notebook, navigate to `CAGE_Population_Code`, and open it.

Step 2. Change the working directory accordingly, move the downloaded `cage17sep18pop1820-2100un.xlsx` to the same working directory, and press Shift-Enter to run the code.

Table B.1. Total Population (1000s)

Yr	1820	1840	1860	1880	1900	1920	1940	1960
0	1056503	1179337	1245144	1368834	1593810	1881983	2314820	3033112
1	1063629	1184464	1249023	1379431	1608967	1891855	2329429	3090190
2	1070834	1189571	1252987	1390390	1624431	1908822	2345731	3149131
3	1078075	1194611	1257027	1401188	1639752	1927974	2361361	3210163
4	1085371	1199786	1261106	1412333	1655368	1948995	2376833	3273553
5	1092713	1204998	1265230	1423371	1671105	1970574	2389124	3339480
6	1100021	1210100	1269096	1434429	1686871	1992567	2404720	3407999
7	1107329	1214396	1273073	1445554	1702792	2014129	2433294	3478942
8	1114666	1218060	1276870	1456936	1719161	2035658	2464630	3551759
9	1122039	1222244	1281358	1468555	1735780	2056479	2498399	3625795
10	1129434	1226656	1288286	1480165	1752408	2076964	2536167	3700459
11	1134240	1227642	1294301	1490723	1769377	2100596	2583706	3775677
12	1139030	1229190	1301725	1501437	1785036	2123173	2630481	3851424
13	1143851	1230876	1309634	1512197	1805135	2145500	2677124	3927410
14	1148641	1232457	1317705	1523350	1819477	2167425	2724197	4003325
15	1153703	1234271	1325862	1534610	1831093	2190090	2772141	4078963
16	1158718	1236193	1334439	1546089	1842402	2213218	2821288	4154162
17	1163798	1238232	1343128	1557925	1853272	2238412	2871851	4229076
18	1168914	1240422	1351663	1569905	1862545	2264521	2923972	4304246
19	1174091	1242725	1360388	1581907	1868260	2291233	2977716	4380471

Table B.1. Total Population (1000s) Continued

Yr	1980	2000	2020	2040	2060	2080	2100
0	4458280	6144860	7795310	9210163	10222416	10848533	11184193
1	4537719	6223267	7875291	9270880	10261696	10871687	
2	4618644	6302001	7954296	9330672	10300017	10894125	
3	4701405	6381263	8032319	9389478	10337428	10915880	
4	4786355	6461222	8109364	9447273	10373963	10936949	
5	4873654	6542007	8185442	9504039	10409634	10957391	
6	4963501	6623686	8260537	9559728	10444464	10977173	
7	5055498	6706262	8334628	9614362	10478481	10996321	
8	5148420	6789610	8407736	9667908	10511684	11014833	
9	5240603	6873586	8479866	9720341	10544076	11032672	
10	5330802	6958018	8551028	9771647	10575656	11049881	
11	5418618	7042858	8621238	9821804	10606466	11066412	
12	5504260	7128025	8690501	9870826	10636476	11082285	
13	5587961	7213266	8758794	9918687	10665702	11097491	
14	5670181	7298291	8826138	9965411	10694132	11112024	
15	5751330	7382849	8892529	10010987	10721788	11125862	
16	5831416	7466803	8957952	10055437	10748646	11138995	
17	5910426	7550100	9022412	10098745	10774737	11151424	
18	5988698	7632654	9085932	10140980	10800068	11163111	
19	6066734	7714409	9148503	10182188	10824670	11174044	

B.4 Sample output files

Step 1. You will get `CAGE_Pop_Parameters.xlsx` and `pop.eps` file from your working directory.

Step 2. In `CAGE_Pop_Parameters.xlsx` excel sheet, the code saves the fitted parameters' values. It is shown as Table B.2 below.

Table B.2. CAGE_Pop_Parameters

Name	Values	Units	Meaning
b1	10.66438	Year	Saturation value
b2	2003.344	Julian Year	Inflection time
b3	31.48011	Year	Inverse of logistic growth rate

Step 3. The file `pop.eps` shows the logistic function fit for global population.

APPENDIX C

DEFORESTATION CODE

C.1 Get ready for sample input files

Step 1. Go to (https://automeris.io/WebPlotDigitizer/), on the right side, click "Launch Now".

Step 2. Click "Load Image" button, and choose the figure you downloaded from Compass 2g. Then choose Plot Type as 2D(X-Y) Plot and click "Align Axes" button.

Step 3. Then, click "Proceed" button. In this step, we need to click four known points on the axes in the order shown in red. Two on the X axis (X1, X2) and two on the Y axis (Y1, Y2).

Step 4. After you finish picking four points, click "complete!" button on the right side.

Step 5. In the pop-up window, insert the points "coordinates" value, and select OK.

Step 6. Then, you can manually add points on deforestation curve. Also, you can adjust points you click by clicking "Adjust Point". Be as accurate as possible, make sure that points you click are sitting on the curve for each year.

Step 7. After that, you can click "View data" and those "coordinates" values can be either saved as a csv file and downloaded or you can copy to clipboard and paste it in excel sheet.

Step 8. If you copy and paste data into excel sheet, you can insert a line as a header, by input "Year" and "Deforestation".

Step 9. Save this excel sheet as graph data.xlsx. It is shown as Table C.1 below.

Table C.1. Graph Data

Year	Deforestation(Gha)
1799.97	0.840283
1809.975	0.859364
1819.979	0.889046
1829.983	0.910247
1839.986	0.939929
1849.99	0.969611
1859.993	0.999293
1869.996	1.031095
1879.998	1.077739
1890	1.120141
1900.001	1.168905
1910.001	1.219788
1920.002	1.268551
1930.003	1.319435
1940.004	1.368198
1950.005	1.419081
1960.005	1.478445
1970.004	1.539929
1980.003	1.607774
1989.999	1.69682
1999.998	1.758304
2009.999	1.809187

C.2 How to run the code

Step 1. Open the Jupyter notebook, navigate to `CAGE_Deforestation_Code`, and open it.
Step 2. In the second line, Change the working directory accordingly and in line 21, change the directory to the location where you store `CAGE_Pop_Parameters.xlsx` file, and press Shift-Enter to run the code.

C.3 Sample output files

Step 1. You will get `heat18jun06deforest.csv` shown as Table C.2 below and a deforest.eps file from your working directory.

Step 2. In the `heat18jun06deforest.csv` file, it saves the deforestation area from the year 1800 to 2015.
Step 3. The figure deforest.eps shows the logistic function fit for global deforestation. Also, the csv file titled as `CAGE_Deforest_Parameters` saved the fitted parameters results. It is shown as Table C.3 below.

Table C.2. heat18jun06deforest.csv

Year	Deforestation(Gha)
1799.97	0.840283
1809.975	0.859364
1819.979	0.889046
1829.983	0.910247
1839.986	0.939929
1849.99	0.969611
1859.993	0.999293
1869.996	1.031095
1879.998	1.077739
1890	1.120141
1900.001	1.168905
1910.001	1.219788
1920.002	1.268551
1930.003	1.319435
1940.004	1.368198
1950.005	1.419081
1960.005	1.478445
1970.004	1.539929
1980.003	1.607774
1989.999	1.69682
1999.998	1.758304
2009.999	1.809187
2015	1.825726
6/13/18	Deforestation.py

Table C.3. CAGE_Deforest_Parameters

Name	Values	Units	Meaning
b1	3.46566	Year	Saturation value
b2	2003.34	Julian Year	Inflection time
b3	162.813	Year	Inverse of logistic growth rate

APPENDIX D

CO_2 INDUSTRIAL EMISSION CODE

D.1 Get ready for sample input files

Step 1. Download `heat17emtic.1751-2017dec11.xlsx` from Compass 2g website.

D.2 How to run the code

Step 1. Run Jupyter notebook, navigate to the code named`"CAGE_CO2_industry"`, and open it.

Step 2. Change the working directory accordingly, and moves the downloaded `heat17emtic.1751-2017dec11.xlsx` to the same working directory, and press Shift-Enter to run the code.

D.3 Sample output files

Table D.1. CO_2 Industrial Emission Fitted Parameters

Name	Values	Units	Meaning
b1	18.2520	Year	Saturation value
b2	2011.18	Julian Year	Inflection time
b3	29.3045	Year	Inverse of logistic growth rate

APPENDIX E

CO_2 LAND USE EMISSION CODE

E.1 Get ready for sample input files

Step 1. Download `Global_land_use_flux_1850_2005.xlsx` from Compass 2g website.

E.2 How to run the code

Step 1. Run the Jupyter notebook, navigate to the code named`"CAGE_CO2 _landuse"`, and open it.

Step 2. Change the working directory accordingly, and moves the downloaded `Global_land_use_flux_1850_2005.xlsx` to the same working directory, and press Shift-Enter to run the code.

E.3 Sample output files

Table E.1. CO_2 Land Use Emission Fitted Parameters

Name	Values	Units	Meaning
b1	3.46566	Year	Saturation value
b2	2003.34	Julian Year	Inflection time
b3	162.813	Year	Inverse of logistic growth rate
b8	121.98415		Constant multiplier

Table E.2. CO_2 Land Use Emission Fitted Parameters

Name	Values
b1	0.199856
b2	1932.79
b3	5.56387

Table E.3. CO_2 Land Use Emission Fitted Parameters

Name	Values
b1	0.770546
b2	1959.73
b3	9.13108

Table E.4. CO_2 Land Use Emission Fitted Parameters

Name	Values
b1	0.964413
b2	1993.15
b3	15.2196

APPENDIX F

CH_4 PRE-INDUSTRIAL CONCENTRATION CODE

F.1 Get ready for sample input files

Step 1. Download `cage17lawdome1-2004nov02_ud.xlsx`,
`NOAA_MoleFractions_2016_ud.xlsx`, and `NOAAESRL.xlsx` from Compass 2g website.

F.2 How to run the code

Step 1. Run the Jupyter notebook, navigate to the code named"`CAGE_Pre_CH4`", and open it.
Step 2. Change the working directory accordingly, move the downloaded three excel sheets to the same working directory, go back to Jupyter notebook, and press Shift-Enter to run the code.

F.3 Sample output files

Table F.1. CH_4 Pre-industrial Concentration Fitted Parameters

Name	Values	Units	Meaning
b1	64.1562	ppb	Saturation value
b2	871.32	Julian Year	Inflection time
b3	237.898	Year	Inverse of logistic growth rate
b4	667.982	ppb	Initial atmospheric concentration of methane

APPENDIX G

CH_4 POST-1749 CONCENTRATION CODE

G.1 Get ready for sample input files

Step 1. Download `heat17ch4emitdec14.xlsx` from Compass 2g website.

G.2 How to run the code

Step 1. Run the Jupyter notebook, navigate to the code named"`CAGE_Post_CH4`", and open it.

Step 2. Change the working directory accordingly, move the downloaded three excel sheets to the same working directory, go back to Jupyter notebook, and press Shift-Enter to run the code.

G.3 Sample output files

Table G.1. CH_4 Post-1749 Concentration Fitted Parameters

Name	Values	Units	Meaning
b1	176.655	ppb	Saturation value
b2	1973.91	Julian Year	Inflection time
b3	41.3836	Year	Inverse of logistic growth rate
b4	9.51428	Year	Atmospheric lifetime of methane

APPENDIX H

N_2O PRE-INDUSTRIAL CONCENTRATION CODE

H.1 Get ready for sample input files

Step 1. Download `cage17lawdome1-2004nov02_ud.xlsx` and `NOAA_MoleFractions_2016_ud.xlsx` from Compass 2g website.

H.2 How to run the code

Step 1. Run the Jupyter notebook, navigate to the code named"`CAGE_Pre_N2O`", and open it.

Step 2. Change the working directory accordingly, move the downloaded excel sheets to the same working directory, go back to the Jupyter notebook, and press Shift-Enter to run the code.

H.3 Sample output files

Table H.1. N_2O Pre-Industrial Concentration Fitted Parameters

Name	Values	Units	Meaning
b1	5.14088	ppb	Saturation value
b2	735.908	Julian Year	Inflection time
b3	7.2796	Year	Inverse of logistic growth rate
b4	262.15	ppb	Initial atmospheric concentration of nitrous oxide

APPENDIX I

N_2O POST-1749 CONCENTRATION CODE

I.1 Get ready for sample input files

Step 1. Download `heat18n2oemitjul17.csv`, and `CAGE_Pop_Parameters.csv` from Compass 2g website.

I.2 How to run the code

Step 1. Run the Jupyter notebook, navigate to the code named
"`CAGE_N2O_post1750`", and open it.
Step 2. Change the working directory accordingly, move the downloaded excel sheets to the same working directory, go back to Jupyter notebook, and press Shift-Enter to run the code.

I.3 Sample output files

Table I.1. N_2O Post-1749 Concentration Fitted Parameters

Name	Values	Units	Meaning
b1	2.39098	ppb	Saturation value
b2	2003.34	Julian Year	Inflection time
b3	40.3178	Year	Inverse of logistic growth rate

APPENDIX J

OTHER WELL MIXED GREENHOUSE GASES AND CONTRAILS RADIATIVE FORCING CODE

J.1 Get ready for sample input files

Step 1. Download `WG1AR5_AIISM_Datafiles.xlsx`, and

`Other_graph_data.xlsx`, which is shown as Table J.1 below, from Compass 2g website.

Table J.1. Other Well Mixed Greenhouse Gases graph data

Years(Julian)	Radiative Forcing(W/m^2)
1934.943	0.002475
1940	0.00495
1944.943	0.007426
1950	0.009901
1954.943	0.014851
1959.885	0.024752
1964.943	0.042079
1969.885	0.071782
1974.943	0.123762
1980	0.183168
1984.943	0.235149
1990	0.299505
1994.943	0.329208
2000	0.339109
2004.943	0.346535
2010	0.35396

J.2 How to run the code

Step 1. Run the Jupyter notebook, navigate to the code named"`CAGE_Other`", and open it.
Step 2. Change the working directory accordingly, move the downloaded three excel sheets to the same working directory, go back to the Jupyter notebook, and press Shift-Enter to run the code.

J.3 Sample output files

Table J.2. Other Well Mixed Greenhouse Gases Radiative Forcing Fitted Parameters

Name	Values	Units	Meaning
b1	0.360664	W/m^2	Saturation value
b2	1980.04	Julian Year	Inflection time
b3	7.5219	Year	Inverse of logistic growth rate

Table J.3. Contrails Radiative Forcing Fitted Parameters

Name	Values	Units	Meaning
b1	0.169096	W/m^2	Saturation value
b2	2026.34	Julian Year	Inflection time
b3	17.8118	Year	Inverse of logistic growth rate

APPENDIX K

AEROSOLS LESS BLACK CARBON ON SNOW RADIATIVE FORCING CODE

K.1 Get ready for sample input files

Step 1. Download `OtherForcings.csv` from Compass 2g website.

K.2 How to run the code

Step 1. Run the Jupyter notebook, navigate to the code named"`CAGE_Aerosol_BlackCarbon_Ozone`", and open it.

Step 2. Change the working directory accordingly, move the downloaded excel sheet to the same working directory, go back to the Jupyter notebook, and press Shift-Enter to run the code.

K.3 Sample output files

Table K.1. Aerosols less Black Carbon on Snow Radiative Forcing Fitted Parameters

Name	Values	Units	Meaning
b1	0.577154	W/m^2	
b2	2001.19	Julian Year	
b3	28.4973	Year	
b4	131.852		constant multiplier

Table K.2. Tropospheric Ozone Radiative Forcing Fitted Parameters

Name	Values	Units	Meaning
b1	0.30468	W/m^2	
b2	2008.2	Julian Year	
b3	36.5573	Year	
b4	42.1605		constant multiplier

APPENDIX L

LAND USE ALBEDO RADIATIVE FORCING CODE

L.1 Get ready for sample input files

Step 1. Download `OtherForcings.csv` from Compass 2g website.

L.2 How to run the code

Step 1. Run the Jupyter notebook, navigate to the code named"`CAGE_Albedo`", and open it.

Step 2. Change the working directory accordingly, move the downloaded excel sheet to the same working directory, go back to the Jupyter notebook, and press Shift-Enter to run the code.

L.3 Sample output files

Table L.1. Land Use Albedo Radiative Forcing Fitted Parameters

Name	Values	Units	Meaning
b1	0.147705	W/m^2	Saturation value
b2	1952.34	Julian Year	Inflection time
b3	20.064	1/Year	Inverse of logistic growth rate

Table L.2. Land Use Albedo Radiative Forcing Fitted Parameters

Name	Values	Units	Meaning
b1	8.50988	Year	Constant multiplier
b2	1893.04	Julian Year	Inflection time
b3	42.944	Year	Inverse of logistic growth rate

APPENDIX M

LINEAR APPROXIAMTION OF GREENHOUSE GASES' RADIATIVE FORCING CODE

M.1 Get ready for sample input files

Step 1. Download NOAA ANNUAL GREENHOUSE GAS INDEX (AGGI) from https://www.esrl.noaa.gov/gmd/aggi/aggi.html.

M.2 How to run the code

Step 1. Run the Jupyter notebook, navigate to the code named"`CAGE_Linear`", and open it.

Step 2. Change the working directory accordingly, move the downloaded excel sheet to the same working directory, go back to the Jupyter notebook, and press Shift-Enter to run the code.

M.3 Sample output files

Table M.1 lists parameters used to relate atmospheric concentra-tions of those gases to radiative forcing. In the Table M.1, the linear radiative forcing formula for those three GHGs take the form of $S_x(x - x_0)$.

Table M.1. Linear Forcing Formula Parameters

Type	$<X_0>$	units	Formula	S_X ((W/m^2)/units)	X
1	277.8529	ppm	Linear	0.01653708	$<CO_2>$
2	732.1388	ppb	Linear	0.00048336	$<CH_4>$
3	267.2913	ppb	Linear	0.00309776	$<N_2O>$

APPENDIX N

VOLCANIC RADIATIVE FORCING CODE

N.1 Get ready for sample input files

Step 1. Download heat17volcanoshield491bc-2011dec28.xlsx from Compass 2g website.

N.2 How to run the code

Step 1. Run the Jupyter notebook, navigate to the code named "`CAGE_Volcanic`", and open it.

Step 2. Change the working directory accordingly, move the downloaded excel sheet to the same working directory, go back to the Jupyter notebook, and press Shift-Enter to run the code.

N.3 Sample output files

Table N.1. Volcanic Radiative Forcing Fitted Parameters

Name	Values	Units	Meaning
b1	0.476273		Growth rate
b2	1795.5	Julian Year	Inflection time
b3	2	Year	Inverse of logistic growth rate

Table N.2. Volcanic Radiative Forcing Fitted Parameters

Name	Values	Units	Meaning
b1	1.10145		Growth rate
b2	1819	Julian Year	Inflection time
b3	2	Year	Inverse of logistic growth rate

Table N.3. Volcanic Radiative Forcing Fitted Parameters

Name	Values	Units	Meaning
b1	0.183586	1/Year	Growth rate
b2	1819	Julian Year	Inflection time
b3	2	Year	Inverse of logistic growth rate

APPENDIX O

SOLAR IRRADIANCE RADIATIVE FORCING CODE

O.1 Get ready for sample input files

Step 1. Download `heat17dec30irradiance1610-2017.xlsx` from Compass 2g website.

O.2 How to run the code

Step 1. Run the Jupyter notebook, navigate to the code named "`CAGE_Solar Irradiance`", and open it.

Step 2. Change the working directory accordingly, move the downloaded excel sheet to the same working directory, go back to the Jupyter notebook, and press Shift-Enter to run the code.

O.3 Sample output files

Table O.1. Solar Irradiance Radiative Forcing Fitted Parameters

Name	Values	Units	Meaning
b1	0.15466	W/m^2	
b2	841.916	Year	Phase
b3	217.337	Year	Period

Table O.2. Solar Irradiance Radiative Forcing Fitted Parameters

Name	Values	Units	Meaning
b1	0.0461415	W/m^2	
b2	1566.39	Year	Phase
b3	40.9932	Year	Period

Table O.3. Solar Irradiance Radiative Forcing Fitted Parameters

Name	Values	Units
b1	0.131567	W/m^2
b2	1854.18	Year
b3	242	Year

Table O.4. Solar Irradiance Radiative Forcing Fitted Parameters

Name	Values	Units
b1	0.182904	W/m^2
b2	2013.95	Julian Year
b3	60.5	Year

APPENDIX P

PARAMETERS SUMMARY

The tables in this section list numerical values of parameters used in this thesis. Table P.1 lists parameters used to fit estimates of CO_2, CH_4 and N_2O emissions. Table P.2 lists values of various other relevant constants. Table P.4 lists parameters used to fit data on atmospheric concentrations of those gases. Together with the information in Table M.1, those parameters allow estimates of radiative forcing. Although the parameters in Tables M.1 and P.4 are sufficient for producing analytic fits to estimates of radiative forcing, the parameters in Table P.1 are included to support future work on extrapolation of emissions, atmospheric concentrations, and radiative forcing.

Table P.1. Emissions Parameters

Type	b_1	b_1 units	b_2 (yr)	b_3 (yr)	Formula	Description
1	18.2520	GtonneC/yr	2011.18	29.3045	u	Industrial CO_2
1	2.59791	GtonneC/yr	2003.38	162.813	u'	Land use CO_2
1	0.242866	GtonneC/yr	1910.94	19.6493	$e^{-x^2/2}/\sqrt{2\pi}$	Land use CO_2
1	0.199913	GtonneC/yr	1932.79	5.56387	$e^{-x^2/2}/\sqrt{2\pi}$	Land use CO_2
1	0.770972	GtonneC/yr	1959.73	9.13108	$e^{-x^2/2}/\sqrt{2\pi}$	Land use CO_2
1	0.965531	GtonneC/yr	1993.15	15.2196	$e^{-x^2/2}/\sqrt{2\pi}$	Land use CO_2
2	176.655	ppb/yr	1973.91	41.3836	u	CH_4
3	2.39098	ppb/yr	2003.32	40.3178	u	N_2O

Here, in the above Table P.1, u is $1/(1+e^{-x})$, a unit logistic function, u' is the first order time derivative of u.

In the table P.4, the first column gives the type of f_{nm} defined in equation 7.16 that each kind of gases are referring to. However, different g_n can be decomposed into g_{nm}, and the number of terms of g_{nm} contained in g_n varies with g_n. Thus, for the same type of g_n, some of them have more than one term of g_{nm}.

The first six parameters in Table P.2 define the dashed curve in figure 7.1. The next five parameters in Table P.2 are consistent with a base period thermal equilibrium. The next two parameters in Table P.2 are derived from the reference case surface ocean thermal inertia parameter and the equilibrium climate sensitivity. The last parameter in Table P.2 relates atmospheric carbon content in Gtonne to the atmospheric carbon dioxide concentration in ppm by volume.

Table P.2. Other Parameters

Value	Units	Description
0.84998	°K/(W/m^2)	reference case climate sensitivity, λ
48.7984	(W/m^2)yr/°K	reference surface ocean layer thermal inertia, c_3
1.5899	°K/(W/m^2	coal dominated aerosol shielding multiplier
50.4	yr	intrinsic temperature variation dominant period
0.0716995	°C	dominant intrinsic temperature variation amplitude
1891.5	Julian year	dominant intrinsic variation maximum time
286.681	°K	1650-1749 base period average temperature, T_0
0.299557	1	base period albedo
0.620523	1	base period emissivity
339.873	W/m^2	base period global average insolation
383.647	W/m^2	σT_0^4 with σ= Boltzman constant
761.519	m	mixed ocean layer volume/area ratio
41.4776	yr	ocean thermal inertia relaxation time, λc_3
2.13	GtonneC/ppm	<CO_2> per Gtonne of atmospheric carbon

Since it is more convenient to write out the solution of equation 7.15 than integrating it every time, the solution for each type of radiative forcing is provided below. There are overall ten different types of integrand in this work. Some of the integrands overlap, and so are not shown repeatedly. The first kind of solution I_1 is shown below.

$$I_1 = ((-1 + hyp2f1(1, s, 1+s, -e^x)) - e^{s\cdot(-x+x_0)} \cdot (-1 + hyp2f1(1, s, 1+s, -e^{x_0})) + s \cdot log(1+e^x) - s \cdot log(1+e^{x_0}))/s^2 \quad \text{(P.1)}$$

where,

$$x = (t - t_{nm})/w_{nm}$$

The $hyp2f1$ represents Gauss hypergeometric function 2F1, and x_0 is the value of x when $t = t_0 = 1750$, and s is the same variable defined as equation 7.14.
The second kind of solution I_2, which is the integration of unit logistic function u, is shown below.

$$I_2 = ((-1 + hyp2f1(1, s, 1+s, -e^x)) - e^{s\cdot(-x+x_0)} \cdot (-1 + hyp2f1(1, s, 1+s, -e^{x_0})) + s \cdot log(1+e^x) - s \cdot log(1+e^{x_0}))/s^2 \quad \text{(P.2)}$$

The third kind of solution I_3, which is the integration of error function, is shown below.

$$I_3 = e^{-sx} \cdot \sqrt{\pi/2} \cdot (e^{sx} \cdot erf(x/\sqrt{2})) - e^{s^2/2} \cdot erf((-s+x)/\sqrt{2})) - e^{sx} \cdot erf(x_0/\sqrt{2}) + e^{s^2/2}) \cdot erf((-s+x_0)/\sqrt{2})/s \quad \text{(P.3)}$$

The fourth kind of solution I_4, which is the integration of the first order time derivative of the logistic function, is shown below.

$$I_4 = (-(e^{x+x_0} + s + e^{2x_0} \cdot s + e^{x_0} \cdot (1+2s) - (1+e^x)) \cdot (1+e^{x_0})^2 \cdot s \cdot hyp2f1(1, s, 1+s, -e^x)/(1+e^x) + e^{(s\cdot(-x+x_0))} \cdot (s + e^{x_0} \cdot (1+s) - (1+e^{x_0})^2 \cdot s \cdot hyp2f1(1, s, 1+s, -e^{x_0})/((1+e^{x_0})^2 \cdot s) \quad \text{(P.4)}$$

The fifth kind of solution, which is the integration of second order time derivative of logistic function, is shown below.

$$I_5 = I_{51} + I_{52} + I_{53} + I_{54} + I_{55} \quad \text{(P.5)}$$

$$I_{51} = e^{-sx} \cdot (2 \cdot e^{(3+s)\cdot x_0}/((1+e^{x_0})^3 \cdot s) - 2 \cdot e^{sx+3x_0}/((1+e^{x_0})^3 \cdot s) - (3 \cdot e^{(2+s)\cdot x_0})/((1+e^{x_0})^2 \cdot s) + (3 \cdot e^{s\cdot x+2\cdot x_0})/((1+e^{x_0})^2 \cdot s) + e^{(1+s)\cdot x_0}/(s+e^{x_0}\cdot s) - e^{sx+x_0}/(s+e^{x_0}\cdot s) \quad \text{(P.6)}$$

$$I_{52} = e^{(1+s)\cdot x} \cdot hyp2f1(1, 1+s, 2+s, -e^x)/(1+s) - e^{(1+s)\cdot x_0} \cdot hyp2f1(1, 1+s, 2+s, -e^{x_0})/(1+s) \quad \text{(P.7)}$$

$$I_{53} = -3 \cdot e^{(2+s)\cdot x} \cdot (2+s-(1+e^x)\cdot(1+s)\cdot hyp2f1(1, 2+s, 3+s, -e^x)) /((1+e^x)\cdot(2+s)) \quad \text{(P.8)}$$

$$I_{54} = 3 \cdot e^{(2+s)\cdot x_0} \cdot (2+s-(1+e^{x_0})\cdot(1+s)\cdot hyp2f1(1, 2+s, 3+s, -e^{x_0})) /((1+e^{x_0})\cdot(2+s)) + e^{(3+s)\cdot x} \cdot (-(s+e^x\cdot(1+s))/(1+e^x)^2) \quad \text{(P.9)}$$

$$I_{55} = ((2+3s+s^2)\cdot hyp2f1(1, 3+s, 4+s, -e^x)/(3+s)) + e^{(3+s)\cdot x_0} \cdot ((s+e^{x_0}\cdot(1+s))/(1+e^{x_0})^2 - ((2+3s+s^2)\cdot hyp2f1(1, 3+s, 4+s, -e^{x_0})/(3+s))) \quad \text{(P.10)}$$

The sixth kind of solution, which is the integration of dilogarithm function $Li_2(z)$, is shown below.

$$I_6 = (-1 + hyp2f1(1, s, 1+s, -e^x) + s\cdot log(1+e^x) - e^{s\cdot(-x+x_0)} \cdot (-1 + hyp2f1(1, s, 1+s, -e^{x_0}) + s\cdot log(1+e^{x_0})) + s^2\cdot Li_2(-e^x) - s^2\cdot Li_2(-e^{x_0}))/s^3 \quad \text{(P.11)}$$

The seventh kind of solution, which is the integration of trilogarithm function $Li_3(z)$, is shown below.

$$I_7 = (-1/s^4) \cdot (-1 + hyp2f1(1, s, 1+s, -e^x) + s \cdot log(1+e^x) \\ + s^2 \cdot Li_2(-e^x) - e^{s\cdot(-x+x_0)} \cdot (-1 + hyp2f1(1, s, 1+s, -e^{x_0}) + s \cdot log(1+e^{x_0}) \\ + s^2 \cdot Li_2(-e^{x_0})) - s^3 \cdot Li_3(-e^x) + s^3 \cdot Li_3(-e^{x_0})) \quad \text{(P.12)}$$

The eighth kind of solution, which is the integration of gaussian function, is shown below. Here, erf is the error function.

$$I_8 = e^{s/2\cdot(s-2x)} \cdot \sqrt{\pi/2} \cdot (erf((-s + x)/\sqrt{2}) - erf((-s + x_0)/\sqrt{2})) \quad \text{(P.13)}$$

The ninth kind of solution, which is the integration of cosine function, is shown below.

$$I_9 = e^{-sx}(e^{sx} \cdot s \cdot cos(2\pi x) - e^{sx_0} \cdot s \cdot cos(2\pi x_0) + 2e^{sx} \cdot \pi \cdot sin(2\pi x) \\ - 2e^{sx_0} \cdot \pi \cdot sin(2\pi x_0))/(4\pi^2 + s^2) \quad \text{(P.14)}$$

The tenth kind of solution, which is the integration of a constant, is shown below.

$$I_{10} = -(-1 + e^{s(-x+x_0)})/s \quad \text{(P.15)}$$

The f_{nm} in equation 7.16 is shown in the table P.4. In P.4, u is the unit logistic function of the form $u = 1/(1+e^{-x})$, where $x = (t - t_{nm})/w_{nm}$ with t in Julian years. For different f_{nm}, x_0 is different, and x_0 is x evaluated at $t = t_0 = 1750$. Similarly, u_0 is u evaluated at $x = x_0$. Li_2, Li_3 are the dilogarithm and trilogarithm functions respectively. Erf denotes the error function.

The parameters used to compensate the intrinsic variations in that cosine function Q are listed in Table P.3.

$$Q = b_1 cos(b_3\pi(b_2 + t)) \quad \text{(P.16)}$$

Table P.3. Temperature Extrapolations Cosine Correction Function Parameters

Name	Values
b1	0.072332
b2	3783/2
b3	5/126

Table P.4. Atmopsheric Concentrations and Radiativie Forcing

f_{nm}	Formula	t_{nm}(yr)	w_{nm}(yr)	Description
f_{01}	$u(x)[1-u(x)]$	2003.34	162.813	Tropospheric O_3
f_{02}	$e^{-\frac{1}{2}x^2}$	2008.2	36.5573	Tropospheric O_3
f_{11}	$\int_{x_0}^{x} u dx$	2011.18	29.3045	<CO_2>
f_{12}	$u(x)-u(x_0)$	2003.34	162.813	<CO_2>
f_{13}	$\sqrt{\pi/2}[Erf(x/\sqrt{2})-Erf(x_0/\sqrt{2})]$	1910.94	19.6327	<CO_2>
f_{14}	$\sqrt{\pi/2}[Erf(x/\sqrt{2})-Erf(x_0/\sqrt{2})]$	1932.79	5.56387	<CO_2>
f_{15}	$\sqrt{\pi/2}[Erf(x/\sqrt{2})-Erf(x_0/\sqrt{2})]$	1959.73	9.13108	<CO_2>
f_{16}	$\sqrt{\pi/2}[Erf(x/\sqrt{2})-Erf(x_0/\sqrt{2})]$	1993.15	15.2196	<CO_2>
f_{21}	$u(1-u)-u_0(1-u_0)$	1973.91	41.3836	<CH_4>
f_{22}	$u(1-u)(1-2u)-u_0(1-u_0)(1-2u_0)$	1973.91	41.3836	<CH_4>
f_{23}	$u(x)-u(x_0)$	1973.91	41.3836	<CH_4>
f_{31}	$Li_2(-e^x)-Li_2(-e^{x_0})$	2003.34	40.3178	<N_2O>
f_{32}	$Li_3(-e^x)-Li_3(-e^{x_0})$	2003.34	40.3178	<N_2O>
f_{33}	$1-u(x)$	1956.34	5.08431	<N_2O>
f_{34}	$\int_{x_0}^{x} u dx$	2003.34	40.3178	<N_2O>
f_{41}	$u(x)$	1980.04	7.5219	<Other>
f_{51}	$u(x)$	2026.34	17.8118	Contrails
f_{61}	$u(x)[1-u(x)]$	1893.04	42.944	Land use
f_{62}	$u(x)$	1952.34	20.064	Land use
f_{71}	$e^{-\frac{1}{2}x^2}$	2001.19	28.4973	Aerosols etc.
f_{72}	$u(x)(1-u(x))$	2003.34	162.813	Aerosols etc.
f_{81}	$1-u(x)$	1795.5	2	Volcanoes
f_{82}	$u(x)$	1795.5	2	Volcanoes
f_{83}	$u(x)$	1819	2	Volcanoes
f_{84}	$u(x)$	1819	2	Volcanoes
f_{91}	$cos(2\pi x)$	1566.39	257.658	Solar Irradiance
f_{92}	$cos(2\pi x)$	841.916	1365.57	Solar Irradiance
f_{93}	$e^{-\frac{1}{2}x^2}$	1854.18	11	Solar Irradiance
f_{94}	$e^{-\frac{1}{2}x^2}$	2013.95	5.5	Solar Irradiance
f_{95}	1	1566.39	257.658	Solar Irradiance